TECHNISCHE UNIVERSITÄT MÜNCHEN
FAKULTÄT FÜR ELEKTROTECHNIK UND INFORMATIONSTECHNIK

Electrical Characterization of the Displacement Damage in III-V Space Solar Cells

Carmine Pellegrino

Vollständiger Abdruck der von der Fakultät für Elektrotechnik und Informationstechnik der Technischen Universität München zur Erlangung des akademischen Grades eines

Doktors der Naturwissenschaften

genehmigten Dissertation.

Vorsitzender: Prof. Dr.-Ing. Christian Jirauschek

Prüfer*innen der Dissertation:

1. Prof. Dr. Alessio Gagliardi
2. Assoc. Prof. Federica Cappelluti

Die Dissertation wurde am 12.07.2021 bei der Technischen Universität München eingereicht und durch die Fakultät für Elektrotechnik und Informationstechnik am 11.04.2022 angenommen.

TECHNISCHE UNIVERSITÄT MÜNCHEN

FAKULTÄT FÜR ELEKTROTECHNIK UND INFORMATIONSTECHNIK

CHAIR OF NANOELECTRONICS

Electrical Characterization of the Displacement Damage in III-V Space Solar Cells

Author: Carmine Pellegrino
Supervisor: Prof. Dr. Alessio Gagliardi
Mentors: Dr. Claus Zimmermann
Dr. David Lackner

Alla mia famiglia.

Abstract

For more than two decades, the non-ionizing energy loss (NIEL) has been used by the solar cell radiation community to model the performance degradation of solar cells due to the displacement damage caused by particle radiation environment in space. A NIEL with an atomic displacement threshold energy $E_{\mathrm{d}} = 21\,\mathrm{eV}$ is customarily used in the Naval Research Laboratory (NRL) method for the degradation analysis of GaAs-based solar cell photovoltaic parameters. This E_{d} value is higher than the one expected from atomistic simulations in GaAs. Moreover, the same amount of physical damage calculated with $E_{\mathrm{d}} = 21\,\mathrm{eV}$ has different electrical effects on the solar cell, depending whether it is incurred by electrons or protons. The discrepancies are accounted for with phenomenological factors in the NRL method, yet a physical explanation is still missing.

In this dissertation, the displacement damage-induced degradation of state-of-the-art GaInP/(In)GaAs/Ge triple-junction space solar cells is characterized comprehensively with a multi-level approach, and physical explanations for the discrepancies between electron and proton damage are addressed.

Solar cells and related component cells were irradiated with electrons and protons in the MeV range and exposed to photon and thermal annealing procedures according to relevant space standards. The changes in the macroscopic photovoltaic parameters, namely the open-circuit voltage V_{OC} and the short-circuit current density J_{SC}, were monitored by means of illuminated current density-voltage (J-V) characteristics. The electrical characterization of electron- and proton-induced defects in the (In)GaAs sub-cell, as well as their influence on the macroscopic parameters, was achieved by means of dark J-V analysis and admittance spectroscopy. First, the dark J-V characteristics are fitted with the help of an analytical model based on Shockley-Read-Hall statistics. A remarkable difference in the space-charge region lifetimes associated to mid-gap recombination centers is found, which is the first sign of a different type of damage introduced by the two particles. The discrepancy is further investigated at a defect level by means of admittance spectroscopy analysis on (In)GaAs component cells and a complementary deep-level transient spectroscopy (DLTS) study on GaAs mesa-diodes.

Defect spectroscopy combined with NIEL analysis is shown to be a powerful tool for analyzing solar cell radiation degradation from a fundamental point of view, not relying on the change of macroscopic cell parameters. The threshold energies for defect formation are assessed by analyzing the dependence of the defect introduction rates on the NIEL deposited by electrons in the semiconductor. The atomic recoil spectrum due to collisions with protons and electrons of different energies are found to influence the relative abundance of the different defects. An electron NIEL with

$E_d = 21\,\mathrm{eV}$ is found to be proportional to the relative abundance of the irradiation-induced defects. Thus, the 21 eV value is not only a parameter obtained from the fitting of the macroscopic degradation data, but rather a GaAs material-specific parameter independent of the device electrical design.
For a similar amount of NIEL dose introduced in the solar cell, protons are almost three times more effective than electrons in damaging V_{OC}. In the NRL method, this effect is accounted for with an empirical factor R_{ep} converting the electron dose to an equivalent proton dose. In this thesis, the origin of the R_{ep} factor is traced back to different properties of the recombination centers in (In)GaAs sub-cell, ultimately attributed to different type of defects produced by the two particles. The electron displacements are mostly generated by low-energy recoils in the range of few tens of eV, whereas a significant fraction of proton displacements are caused by long collision cascades due to high-energy recoils in the order of hundreds of eV up to keV. The damage produced in the two cases is considerably different, regardless of the total number of displacement produced: isolated point defects are expected in the electron case, whereas clustered damage in the proton case. This difference is observed and characterized by DLTS and admittance spectroscopy. The enhanced carrier capture cross-section observed at proton-induced recombination centers is found to be the ultimate cause of the enhanced V_{OC} degradation.

Zusammenfassung

Seit mehr als zwei Jahrzehnten wird der Non-Ionizing Energy Loss (NIEL) von der Solarzellengemeinschaft verwendet, um die Leistungsverschlechterung von Solarzellen aufgrund der durch die Teilchenstrahlungsumgebung im Weltraum verursachten Verdrängungsschäden zu modellieren.
In weltraumtauglichen GaInP/(In)GaAs/Ge Triple-Junction (3J)-Solarzellen wurden Abweichungen der elektronen- und protoneninduzierten Degradation von den theoretischen Modellen beobachtet. Die Diskrepanzen werden mit phänomenologischen Faktoren für die End-of-Life (EOL)-Vorhersagen von Solarzellen erklärt, obwohl das Problem bisher noch nicht vom grundlegenden physikalischen Aspekt her untersucht wurde.
In dieser Dissertation wird die durch Verschiebungsschäden induzierte Degradation von 3J-Solarzellen mit einem mehrstufigen Ansatz umfassend charakterisiert. Weltraumtaugliche Solarzellen und zugehörige Komponentenzellen sowie Ad-hoc-Mesastrukturen wurden mit Elektronen und Protonen im MeV-Bereich bestrahlt und Photonen- und thermischen Ausglühverfahren nach relevanten Weltraumstandards ausgesetzt. Die änderungen der makroskopischen photo-voltaischen Parameter, nämlich die Leerlauf Spannung V_{OC} und der Kurzschlussstromdichte J_{SC}, wurden mittels beleuchteter Strom-Spannungs-Kennlinien (I-V) verfolgt. Eine ziemlich umfassende elektrische Charakterisierung der protonen- und elektroneninduzierten Defekte in der (In)GaAs-Subzelle und deren Einfluss auf die makroskopischen Parameter wurde mittels Dunkel-I-V-Analyse, Admittanzspektroskopie (AS) und Deep-Level-Transient-Spektroskopie (DLTS) erreicht.
Zunächst wird eine eigentümliche Signatur des bestrahlenden Teilchens im lokalen Idealitätsfaktor der dunklen I-V-Kennlinie gefunden. Mit Hilfe eines analytischen Modells, das auf der Shockley-Read-Hall-Statistik basiert, wird der Rekombinationsstrom in der Raumladungsregion (SCR) berechnet und der lokale Diodenidealitätsfaktor genau reproduziert. Ein bemerkenswerter Unterschied in den SCR-Lebensdauern, der mit strahlungsinduzierten Rekombinationszentren assoziiert ist, wird als Hauptursache für die Proton-Elektron-Divergenz gefunden. Die Diskrepanz wird mittels AS-Analyse an (In)GaAs-Komponentenzellen auf Defektniveau weiter untersucht. Die AS-Ergebnisse werden durch eine ergänzende DLTS-Studie an GaAs-Mesa-Dioden unterstützt.
Die Defektspektroskopie in Kombination mit der NIEL-Analyse erweist sich als ein leistungsfähiges Werkzeug zur Analyse der Strahlungsdegradation von Solarzellen Strahlungsdegradation von einem fundamentalen Standpunkt aus zu analysieren, der nicht auf der Veränderung makroskopischer Zellparameter beruht. Die Natur eines jeden Defekts wird durch die Analyse der Abhängigkeit seiner Einführungsrate

von der NIEL, die von den Elektronen im Halbleiter deponiert wird. Es wird festgestellt, dass die Rückstoss-spektren verschiedener Teilchentypen und Energien die relative Häufigkeit der verschiedenen Defekte beeinflussen. Eine Elektronen-NIEL mit einer atomaren Schwellenenergie E_d, die üblicherweise für die Degradationsanalyse von GaAs-basierten Solarzellen verwendet wird Analyse verwendet wird, stellt eine Annäherung an die relative Defekthäufigkeit dar. Der 21 eV-Wert ist somit ein GaAs-materialspezifischer Parameter, unabhängig vom elektrischen Gerätedesign.
Der grundsätzliche Unterschied zwischen dem Einfluss der Elektronen- und der Protonendosis wird in Form von unterschiedlichen Eigenschaften der mittleren Lückenzustände verstanden. Ein breites Merkmal der Defektspektren wird im Protonenfall beobachtet, und es wird auf geclusterte Defekte zurückgeführt. Diese Art der Schädigung unterscheidet sich deutlich von den isolierten Punktdefekten, die im Elektronenfall beobachtet werden, und ist unabhängig von der Gesamtverschiebungsschaden, der sich im Material ablagert. Die durch Protonen ausgelösten hochenergetischen Rückstösse sind verantwortlich für die Bildung dieser ungeordneten Regionen verantwortlich. Der erhöhte Ladungsträgereinfangquerschnitt, der an diesen Rekombinationszentren beobachtet wird, ist die eigentliche Ursache für die erhöhte V_OC Degradation und erklärt somit der Proton-Elektron-Äquivalenzfaktoren R_ep, die in der Methode des US Naval Research Laboratory (NRL) angenommen wurden.

List of Own Publications and Contributions

This dissertation is based on the work conducted at the Solar Array Engineering and Design department, Airbus Defence and Space GmbH, and partially also at the III-V Epitaxy and Solar Cell department, Fraunhofer Institute for Solar Energy, from 2018 until 2021. Part of this work is based on the following scientific contributions:

Peer-reviewed journal contributions

C. Pellegrino, A. Gagliardi, and C. G. Zimmermann, "Defect spectroscopy and non-ionizing energy loss analysis of proton and electron irradiated p-type GaAs solar cells" , Journal of Applied Physics 128, 195701 (2020)

C. Pellegrino, A. Gagliardi and C. G. Zimmermann, "Difference in space-charge recombination of proton and electron irradiated GaAs solar cells. Prog Photovolt Res Appl. 2019; 27: 379 - 390.

C. Pellegrino, A. Gagliardi and C. G. Zimmermann, "Impact of Proton and Electron Irradiation-Induced Defects on the Dark Current of GaAs Solar Cells," in IEEE Journal of Photovoltaics, vol. 9, no. 6, pp. 1661-1667, Nov. 2019, doi: 10.1109/JPHOTOV.2019.2941733.

Conference proceedings

C. Pellegrino, A. Gagliardi and C. G. Zimmermann, "Admittance Spectroscopy on Irradiated GaAs Component Cells: Defect Analysis and Characterization," 2020 47th IEEE Photovoltaic Specialists Conference (PVSC), Calgary, AB, Canada, 2020, pp. 0156-0159, doi: 10.1109/PVSC45281.2020.9300890.

C. G. Zimmermann, M. Rutzinger, C. Pellegrino, M. Salzberger and H. Nesswetter, "Determination of subcell properties in multijunction solar cells through pulsed illumination," 2018 IEEE 7th World Conference on Photovoltaic Energy Conversion (WCPEC), 2018, pp. 1564-1569, doi: 10.1109/PVSC.2018.8547433.

Conference presentation

C. Pellegrino, A. Gagliardi and C. G. Zimmermann, "Characterization of the Defects Introduced by Proton and Electron Irradiation in GaAs Solar Cells via Dark I-V Analysis", Oral Presentation at 46th IEEE Photovoltaic Specialist Conference, June 2018

Contents

1 Introduction **1**
1.1 Space photovoltaics . . . 4
1.2 The III-V materials . . . 6
1.3 Scope and outline of this thesis . . . 7

2 Radiation Damage in III-V Solar Cells: Fundamentals and Modeling **9**
2.1 Space radiation environment . . . 9
2.1.1 Radiation belts . . . 10
2.1.2 Radiation environment modeling . . . 12
2.2 Non-ionizing collisions in semiconductor crystals . . . 14
2.2.1 Defect production . . . 14
2.2.2 Defect reordering . . . 16
2.2.3 Characterization of the recoil damage . . . 17
2.2.4 Non-Ionizing Energy Loss (NIEL) . . . 18
2.3 NIEL scaling . . . 25
2.3.1 Displacement Damage Dose (DDD) method . . . 25
2.3.2 Limits of applicability . . . 26
2.3.3 Physical interpretation . . . 27
2.4 Radiation damage coefficients . . . 28
2.4.1 Dark current . . . 30
2.4.2 Short-circuit current density . . . 32
2.4.3 Open-circuit voltage . . . 34

3 Experimental Setups **37**
3.1 Solar Cell structure . . . 37
3.1.1 Triple-junction solar cell . . . 37
3.1.2 Component cells . . . 39
3.1.3 Mesa-diodes . . . 40
3.2 Experimental techniques . . . 40
3.2.1 Irradiation experiments . . . 40
3.2.2 Characterization methods . . . 42
3.2.3 Defect spectroscopy methods . . . 44

4 Photovoltaic Parameter Degradation **53**
4.1 Fitting of the remaining factors . . . 54
4.2 $In_{0.01}Ga_{0.99}As$ middle component cell . . . 54

4.3 $Ga_{0.5}In_{0.5}P$ top component cell 57
4.4 3J solar cell 60
4.5 Quality of component cell-based degradation analysis 62

5 Dark Current Degradation **63**
5.1 Two-diode model approach 63
5.2 Recombination current in the space-charge region 66
5.2.1 Shockley-Read-Hall discrete model 67
5.2.2 Fitting of the inverse ideality factor 70
5.2.3 Fitting results 74
5.2.4 Conclusion on the electron- and proton-induced recombination current 76

6 Admittance spectroscopy on $In_{0.01}Ga_{0.99}As$ middle component cell **77**
6.1 Introduction 77
6.2 Experimental details 78
6.3 Admittance evaluation 79
6.3.1 General considerations 79
6.3.2 Parameter fitting 80
6.4 NIEL Defect Analysis 83
6.4.1 Recoil contribution 83
6.4.2 Fitting of the Defect E_d 84
6.5 Irradiation-induced defects 85
6.6 Discussion 87
6.6.1 Effective defect NIEL* 87
6.6.2 Relative defect introduction 88
6.6.3 Macroscopic parameter degradation 88
6.6.4 Proton-electron equivalence factors 90
6.7 Conclusion 91

7 Deep-level Transient Spectroscopy on GaAs Mesa-diodes **93**
7.1 Introduction 93
7.2 Experimental details 94
7.3 Data analysis 95
7.4 Electron irradiation 96
7.4.1 Electron traps in n-GaAs 96
7.4.2 Hole traps in p-GaAs 97
7.4.3 Annealing dynamics 98
7.4.4 Correlation with the trap levels in $In_{0.01}Ga_{0.99}As$ 101
7.4.5 Effective defect NIEL* 105
7.5 Proton irradiation 106
7.5.1 Difference between proton and electron damage 107
7.6 Conclusion 108

8 Summary, Conclusion and Outlook **111**

Bibliography **117**

Chapter 1

Introduction

The importance of efficient systems able to harvest energy from renewable sources is paramount in the present days, where the unequivocal global warming awareness imposes tight constraints on the utilization of fossil fuels. Pioneered in the early years of the XX century, the semiconductor photovoltaic (PV) technology has developed rapidly in the last decades and, nowadays, it plays a major role in the world renewable energy harvesting systems.

The PV effect is an electromagnetic radiation-matter interaction that excites electrons in a material by means of photon absorption. The energy transition experienced by the electrons equals the energy of the absorbed photon E_{ph}. A solar cell device is a conveniently-designed semiconductor device aimed to collect and extract those photo-generated carriers. Particularly suitable device for this task is a simple p-n junction. The electron-hole pair generated in the semiconductor is separated with the help of the junction electric field, and collected at the terminal of the device as output electric power. The PV research community is constantly seeking to obtain solar cells with higher conversion efficiency, thanks to technological improvement and the choice of the right materials.

The efficiency chart published yearly by the US National Renewable Energy Laboratory (NREL) keeps track of the conversion efficiency record reached in PV laboratories by different solar cell technologies. The chart is shown in Fig. 1.1. The different trends highlight the relevant material opportunities and research effort by the scientific community.

Nowadays, silicon represents the most established PV technology and dominates the terrestrial PV market. The development of silicon-based PV technology took advantage of the heritage of the semiconductor industry development in the last decades of the XX century. The reasons can be found in the accessible raw material procurement as well as in the technological establishment. Silicon is relatively inexpensive material to collect, due to the large abundance on Earth and well-established extraction and pure ingot production techniques. The possibility to easily grow insulating oxide during device fabrication processes made it extremely attractive for the electronic industries.

Despite these advantageous features, silicon is not the ideal material for a solar cell device. The quality of a semiconductor material aimed to PV applications can be described in terms of its theoretical conversion efficiency, i.e., the maximum conversion

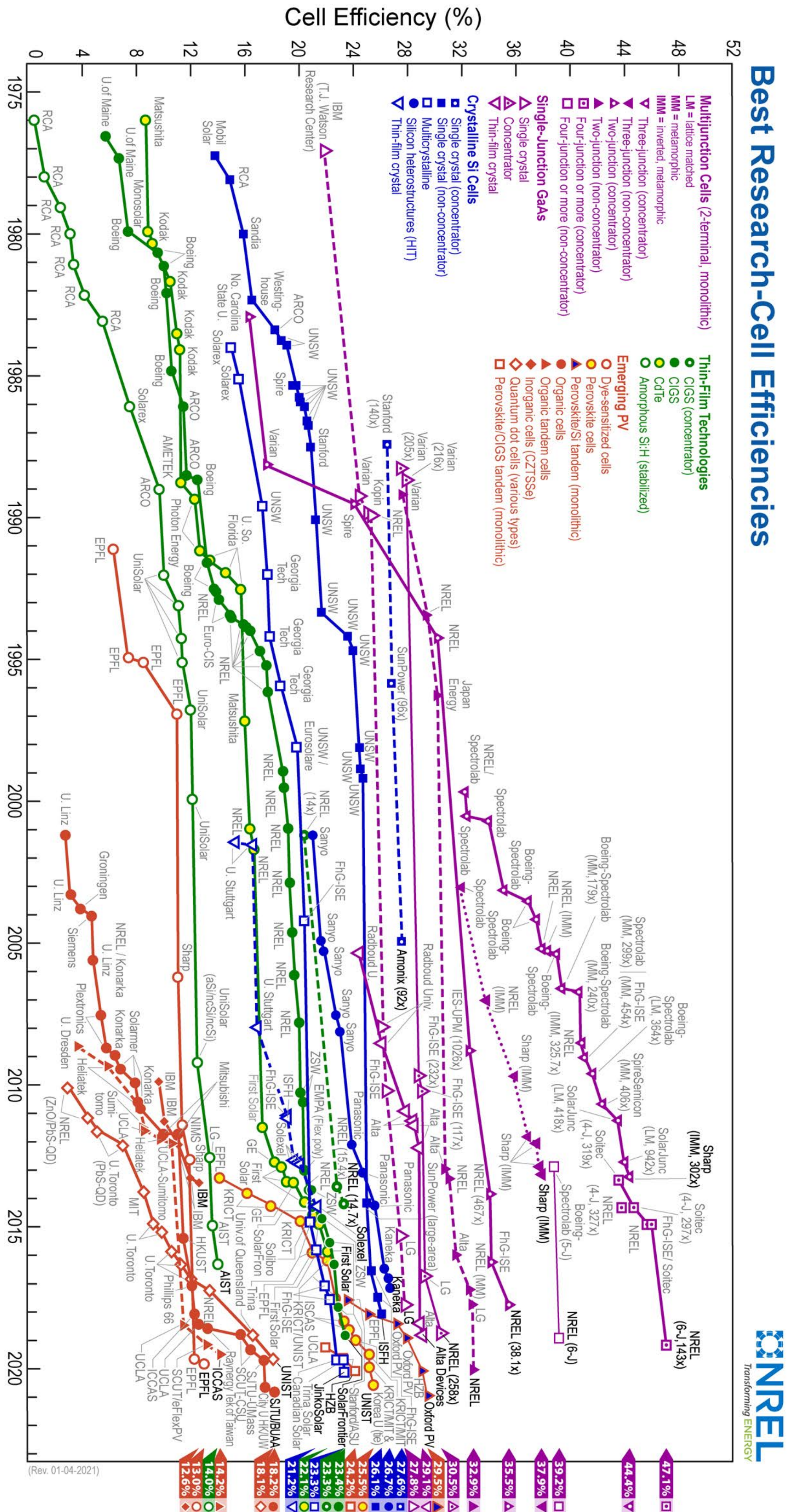

Figure 1.1 – Best research solar cell efficiency table 2020. *Credit: NREL*

efficiency achievable under idealistic assumptions, and the real achievable conversion efficiency, which is usually limited by technological processes. The theoretical conversion efficiency achievable for a solar cell is today known as the Shockley-Queisser (SQ) limit [1]. The SQ model makes use of a detailed balance between the collectable charge carriers in a p-n device exposed to a photon source. Each semiconductor technology is characterized by its absorption capability of the solar photon spectrum. The model aims to provide the intrinsic limitation of a given solar cell technology, in the ideal assumption that the only carrier loss mechanisms within the device are due to radiative recombination. A photon with a certain wavelength λ transfers an energy E_{ph} to the excited electron given by:

$$E_{\mathrm{ph}} = \frac{hc}{\lambda}, \tag{1.1}$$

where h is the Planck's constant and c is the speed of light in vacuum. Denoted as E_{BG} the semiconductor band gap, the photon usage can be framed as follows:

- photons with $E_{\mathrm{ph}} > E_{\mathrm{BG}}$ are absorbed in the material and electron-hole pairs are photo-generated. The energy difference E_{ph} - E_{BG} is, however, lost due to the fact that the excited carriers thermalize to the band edge usually in the time scale below ps;
- photons with $E_{\mathrm{ph}} = E_{\mathrm{BG}}$ are efficiently converted by the ideal device;
- photons with $E_{\mathrm{ph}} < E_{\mathrm{BG}}$ cannot be absorbed in the material due to the absence of available energy states for electrons. The energy of these photons is then completely lost.

If the band gap is tuned according to the photon spectrum of the light source, the photon usage and thus the conversion efficiency is improved. In the single-junction device case, $E_{\mathrm{BG}} = 1.34\,\mathrm{eV}$ allows the best usage of the solar photon spectrum, yielding a maximum theoretical efficiency of 33.7%. A silicon single-junction solar cell has a less favorable band gap of 1.1 eV, which results in a maximum theoretical efficiency of about 32%. This limit is, however, purely theoretical. Several carrier loss mechanisms limit the collection efficiency of silicon cells. The understanding of the SQ detailed balance principle is essential to find alternative solution to silicon, aiming to improve the PV conversion efficiency. The assumptions laid down in the original paper [1], viewed from a different angle, represent new opportunities for devices to overcome these barriers. Among the main assumptions in the SQ model, the choice of a single band gap device limits significantly the usage of the photon spectrum, and can be overcome with the multi-junction approach. Two or more p-n junctions are connected in series, each of them absorbing a different portion of the incoming photons, and producing a similar amount of photo-generated current. In such a device, the thermalization losses are reduced, the photon utilization improves and so does the conversion efficiency. To enable this technologies, high-quality materials with good band gap tunability are required. In this context, semiconductor alloys involving III-V elements are extremely attractive materials, thanks to the great flexibility of band gap and lattice constant tuning, without compromising the

material quality. Nowadays, the world record of best research cell efficiency is held by NREL with a III-V-based 6-junction solar cell reaching 39.2% efficiency under the AM1.5 spectrum [2].

1.1 Space photovoltaics

In the early phases of a space mission design, the best combination of energy source, conversion and storage technologies has to be selected. Among the available options that are compatible with a given space mission and its environment, the final optimum selection must meet multiple criteria but primarily low mass and cost. In Fig 1.2, a classification of the different available approaches for different satellite power ratings are shown, according to Ref. [3]. The dividing lines among various options are only approximate and have large overlaps. Solar cell technology has been pioneered to a large extent by space industry, as solar energy is the main power sources for satellite missions in the timescale of years. Among the different possible approaches for satellite on-board power generation, the solar generator is by far the most widely adopted due to technology expertise, modularity and relatively low-cost as compared to other solutions. A solar generator is a complex structure designed for a vast class of space missions, from telecommunication applications to Earth observation, from military applications to space science. Only few special missions are unable to be equipped with solar generators: for instance, deep space missions further than Jupiter orbit are subjected to such a low solar intensity that a solar panel area out of the affordable range of the satellite budget would result. Despite the huge list of problematics inherent to the different parts of a solar generator, this dissertation focuses only on the solar cell level. Solar generators are populated with electrically-interconnected solar cells, either attached to the core structure of the satellite (body-mounted configuration) or connected in an array configuration via yokes to the spacecraft platform. The latter solution offers the advantage of a panel orientation disjointed from the attitude of the spacecraft.
The first generation of space PV relied on silicon solar cell technology. As the

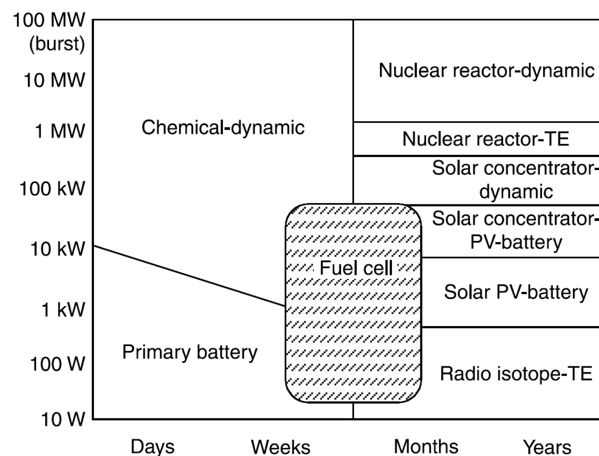

Figure 1.2 – Optimum energy sources for various power levels and space mission durations according to [3].

space business evolved since its dawning in the middle of the XX century, however, satellite market demanded higher on-board power generation capability and longer lifetime operations. III-V solar cells, with their higher conversion efficiency and more intrinsic endurance to space radiation, replaced silicon cells as leaders of the space PV market.
In designing a solar generator for a space mission, the space environment sets a number of challenges for solar cells not typically encountered in terrestrial application. Several environmental factors contribute in the degradation of the solar cell performance and thus impact on the lifetime of the overall mission. The most striking constraints of the space environment are:

- Pressure conditions: the high vacuum of the space causes out-gassing of volatile elements from the spacecraft materials which can deposit and contaminate the optical surface of the solar cell, thus reducing the conversion efficiency;
- Particle charging: The solar panels are exposed to space plasma particles which cause accumulation of charged particles on the surface; discharge bursts via solar cell components may cause failure of entire panel strings;
- Space debris: micro-meteoroids and spacecraft debris in orbit, ranging from few mm up to m, can impact the surface of the solar array leading to permanent damage and drastic power failure;
- Photon radiation: particularly sensitive is the ultraviolet (UV) and vacuum ultraviolet (VuV) radiation which in space is not shielded by the Earth atmosphere. It causes material surface contamination and degradation, and it induces colour centers in the optical components such as the cover glass. Moreover, it contributes significantly in the thermal balance by heating up the solar panels, thus lowering the conversion performance since only radiative cooling is possible in space;
- Thermal environment: spacecraft are usually subjected to rapid temperature changes in a wide range of hundreds of kelvins during eclipse phases. Mechanical stress due to expansion coefficient mismatch may lead to delamination or cracks on the cell or damage at the interconnection levels;
- Atomic oxygen: the dissociation of oxygen-related molecules (O_2, O_3) in atomic oxygen (ATOX) at low Earth orbit (LEO) is extremely harmful, since it collides with the panel surface;
- Charged particle environment: the non-ionizing energy deposited in the solar cell material by high-energy electrons, protons, heavier ions or high-energy photons introduces defects in the semiconductor crystal which lead to a degradation of the solar cell electrical performance.

The design of a space solar array has to deal with all the constraints imposed by similar conditions. At the material level, particularly important is the the endurance to the charged particle environment. Solar cells in the space environment experience electrical performance degradation over time due to the interaction with electrons

and protons in the MeV range. The main cause of degradation due to particle interactions is ascribed to displacement damage, namely the formation of stable defects in the semiconductor crystal lattice as a result of the non-ionizing collision between the impinging particle and the atoms of the target material. The ultimate effect is a solar cell power degradation which limits the maximum operative lifetime of a given solar array.
Space PV research seeks for high-quality solar cell materials and technologies guaranteeing the best power conversion efficiency and a superior endurance to space radiation. Conversion efficiency and radiation-hardness are thus the two key features that a space-grade solar cell shall prove to gain access in the space PV market. Advanced solar cell technologies improving both features will enable higher power ratings on-board the next-generation satellite, extending their operative lifetime.

1.2 The III-V materials

III-V solar cells are grown by using a 1:1 combination of atoms from the third and fifth group of the periodic table of elements. III-V solar cells have achieved the highest efficiencies of any solar cell technology, closest to their theoretical limits. The reasons are found in the very high opto-electronic performance of the materials combined with a well-established epitaxial growth technology. Gallium arsenide (GaAs) is an example of III-V material combination for solar cell reaching for the SQ limit. Most of the III-V compounds have direct band gap, which means higher absorption coefficients α and thus thinner layers required to create fully-absorbant cells. For instance, GaAs has a very high value of α near its 1.42 eV band gap edge ($\alpha = 8\times10^3\,\mathrm{cm}^{-1}$, about $\sim 10^4$ times higher than Si [4]), which leads to a theoretical maximum efficiency of 33.5% achieved with a cell $\sim$100 times thinner than the respective Si-based cell. Moreover, GaAs is one of the very few material systems that can reach internal fluorescence yields close to 1 [5], which is essential to approach the SQ limit.
In addition to the optimum opto-electronic quality, III-V technology allows a great tuning flexibility of several material properties such as band gap, lattice constant, refractive index and endurance to chemical processes. This offers a great advantage in the frame of multi-junction solar cells. Growth technologies such as metal organic chemical vapour deposition (MOCVD) and molecular beam epitaxy (MBE) allow epitaxial layers with very few crystal defects to be grown. This enhances the material quality significantly in terms of carrier lifetime. Moreover, the possibility to grow passivating hetero-interfaces with very low surface recombination velocities and the availability of highly transparent and conductive tunnel junctions make these materials the best candidate for multi-junction solar cells.
III-V solar cells are grown on high-quality substrates either from III-V, e.g.,GaAs or InP, or on IV group semiconductor substrates, e.g., Ge. Germanium is a suitable IV-group substrate for III-V epitaxy, thanks to its lattice constant almost matching with GaAs. In recent years, promising results have been reached in combining III-V epitaxy on silicon substrates [6]. When combining the optimum combination of materials with different lattice constants to form high-efficiency multi-junction solar cells, many challenges arise from the lattice mismatch and metamorphic solutions

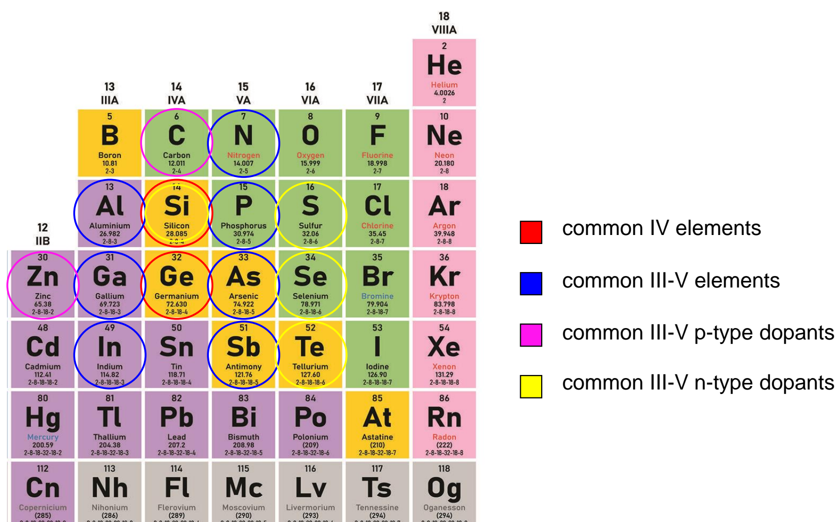

Figure 1.3 – Common III-V elements and dopant atoms adopted in MOCVD epitaxy for space multi-junction solar cells.

or wafer bonding techniques are required.
Despite the higher performance, III-V technology has the disadvantage to be expensive, mainly due to the precursor material costs and to the growth technology. New technologies to lower the growth cost of III-V cells is one of the main research subject nowadays in the PV community, for instance by employing substrate recycling strategies such as epitaxial lift-off [7], or moving toward higher growth rates [8]. Nonetheless, nowadays III-V cells remains mainly adopted in systems where their high efficiency outweighs their high cost, i.e., concentrated and space PV.

1.3 Scope and outline of this thesis

This dissertation addresses the electrical characterization of the displacement damage introduced with particle radiation in III-V solar cells. A multi-level approach is adopted: the damage is characterized from the macroscopic point of view, the degradation of the main PV outputs of the solar cell, down to the microscopic physical level, covering the defect production in the semiconductor materials. The microscopic route is followed by employing defect spectroscopy techniques such as admittance spectroscopy (AS) and deep-level transient spectroscopy (DLTS), as well as local dark current analysis, a method developed as part of this thesis. The microscopic and macroscopic analysis lead to a sound modeling of III-V solar cell degradation in space, which helps in predicting the operative lifetime of solar arrays. The degradation due to the complex, multi-energetic nature of the space radiation environment is dealt with the NIEL scaling approach. A careful analysis provides additional insights and physical explanations to the Naval Research Laboratory (NRL) method, customarily used by space radiation community in treating

solar cell degradation data. The analysis has been carried out on space-grade solar cells, representative of products currently available on the space PV market, as well as on ad-hoc structures aimed for defect spectroscopy purposes.
In Chapter 2 the basic concepts on the space environment, radiation damaging mechanism and modeling of basics solar cell parameters are outlined. The structure of the solar cell devices investigated, as well as the experimental setups, techniques and models adopted for the data analysis are described in detail in Chapter 3. The degradation analysis of the macroscopic photovoltaic solar cell parameters is presented in Chapter 4. The degradation analysis of the cell dark current is presented in Chapter 5. In Chapter 6 and 7 the results of the defect spectroscopy analysis are presented. Final conclusions on the work done and possible outlook are presented in Chapter 8.

Chapter 2

Radiation Damage in III-V Solar Cells: Fundamentals and Modeling

2.1 Space radiation environment

The space radiation environment relevant to solar cell performance degradation consists of electrons, protons and heavier ions ranging from few keV up to tens or hundreds of MeV. These particles have different nature: they can be originated from the solar activity, trapped in the Earth magnetic field surrounding the planet, or coming from interplanetary regions outside of the solar system. The sun is the major responsible for the generation of high-energy charged particles in Earth orbits. The inner core of the sun hosts nuclear fusion reactions where H atoms are transformed in He atoms. The high temperatures cause the positively charged ions and negatively charged electrons that make up the sun plasma to move continuously, thus creating complicated magnetic fields that twist and turn. The dynamic of the plasma and the magnetic field in the solar corona are responsible of the particle ejection from the sun to the outer space. Particle ejection events are classified as solar flares, coronal mass ejections (CME) and solar energetic particle events.
The plasma dynamic within the sun controls every solar particle event. According to the sun dynamo theory laid down by Parker *et al.* [9], the dynamic of the plasma inside the sun core allows the magnetic field to poke out of the corona surface, producing black sunspots on the star surface. The magnetic field, pierced out of the corona, can stretch and twist so that field lines with opposite direction are pressed together, leading to the fundamental process of the magnetic reconnection.
The reconnection of the magnetic field topology in highly conductive plasma environment produces thermal and kinetic energy which triggers particle acceleration. If the reconnection leads to acceleration of particles toward the outer space, an energetic particle event occurrs. As the magnetic field lines reconnect, particles can also be accelerated backward toward the sun surface. The particles stream down the magnetic field at relativistic velocities and slam onto the dense layers of the sun surface, releasing energy in form of other particles and electromagnetic radiation over the entire wavelength spectrum, from the radio up to gamma waves. The bright flash produced is known as solar flare. During a solar flare, tons of material from the sun corona can be ejected toward outer space. This phenomenon is referred to

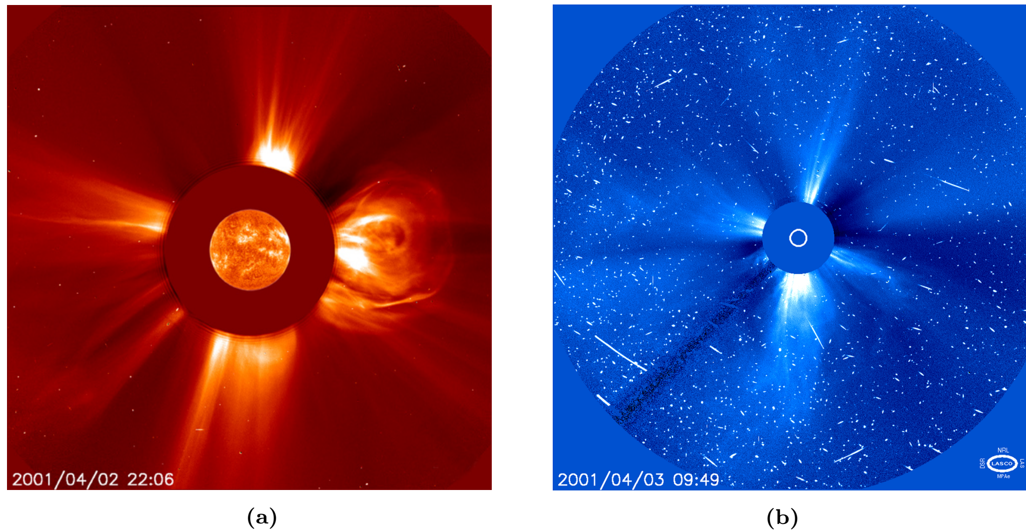

(a) (b)

Figure 2.1 – Solar flare and coronal mass ejection (CME) recorded by the SOHO satellite on the 2nd of April 2001. (a) Superposition of the ultraviolet imaging telescope (EIT) and spectrometric coronagraph data (LASCO), where the solar flare and the CME are visible, respectively. (b) Proton event associated with the solar flare resulting in bright pixels in the coronagraph imaging, recorded few hours after the solar flare. Courtesy of SOHO/MDI, SOHO/EIT, and SOHO/LASCO consortium. SOHO is a project of international cooperation between ESA and NASA.

as CME.
Solar flare and CME are monitored by the Solar and Heliospheric Observatory (SOHO) satellite, a result of the collaboration between ESA and NASA. An exemplary case of solar flare and CME recorded by the SOHO instruments is shown in Fig. 2.1 (a). The outer part of the images are the data from the spectrometric coronagraph LASCO, a telescope designed to block the light coming from the solar disk in order to capture the extremely faint electromagnetic emission from the outer corona layers. The inner picture, superimposed to the coronagraph image, shows the inner solar disk captured by the ultraviolet imaging telescope. The solar flare can be viewed in the inner image as a bright area on the surface of the sun. Simultaneously, a CME event is observable in the coronagraph image. The image in Fig. 2.1 (b), recorded few hours after the image in Fig. 2.1 (a), shows a solar particle event, appearing as bright spots caused by the detector pixel saturation. The particle event is ascribed as a direct consequence of the CME, as the heavier particles ejected from the solar corona travel slower than the electromagnetic radiation.

2.1.1 Radiation belts

The solar wind carries magnetic field through its journey in the outer space, according to the Alfven theorem [10]. When it interacts with planet magnetic fields, such as the one of the Earth, the interaction between energetic particles and the magnetic field lines leads to particle trajectory deflection. If the magnitude of the planet magnetic field $\vec{B}$ is uniform in space and time, as the Earth dipole field can be approximated at large distances from the Earth surface, the particles experience a spiral-like motion characterized by a certain radius (Larmor radius), a certain velocity component $v_{\parallel}$ in the direction parallel to $\vec{B}$, and a certain transversal velocity

component $v_\perp$. These values depend on the particle mass and energy, as well as on the magnitude of $\vec{B}$. As the particles spin up toward the magnetic pole, they experience an electric field resulting from the variation of $\vec{B}$. Since the magnetic flux across the Larmor circle is constant, so does the particle magnetic momentum $\vec{\mu_\mathrm{B}} = v_\perp / \vec{B}$. The magnitude of $\vec{B}$ increases towards the pole, so does $v_\perp$ as well. As magnetic forces do not produce work, conservation of energy entails a decrease in $v_\parallel$, i.e. the particle feels a force opposite to the direction of motion. As a result, particles approaching a pole slow down and eventually reach a mirror point [11] where they reverse the direction of $v_\parallel$ and bounce back towards the other pole. The same situation happens at the south pole. As the particles spiral up and down toward the planet poles, they are effectively trapped in the magnetic field. The dynamic of the trapped particles is sketched out in Fig. 2.2 (a). Moreover, the inhomogeneity of the magnetic field in the perpendicular direction of the force makes the particles drift around along the Earth parallels in opposite direction. The trapped particles are thus forming a radiation belt around the planet. The particle trapping lifetime is estimated to reach up to 10 years. However, particles can eventually escape out of the trapping mechanism due to collisions with neutral atoms in the ionosphere above the poles. Since the formation of the Earth and the establishment of its magnetic field, two main radiation belts have been generated, known as Van Allen belts. The inner belt, fairly quiescent, extends from 0.2 up to 2 Earth radii (one Earth radius = 6371 km) above the Earth surface. It comprises of few trapped electrons in the range of hundreds of keV and mostly protons up to 100 MeV. Not all the particles stuck in the inner belt have been originated from solar activities. At least part of the protons are believed to be formed following the decay of neutrons that are emitted from the Earth's atmosphere as it is bombarded by cosmic rays.

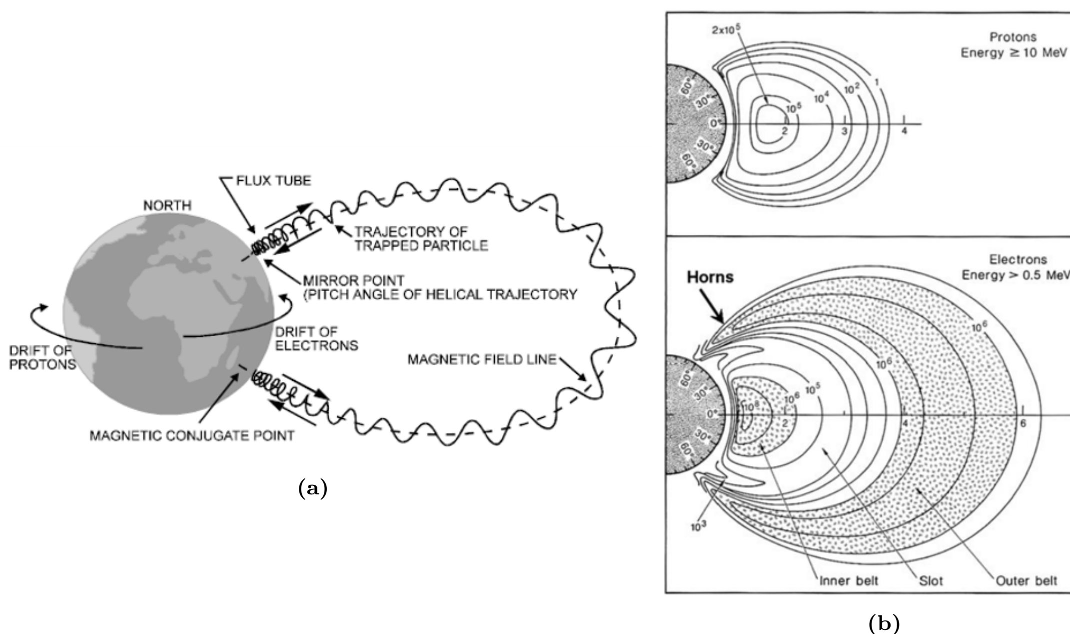

Figure 2.2 – (a) Particle trajectory, bounce and drift in Van Allen belts [12]. (b) Time averaged radiation belt omnidirectional fluxes for > 10 MeV protons (top) and > 0.5 MeV electons (bottom), according to [13].

The outer belt stretches from 3 to 10 Earth radii, and it contains high concentrations of energetic electrons in the energy range 0.1 - 10 MeV. These electrons are originated by injection from the outer magnetosphere. Unlike the inner belt, the outer belt is very dynamic in response to perturbations of the magnetosphere.
The averaged fluxes for the inner and outer belts are sketched out in Fig. 2.2 (b) according to [12].

2.1.2 Radiation environment modeling

Electron and proton environments are represented by isotropic, omnidirectional differential fluence spectra $\phi_{\mathrm{e,p}}(\xi)$ where ξ is the particle energy and $\phi_{\mathrm{e,p}}$ is in units of $\mathrm{cm^{-2}\,MeV^{-1}}$. Several models are available to the space radiation community to map a given mission orbit with the spectra $\phi_{\mathrm{e,p}}$. The spectra functions are interpreted as the total number of particles, per unit energy, that isotropically traverse a test sphere with unit cross-sectional area over a determined period of time which usually matches the entire mission duration. A common solar cell configuration in space involves infinite back shielding provided by the solar panel substrate and a finite front shield provided by the cover glass, as shown in the sketch of Fig. 2.3 (a). This situation is conveniently characterized by an unidirectional differential spectrum normally incident on the solar cell surface. The conversion from omnidirectional to unidirectional $\phi_{\mathrm{e,p}}$ is achieved via geometrical considerations, integrating the contribution from all possible incident angles over 2π steradians [14]. The conversion accounts also for the transport of the particle through the finite thickness of the shielding cover glass material. The converted spectrum ϕ_{C} is computed numerically via Geant4-based Monte Carlo MULASSIS code [15], which employs a continuous slowing-down approach to describe the transport of charged particles in the shielding material. The code is available in several software platforms such as SCREAM [16] or SPENVIS.
The omnidirectional ϕ is converted in monodirectional differential fluence ϕ_{C}, assuming infinite back shielding and front shielding due to a CMX cover glass of different thickness values. An example of omnidirectional and converted monodirectional ϕ_{C} spectra is reported in Fig. 2.3 (b). The solid line is the omnidirectional proton environment, sum of the trapped and solar protons, for a 10-years heliosynchronous low-Earth orbit (LEO) at 1500 km altitude. The dashed lines are the converted monodirectional spectra accounting for the proton transport across a CMX-based cover glass of different thicknesses. The converted spectra are calculated with the continuous slowing-down approach by means of the MULASSIS code implemented in the SCREAM software [16].
The solar cell performance under particle environment are tested by performing irradiation experiments in dedicated facilities where the solar cell is exposed to a mono-energetic radiation fluence Φ, in units of $\mathrm{cm^{-2}}$. An appropriate tool is required to condense the complex, multi-energetic spectrum of the space environment into a mono-energetic spectrum. In the last decades, the method developed at the US Naval Research Laboratory (NRL) [17], also known as the NRL method, became widely adopted by the space radiation community . The method is based on the correlation between the solar cell damage coefficients and the non-ionizing energy loss

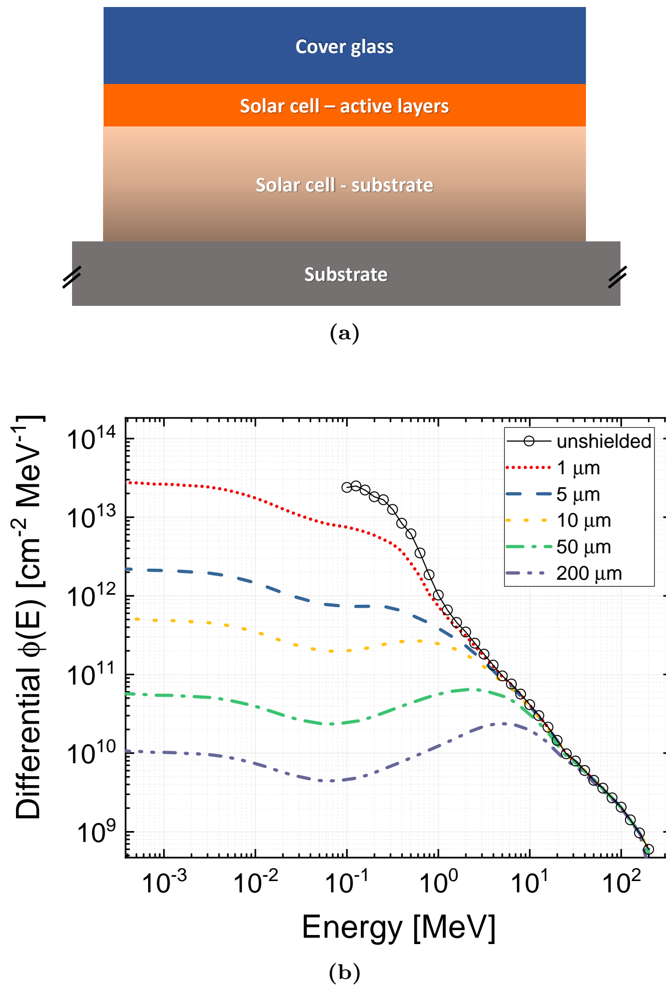

(a)

(b)

Figure 2.3 – (a) Simplified sketch of a space solar cell on a solar array. (b) Differential proton fluence in a 10 years heliosynchronous LEO orbit at 1500 km altitude. The black line is the omnidirectional spectrum, whereas the coloured lines represent the converted monodirectional spectra at the solar cell, considering infinite back shielding and a CMX cover glass of variable thickness at the front side. The monodirectional spectra are obtained by employing the MULASSIS code to compute the particle transport through the cover glass.

.

(NIEL) of the particles in the solar cell material. The degradation of a specific solar cell technology in a multi-energetic environment is obtained by performing irradiation tests with one proton and two electron energies in the MeV range. The NRL method represents a significant improvement over the Jet Propulsion Laboratory (JPL) method [17], which was adopted in the past and which required much more irradiation experiments. The physical principles and the application of the NRL method to solar cell parameter degradation in space are outlined in the following sections.

2.2 Non-ionizing collisions in semiconductor crystals

The term displacement damage refers to the stable crystallographic defects produced within the crystal of a semiconductor as a result of the non-ionizing collisions with particle radiation. A charged particle with kinetic energy ξ penetrating a crystal semiconductor loses its energy via elastic and inelastic collisions with the atoms and nuclei of the target medium. Inelastic collisions occurring between the projectile particle and the electron clouds of the target atom lead to change in the free carrier concentration via ionization, i.e., the excitation of electrons of the outer shells of the atoms resulting in electron-hole pair formation. Ionizing collisions accounts for a big fraction of the total energy deposited by the particle in the material. Nonetheless, the phenomenon does not lead to permanent degradation of the electrical properties of the semiconductor material. Elastic collisions with atomic nuclei, on the other hand, are the main source of displacement generation in a semiconductor. In these non-ionizing collisions, the energy lost by the projectile particle is transferred directly to the target atoms. If the target lattice atom gains a sufficiently high energy to break its chemical bonds, it is displaced from its position and forms a crystallographic defect. The quantification of the non-ionizing damage, also referred to as the displacement damage, requires the study of the elastic interaction between the projectile particle and the target atom. This can be described by different models according to the particle and the atom initial energies. Since the target atom is bound within a crystal, we shall assume that its initial energy equals 0. The incoming particle energy defines the model with which the collision is studied. If the energy of the particle is low enough, the nucleus of the target atom and its screening electrons leads to a collision which can be treated, in a first approximation, as an hard-sphere interaction. As the projectile particle energy increase, the collision becomes a Coulomb interaction between the particle and the atomic nucleus electric field. The latter has to be corrected to include the screening effect of the electron clouds. As the particle energy increases, the screening effect becomes lower and the collision can be treated as ordinary un-screened Rutherford collisions. The latter is usually the case for the primary collisions of protons and electrons in the MeV range on III-V atoms. A secondary source of displacements may result from inelastic collision of the projectile particles with the atomic nucleus. Fast protons and heavier ions with energies above tens of MeV can overcome the Coulomb barrier of the target atom and interact directly with the nucleus via nuclear inelastic collision, i.e., short-range nuclear interactions. This phenomenon, known also as spallation, leads to ejection of secondary particles from the target nucleus which can in turn introduce displacements in the lattice. The displacement contribution from nuclear inelastic collision, also referred to as hadronic contribution, can introduce radioactivity into the material.

2.2.1 Defect production

Next we shall analyze the scenario of a projectile particle with energy ξ colliding with a target atom from the III-V groups. This is a particle-atom interaction and it is

termed primary collision. The particle energy is considered to be below the threshold energy for inelastic nuclear collisions. A fraction of the particle energy is transferred to the atom in the non-ionizing collision. If the non-ionizing energy transferred to the target atom is higher than the threshold displacement energy for displacement E_{d_0}, the atom can be displaced from its bound position within the crystal, the value of E_{d_0} depending on the atomic species and the bond type. In GaAs, the lowest value has been measured via X-ray diffraction [18] and estimated via molecular dynamics (MD) simulations [19] to be in the range of E_{d_0} =9-13 eV, although higher values can result in the case of particular combinations of radiation and crystal orientations. The recoiling atom generated from the primary collision is termed primary knock-on (PKA) atom. In the simplest case the PKA does not have enough energy to generate further displacements ($E_{\mathrm{PKA}} < E_{\mathrm{d}_0}$) and it settles in an interstitial position within the lattice, leaving a void (vacancy) behind. The energy gained by the PKA in the elastic collision is dissipated via phonon interaction. The vacancy-interstitial pair produced in the semiconductor, known as Frenkel pair (FP), is the simplest defect structure produced by the collision. If $E_{\mathrm{PKA}} > E_{\mathrm{d}_0}$, further displacements can be generated by the recoiling PKA via secondary collisions, i.e. atom-atom collisions. We shall now examine the secondary collision of a PKA atom – characterized by its energy E_{PKA}, atomic number Z_{PKA} and the atomic mass A_{PKA} – with a target atom characterized by Z_{T}, A_{T}, and $E_{\mathrm{T}} = 0$ as initial condition. A fraction of the energy E_{PKA} is lost in ionization of electrons in the outer cloud surrounding the target nucleus, whereas the remaining energy is lost in the non-ionizing collision process leading to a potential displacement. The function quantifying the energy fraction of E_{PKA} remaining for the non-ionizing collision process is denoted as the Lindhard partition function $L(E_{\mathrm{PKA}}, Z_{\mathrm{PKA}}, Z_{\mathrm{T}}, A_{\mathrm{PKA}}, A_{\mathrm{T}})$ [20]. The non-ionizing energy transferred to the secondary target atom after the collision is given by:

$$E_{\mathrm{T}} = E_{\mathrm{PKA}}\, L(E_{\mathrm{PKA}})\,. \tag{2.1}$$

For low values of E_{PKA} in the order of few E_{d_0}, the ionization energy is negligible ($L = 1$) and the displacement collision can be treated as an hard-sphere collision. After the secondary displacement, both the PKA and the target atom can produce a displacement cascade which becomes a recursive problem. Eventually, the last recoil will not be able to produce further displacement and the cascade ends. After each collision, it can occur that the energy of the colliding atom is not enough to create further displacements. In this case, the incoming atom settles in the position of the displaced target atom, and the collision is termed replacement collision. In alloy semiconductors, if the atom-atom collision involves the same species the replacement collision does not change the unit cell configuration; vice versa, when different atomic species are involved, the effect is disruptive as it generates antisite defects. Replacement collisions are the main source of antisite generation in irradiated III-V semiconductor. Defects related to As antisite are very harmful in GaAs-based devices, as the energy level is very close to the mid gap position. The As antisite defect is often mentioned in the literature as the EL2 defect, a name which was attributed in one of the very first study of this defect in GaAs epitaxial layers [21].

In the simplest case, all the defects generated by displacements are primary defects

such as vacancies (V), interstitials (I) and antisites (e.g., As_{Ga} or Ga_{As} in the GaAs case). Combined defects might also be formed as a result of short collision cascade, such as Frenkel pairs, divacancy, trivacancy and so on. In addition, an isolated point defects may combine with dopant atoms or other impurity to form complexes. According to the distribution, orientation and the distance between single point defects, the impact on the electrical performance may vary significantly.

When the defects created by particle bombardment are widely distributed within the lattice and far enough apart from each other, they are isolated and thus act as single point defects. This is representative of a scenario where all triggered recoils have low-enough energy, so that the collision cascades generated are rather short. In the following, we will refer to these particles as low-NIEL particles, i.e., particle radiation whose displacements generate mainly isolated defects. Particles triggering recoils with higher energies, on the other hand, can introduce several displacements closely-spaced within the lattice. This facilitates the agglomeration of single point-defects in stable defect clusters. Those particles will be referred to as high-NIEL particles. The crystal defects made up of multiple single defect entities are knwon as clusters.

2.2.2 Defect reordering

The defects produced by particle radiation are formed in few picoseconds after the collision occurs. In longer time scales, the defect structure will reorder to form more stable configurations. The reordering is usually differentiated in short-term (ns to s scale) and long term reordering processes ($\gg$ s scale). The defect reordering properties are governed by the type of material, the thermal environment of the lattice (thermal reordering) and the carrier concentration (injection reordering). As space solar cells operate in a wide temperature range, the understanding of defect reordering processes is important to evaluate the final degradation of the solar cell performance. In current European space standards [22], a degradation analysis studied via the NRL method requires that the solar cells are subjected to thermal and photon annealing for a specific amount of time after irradiation experiments. The annealing temperature and duration are defined in order to produce a similar effect on the solar cells representative of the real space mission conditions. The photon annealing is usually performed by employing an AM0 spectrum, whereas the thermal annealing is usually performed at 60°C, equivalent to 333.15 K. As the annealing temperature is higher than the irradiation temperature (300 K), thermal reordering occurs during the thermal annealing. Injection reordering processes are also likely to occur during photon annealing as carriers are generated within the solar cells. The annealing phase is usually beneficial in III-V materials, meaning that the total amount of defects is reduced and the performance of the solar cells are improved, although it should be remarked that this is not a general trend.

Defect reordering occurs in materials containing defects in concentration larger than the thermodynamic equilibrium concentration. The defect concentration is brought back to the equilibrium – characteristic of the material and of the temperature – via thermodynamic processes such as migration to a sink (e.g., surface), pair recombination (e.g., vacancy-interstitial recombination) and complex formation or dissoci-

ation [23]. Each of these processes is characterized by an activation energy. Let us assume that a certain amount N_t of defects per cm^{-3} are produced in a semiconductor via a particle irradiation experiment performed at a fixed temperature T_{irr}, and all the long-term reordering dynamics occurring in the semiconductor at T_{irr} have already taken place. If the semiconductor is brought to a temperature $T > T_{irr}$, new reordering dynamics occur. The annealing kinetic can be modeled with the rate of reaction equation:

$$\frac{\mathrm{d}\, N_t(t)}{\mathrm{d}t} = -K(T)\, N_t^{\alpha}(t)\,, \tag{2.2}$$

where $K(T)$ is the rate constant and α is the order of the reaction. The value of α describes the nature of the annealing process: defects migrating to a sink lead to an unitary order of reaction ($\alpha = 1$), whereas pair recombination, such as vacancy-interstitial recombination, leads to $\alpha = 2$. In GaAs, an As interstitial (I_{As}) is mobile already at room temperature, which is the typical temperature at which the irradiation experiments are performed. Therefore, thermal reordering of I_{As} occurs already during irradiation. The activation energy for the defect annealing can be also influenced by the Fermi level (injection annealing). This occurs when the defect reordering is influenced by Coulomb forces, which varies according to the defect ionization status. Since ionization events occur already during irradiation, potential injection reordering can already occur during the irradiation experiment.

2.2.3 Characterization of the recoil damage

The understanding of the damage introduced by recoil atoms with different energy requires the study of the defect formation after collision cascades in semiconductors. The analytic approach with the Boltzmann transport equation [24] can be useful in determining the range of the cascade collision produced by a recoiling atom, but it does not provide direct information of the defects generated along the recoil track. A Monte-Carlo approach based on the binary collision approximation (BCA), on the other hand, provides information of all the displacement events occurring along the track. The BCA approach treats each collision as a two-body interaction system: the recoil and the target atom. In this way, a more detailed description of the recoil damage is obtained as the collision cascade is studied until all recoils stop in the crystal. A BCA code is implemented in the open-source SRIM software [25]. The influence of the recoil energy on the type of damage is readily understood via SRIM simulations. For instance, in Fig. 2.4 (a) the range of Ga recoil atoms of different energies in a GaAs crystal is reported. The recoil straggle is reported with the error bars. The range of the Ga atoms increase as its initial energy becomes higher. The right ordinate of Fig. 2.4 (a) indicates the total number of vacancies generated by recoils due to the Ga PKA atom. Higher Ga recoil energy entails more defects produced along the track. The 1D spatial distribution of the vacancies are reported in Fig. 2.4 (b). As the recoil energy increases, the vacancy production is spread across a larger crystal volume, thereby increasing the possibility of forming agglomerate of defects.
Several limitations can, however, lead to a misevaluation of the overall damage. The BCA approximation is only applicable for recoil energies larger than several E_{d_0}. In

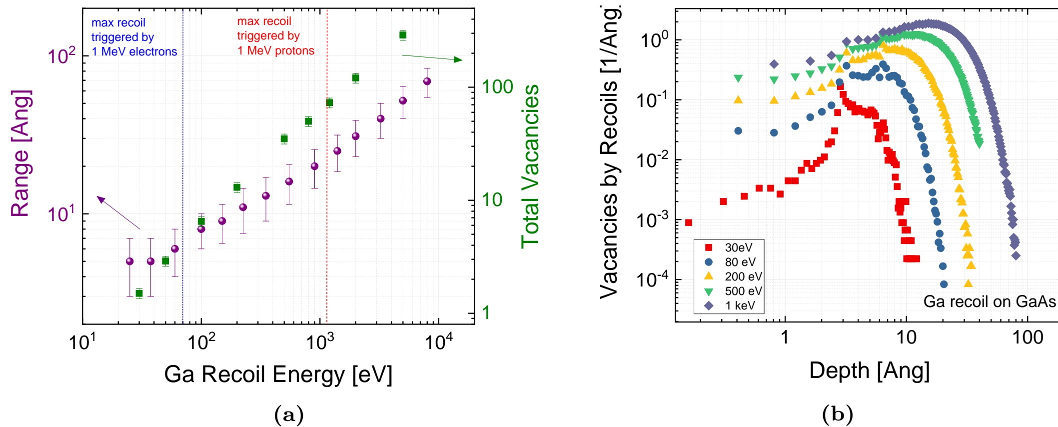

Figure 2.4 – (a) Range (spheres) and total number of vacancies (squares) produced in GaAs by a penetrating Ga recoil as a function of its kinetik energy. (b) Depth distribution of the vacancies produced by Ga recoils of different energies penetrating a GaAs layer. The particle transport is performed with the binary collision approximation (BCA), and the Monte Carlo simulations are performed with the open-source software SRIM. [25]

.

the past years, it was believed that recoils dropping below E_{d_0} dissipate their energy in the crystal via phonon interactions, thus not contributing to defect production. However, recent work [26,27] has shown that following a collision cascade, low-energy recoils below E_{d_0} can significantly contribute to the process of defect creation. The damage introduced by sub-threshold recoils is related to the formation of clustered regions, termed pockets, due to the multi-body interaction between the recoil and all the surrounding atoms. The BCA approach ignores the collective motion of the surrounding lattice atoms at the end of the collision track and thus cannot describe this dynamic. The only way to overcome the BCA limitation is to use the Molecular Dynamics (MD) approach. Even in this case, however, the long-term temperature annealing effects cannot be studied. With simple classical potentials, the MD simulation timescale are limited to the μs range [28]. Therefore, thermally activated process occurring at reasonable temperatures for space analysis cannot be directly simulated. This constitutes an important limitation in the detailed simulation of defect formation in irradiation experiments.

2.2.4 Non-Ionizing Energy Loss (NIEL)

The quantification of the displacement damage introduced in a solar cell material can be achieved by computing the total number of displacements n_{D} generated by the particle and all the possible related recoils, under the assumptions that all of the collisions generate the simplest defect, no reordering effect occurs and neglecting the non-linear processes leading to defect cluster formation. An analytical formulation for the number of displacements produced by a recoil of a given energy E_{R} was first proposed by Kinchin and Pease [29] and then modified by Norgett [30], under the assumption that primary recoils generate further displacements which can be treated as hard-sphere collisions. In this case, each collision of the cascade is treated with the BCA approach. The model forecast a linear relationship between n_{D} and the

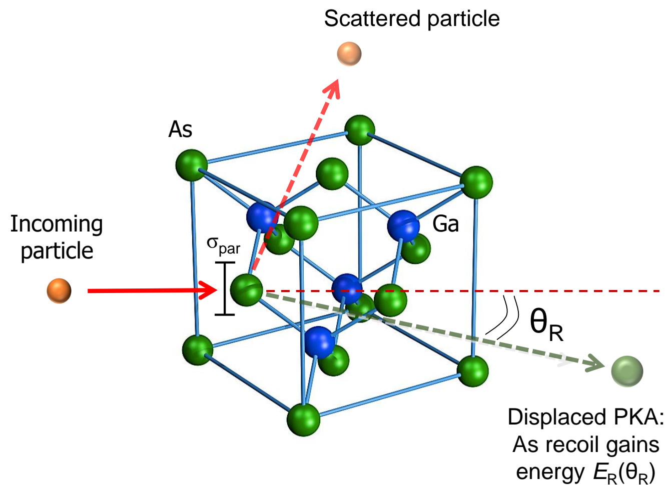

Figure 2.5 – Non-ionizing primary collision of a particle radiation (electron or proton) in GaAs lattice. The PKA is an As atom. The energy of the recoiling As atom depends on the scattering angle θ_{R}.

non-ionizing energy that all recoils transfers to the lattice. The overall non-ionizing energy deposited by each possible recoil is thus representative of n_{D}, and thus of the damage introduced by the particle itself.
This concept can be exploited to quantify the amount of non-ionizing energy (i.e., displacements) that an energetic particle can introduce into a crystal. The non-ionizing energy loss (NIEL), conveniently defined in units of MeV g^{-1} cm^2, is the energy per unit length transferred by the incident particle to the target material atoms via elastic collisions, normalized by the density of the material. The NIEL accounts for the non-ionizing energy deposited in the material by the energetic spectrum of all possible recoils generated by the incident particle at the primary collisions. It is important to address the recoil energy range that a particle can trigger, as well as the probability of each recoil to occur. The generation of recoils with different energies is a statistical process associated with the recoil scattering angle θ_{R} formed between the particle trajectory and the recoil trajectory after the collision. This is exemplary shown in the sketch for a non-ionizing collision of an incoming particle in GaAs lattice reported in Fig. 2.5. The minimum energetic recoil which can be triggered is determined by the atomic threshold energy for displacement $E_{\mathrm{min}} = E_{\mathrm{d}_0}$ of the atomic species of the target material, and is thus not dependent on the incoming particle. The maximum energy E_{max} which can be transferred to a lattice atom, on the other hand, depends on the type and energy of the incident particle. The collision can be treated as a two-body scattering problem where the incoming particle has energy ξ and the recoil nucleus is at rest. The recoil atom, if displaced, will be scattered out with scattering angle θ_{R}. By implying the energy and momentum conservation in a head-on collision ($\theta_{\mathrm{R}} = 0$), E_{max} can be evaluated. An energetic proton in the MeV range travels at a small fraction of the speed of light in vacuum c. Therefore, a simple expression of E_{max} is given by [31]:

$$E_{\mathrm{max}} = \xi \frac{4A_{\mathrm{p}}A_{\mathrm{R}}}{(A_{\mathrm{p}} + A_{\mathrm{R}})^2}\,, \tag{2.3}$$

where A_p and A_R are the atomic masses of the proton and the recoil nucleus, respectively. An electron in the same energy range travels at about 95 % of c. The formula in Eq.2.3 is corrected for relativistic effects [32]:

$$E_\mathrm{max} = \frac{2\xi(\xi + 2A_\mathrm{e}E_\mathrm{u})}{A_\mathrm{R}E_\mathrm{u}(1 + A_\mathrm{R}/A_\mathrm{e})^2 + 2\xi} \,. \tag{2.4}$$

In the latter expressions, $E_\mathrm{u} = 931.5\,\mathrm{MeV}$ is the equivalent energy of 1 atomic mass unit (amu) and A_e is the atomic mass of the electron.
The probability for the primary particle to generate a recoil with energy E_R in the range $E_{\mathrm{d}_0} < E_\mathrm{R} < E_\mathrm{max}$ can be expressed by means of the differential partial cross-section for Coulomb scattering related to the recoil energy $\partial\sigma_\mathrm{CS}/\partial E_\mathrm{R}$ [31]. For instance, the probability $P\{E_\mathrm{R} > E\}$ for an incoming particle to trigger a Ga or As recoil with energy $E_\mathrm{R} > E$ can be expressed as:

$$P\{E_\mathrm{R} > E\} = 1 - \frac{\displaystyle\int_{E_{\mathrm{d}_0}}^{E} \frac{\partial\sigma_\mathrm{CS}}{\partial E_\mathrm{R}} dE_\mathrm{R}}{\displaystyle\int_{E_{\mathrm{d}_0}}^{E_\mathrm{max}} \frac{\partial\sigma_\mathrm{CS}}{\partial E_\mathrm{R}} dE_\mathrm{R}}. \tag{2.5}$$

The determination of $\mathrm{d}\sigma_\mathrm{CS}/\mathrm{d}E_\mathrm{R}$ is crucial for an accurate determination of the NIEL. Every triggered recoil transfers to the lattice atom only a fraction of its energy in the non-ionizing collision. The fraction of the energy which goes into non-ionizing collisions is quantified by the function $L(E_\mathrm{R})$. The damage energy, i.e., the energy that each recoil deposits to displacements, is thus obtained as $E_\mathrm{NI} = E_\mathrm{R}L(E_\mathrm{R})$. The rate at which the total E_NI is deposited per unit length in a target material can be then obtained by accounting for the contribution of all recoils:

$$-\frac{\partial E_\mathrm{NI}}{\partial x} = \frac{N\rho}{A} \int_{E_{\mathrm{d}_0}}^{E_\mathrm{max}} E_\mathrm{R}L(E_\mathrm{R}) \cdot \frac{\partial\sigma_\mathrm{CS}(E_\mathrm{R}, \xi)}{\partial E_\mathrm{R}} dE_\mathrm{R} \,, \tag{2.6}$$

where x denotes the depth into the target material, N is the Avogadro number, ρ and A are the density and the atomic mass of the target nucleus, respectively. The minus sign indicates that the energy is lost along the positive direction x in the medium. Defining the area density $x' = x \cdot \rho$, the non-ionizing energy loss NIEL can be expressed in units of $\mathrm{MeVcm^2g^{-1}}$ as:

$$\mathrm{NIEL}(\xi) = -\frac{\partial E_\mathrm{NI}}{\partial x'} = -\frac{1}{\rho} \cdot \frac{\partial E_\mathrm{NI}}{\partial x} = \frac{N}{A} \int_{E_\mathrm{d}}^{E_\mathrm{max}} E_\mathrm{R}L(E_\mathrm{R}) \cdot \frac{\partial\sigma_\mathrm{CS}(E_\mathrm{R}, \xi)}{\partial E_\mathrm{R}} dE_\mathrm{R} \,. \tag{2.7}$$

The lower integral boundary is generically expressed with E_d. If the physical threshold energy for displacement ($E_\mathrm{d} = E_{\mathrm{d}_0}$) is chosen, the NIEL is marked with the subscript "0" $\mathrm{NIEL_0}$.
Eq.2.7 is used to calculate the NIEL of a particle in an elemental semiconductor. In III-V compound semiconductors, the NIEL is determined according to the Bragg's rule, i.e. a weighted sum in which each material contributes proportionally to the fraction of its atomic weight. For instance in the GaAs case:

$$\mathrm{NIEL_{GaAs}} = \frac{A_\mathrm{Ga}}{A_\mathrm{Ga} + A_\mathrm{As}} \cdot \mathrm{NIEL_{Ga}} + \frac{A_\mathrm{As}}{A_\mathrm{Ga} + A_\mathrm{As}} \cdot \mathrm{NIEL_{As}}. \tag{2.8}$$

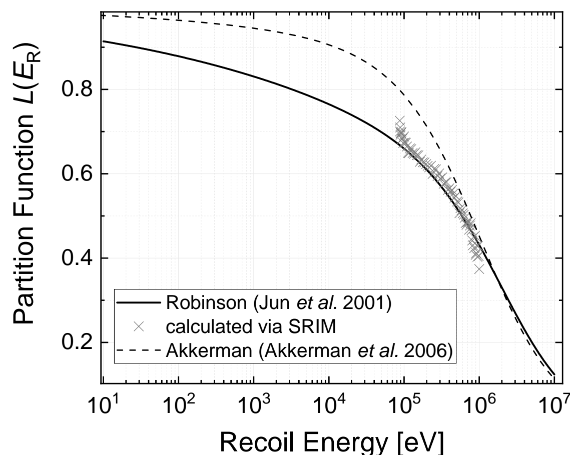

Figure 2.6 – Lindhard partition function $L(E_\mathrm{R})$ for an As atom recoiling on a Ga target atom of the GaAs crystal. The solid line is calculated with the Norgett-Robinson-Torrens formulation. The symbols are the experimental data obtained via SRIM simulation, employing a quick calculation of the damage with the Kinchin-Pease formula. The dashed line is derived according to the Akkerman formalism.

The partition function

The partition function $L(E_\mathrm{R})$ quantifies the fraction of a recoiling atom energy which goes into further atomic displacements in the crystal. Historically, the first formulation was achieved numerically by Lindhard and co-workers [20]. A convenient formulation of $L(E_\mathrm{R})$, widely adopted in the NIEL community, is given by the Norgett-Robinson-Torrens (NRT) equation [32]:

$$L(E_\mathrm{R}) = \frac{1}{1 + F_\mathrm{L} g(\epsilon_\mathrm{L})}, \tag{2.9}$$

where

$$\begin{aligned} g(\epsilon_\mathrm{L}) &= (\epsilon_\mathrm{L} + 0.40244\epsilon_\mathrm{L}^{3/4} + 3.4008\epsilon_\mathrm{L}^{1/6})\,; \\ \epsilon_\mathrm{L} &= E_\mathrm{R}/E_\mathrm{L}\,; \\ E_\mathrm{L} &= 30.724 \cdot Z_\mathrm{R} Z_\mathrm{L} \sqrt{Z_\mathrm{R}^{2/3} + Z_\mathrm{L}^{2/3}} \frac{A_\mathrm{R} + A_\mathrm{L}}{A_\mathrm{L}}\,; \\ F_\mathrm{L} &= \frac{0.0793 Z_\mathrm{R}^{2/3} Z_\mathrm{L}^{1/2} (A_\mathrm{R} + A_\mathrm{L})^{3/2}}{(Z_\mathrm{R}^{2/3} + Z_\mathrm{L}^{2/3})^{3/4} A_\mathrm{R}^{3/2} A_\mathrm{L}^{1/2}}\,. \end{aligned} \tag{2.10}$$

In the above equations, A_R and Z_R are the atomic weight and number of the recoiling nucleus, whereas A_L and Z_L are the corresponding quantities for the lattice nucleus. The $L(E_\mathrm{R})$ function for an As recoil on a Ga target atom is reported in Fig. 2.6. Low-energy recoil have $L(E_\mathrm{R})$ values approaching 1, and thus all of the damage goes into displacement. High-energy recoils, on the other hand, lose energy primarily via ionization events. The validity of the Lindhard function, which was originally formulated for high-energy recoils, has been questioned in recent years for the underestimation of the non-ionizing energy fraction at recoils approaching E_{d_0}. Akkerman *et al.* proposed a Monte Carlo approach to calculate $L(E_\mathrm{R})$ in [33]. The

results have a closer agreement with the experimental values in silicon [34]. The Akkerman expression of the partition function can be put in an NRT-like formalism of Eq. 2.9 by substituting $g(\epsilon_{\mathrm{L}})$ with $g_{\mathrm{Akk}}(\epsilon_{\mathrm{L}})$:

$$g_{\mathrm{Akk}}(\epsilon_{\mathrm{L}}) = 0.74422\epsilon_{\mathrm{L}} + 1.6812\epsilon_{\mathrm{L}}^{3/4} + 0.90565\epsilon_{\mathrm{L}}^{1/6}\,. \tag{2.11}$$

The Akkerman partition function is plotted in Fig. 2.6 with a dashed line. A bigger fraction of the low-recoil energy goes into displacements as compared to the standard Robinson formulation of the Lindhard function.

Electron cross-section

Electrons penetrating a material experience both radiative and collision energy-losses. In the electron-nucleus interaction, where the nucleus atomic number is denoted by Z, an expression for the critical energy E_{crit} separating the dominating energy losses via collision from losses via radiation can be approximated by $E_{\mathrm{crit}} = 550\,Z^{-1}$ MeV. For atomic species of interests in III-V compound semiconductors, this value approaches few tens of MeV. At energies below E_{crit}, the radiative losses can be neglected and it is sufficient to only analyze the collision-based energy loss.

The scattering of electrons by un-screened nuclei was treated first by Mott [35], extending the wave scattering on point-like nuclei theory of Wentzel. The so-called Mott differential cross-section (MDCS) for electrons is also referred to as the exact formula, since its determination involves no Born approximation of any order on the system electric field. Many authors provided an approximation of the exact MDCS, expressing their results in terms of the ratio factor $\Re$ with respect to the classical Rutherford scattering formula:

$$\frac{\mathrm{d}\sigma_{\mathrm{MDCS}}^{\mathrm{un-screened}}}{\mathrm{d}E_{\mathrm{R}}} = \Re(E_{\mathrm{R}})\frac{\mathrm{d}\sigma_{\mathrm{Ruth}}}{\mathrm{d}E_{\mathrm{R}}}\,, \tag{2.12}$$

where $\mathrm{d}\sigma_{\mathrm{Ruth}}/\mathrm{d}E_{\mathrm{R}}$ is the Rutherford scattering cross section for an incoming particle with $z = 1$:

$$\frac{\partial\sigma_{\mathrm{Rut}}(E_{\mathrm{R}},\xi)}{\partial E_{\mathrm{R}}} = \pi\left(\frac{zZe^2}{p\beta c}\right)^2\frac{E_{\mathrm{max}}}{E_{\mathrm{R}}}\,. \tag{2.13}$$

In Eq. 2.13, Z is the atomic number of the target nucleus, c is the speed of light, $\beta = v/c$ with the electron velocity v the electron velocity and p is the electron momentum. The term "un-screened" is referred to the fact that the screening effect of the electron cloud is not taken into account. In this thesis, we resort to the interpolated $\Re(E_{\mathrm{R}})$ expression provided by Boschini *et al.* in [36]. The screening effect on the atomic nucleus electric field, as well as the finite nuclear size of the target atom, is accounted for by re-writing Eq. 2.12 according to [36] and references therein:

$$\frac{\partial\sigma_{\mathrm{Mott}}(E_{\mathrm{R}},\xi)}{\partial E_{\mathrm{R}}} = \frac{\partial\sigma_{\mathrm{Rut}}(E_{\mathrm{R}},\xi)}{\partial E_{\mathrm{R}}}\cdot\Re^{\mathrm{Mott}}(E_{\mathrm{R}})\cdot\mathfrak{F}^2(E_{\mathrm{R}},\xi)\cdot|F_{\mathrm{exp}}(\xi)|^2. \tag{2.14}$$

In Eq. 2.14, $\mathfrak{F}(E_\mathrm{R})$ is the screening factor, expressed by:

$$\mathfrak{F}(E_\mathrm{R},\xi) = \frac{E_\mathrm{R}}{E_\mathrm{R} + E_\mathrm{max} A_\mathrm{s,M}}, \tag{2.15}$$

where $\mathrm{A_{s,M}}$ is the screening parameter computed as in [36]. $\mathfrak{F}(E_\mathrm{R})$ accounts for the fact that at distances larger than the Bohr radius from the target nucleus the nuclear field experienced by the incoming particles is screened by the electron cloud surrounding the atom.
$F_\mathrm{exp}(E_\mathrm{R})$ is the form factor computed with the exponential charge distribution, which accounts for the finite nuclear size. An expression for F_exp is given in [31]:

$$F_\mathrm{exp}(\xi) = \left[1 + \frac{1}{12}\left(\frac{q' r_\mathrm{n}}{\hbar}\right)^2\right]^{-2}, \tag{2.16}$$

where $\hbar$ is the reduced Plank constant, $r_\mathrm{n} = 1.27 A^{0.27}$ in units of fm, is the nuclear radius with A the atomic weight, and the momentum transfer q' to the target atom with mass M is given by:

$$q' = \frac{\sqrt{E_\mathrm{R}(E_\mathrm{R} + 2Mc^2)}}{c}; \tag{2.17}$$

Eq. 2.14 expressed in the center-of-mass (CoM) system is used to calculate the NIEL. The NIEL for GaAs is plotted with open circles in Fig. 2.7 (a). The values obtained are in accordance to the NIEL computed with the online SR-NIEL calculator from the INFN [37], reported in Fig. 2.7 (a) with a solid line. The dashed line in Fig. 2.7 (a) is the electron NIEL calculated with the Akkerman formalism for $L(E_\mathrm{R})$. The NIEL values differ from the one calculated with the NRT formalism by 14% at most.

Proton cross-section

Several expressions of the hydrogen ion differential cross-section in solids have been proposed in the literature. The Ziegler-Biersack-Littmark (ZBL) screened formulation takes into account the reduction of the Coulomb barrier due to the electrostatic screening of the nuclear charges by the innermost electron shells. The ZBL approach is only suitable in cases where the velocity of the ion is a small fraction of c. For the relativistic cases, the Mott-Rutherford and the Wentzel-Moliere differential cross sections shall be used. No analytic model is available to calculate the nuclear inelastic differential cross section, which accounts for the spallation products. We resort to the hadronic contribution data available in the literature (e.g., [32] and [37]). In our case of study, protons have only a small fractions of c, thus the ZBL potential can be adopted with good margins. An expression for the ZBL differential cross section is given in [38] and references therein:

$$\frac{\partial \sigma_\mathrm{ZBL}(E_\mathrm{R},\xi)}{\partial E_\mathrm{R}} = -\frac{\pi a_\mathrm{U}^2}{2}\frac{f_\mathrm{TF}\sqrt{E_\mathrm{max}}}{\epsilon_\mathrm{ZBL} E_\mathrm{R}^{3/2}}, \tag{2.18}$$

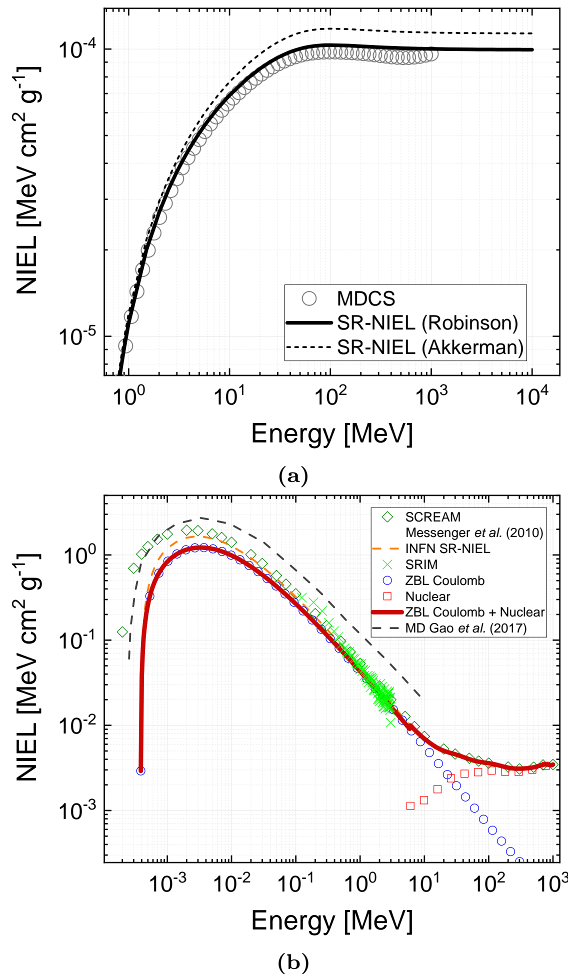

Figure 2.7 – (a) Screened electron NIEL in GaAs with $E_{\mathrm{d}} = 21\,\mathrm{eV}$ computed with the MDCS expression in Eq. 2.14 (open symbols). The reference NIEL calculated with the online SR-NIEL code is superimposed with a solid line. The dotted line is the equivalent SR-NIEL calculated with the Akkerman partition function. (b) Proton NIEL in GaAs with $E_{\mathrm{d}} = 21\,\mathrm{eV}$, computed with the universal ZBL potential (red solid line). The nuclear inelastic contribution is calculated with the SR-NIEL. NIEL curves calculated by other authors are superimposed.

where a_{U} is the ZBL universal screening length, expressed by;

$$a_{\mathrm{U}} = \frac{0.8854\, a_0}{Z_{\mathrm{R}}^{0.23} + Z_{\mathrm{L}}^{0.23}}, \tag{2.19}$$

being a_0 the Bohr radius of the hydrogen atom; ϵ_{ZBL} is the dimensionless ZBL reduced energy, given by:

$$\epsilon_{\mathrm{ZBL}} = \frac{32530 A_{\mathrm{R}} \xi}{Z_{\mathrm{R}} Z_{\mathrm{L}} (A_{\mathrm{R}} + A_{\mathrm{L}})(Z_{\mathrm{R}}^{0.23} + Z_{\mathrm{L}}^{0.23})}; \tag{2.20}$$

f_{TF} is the Thomas-Fermi scattering function obtained via the reduced nuclear stopping power cross section by using the exact coefficients of the ZBL Universal interatomic potential [38]. The NIEL obtained with Eq. 2.18 in GaAs is shown in Fig. 2.7 (b) with blue open circles. The nuclear contribution, depicted with red

squares, accounts for a significant fraction of the total NIEL of high-energy protons. The nuclear contribution is obtained with the help of the online simulator SR-NIEL [37]. The ZBL proton NIEL corrected for the nuclear contribution is plotted with a red solid line. These NIEL values are used throughout the dissertation. Proton NIEL curves in GaAs reported by other authors are superimposed in Fig. 2.7 (b). The NIEL computed with the Wentzel-Moliere expression for the differential cross-section is plotted with an orange dotted line. The NIEL calculated with the SRIM code, by converting the point-defect formation rate using the modified K-P formula [39] is reported with green crossess. The NIEL calculated by Messenger *et al.* with the SCREAM code is reported with green open diamonds. A variation below 5% is observed for all the proton NIEL curves in the energy range of interest for our work, partly ascribed to a different choice of E_{d}.

2.3 NIEL scaling

The defects introduced by displacements degrades the performance of the solar cell. We shall next consider the case of a solar cell irradiated with an energetic particle ξ at different fluence levels Φ. On the basis of the fundamental equations of the solar cell, it is possible to obtain analytical expressions relating the degradation of a generic solar cell parameter Y to Φ. In general, such expressions are of the form:

$$Y(\Phi) = f\big(Y(0),\, \mathrm{RC}(\xi)\,\times\,\Phi\big)\,, \tag{2.21}$$

where $Y(0)$ is the begin-of-life (BOL) value (prior to irradiation) for the Y parameter and the radiation coefficient $\mathrm{RC}(\xi)$ scales the degradation effect of Φ. The derivation of Eqs. 2.21 for the solar cell main electrical parameters, as well as the relationship between the RCs and the defect electrical parameters are given in Chapter 2.4.
When an RC is observed to vary with the particle type and energy in a way proportional to the NIEL in the solar cell material, the concept of the NIEL scaling is said to apply. If the RC satisfies the NIEL scaling principle, the parameter degradation is unequivocally correlated to the displacement damage deposited by the radiation into the solar cell. In the solar cell radiation community, the application of the NIEL scaling is also known as Displacement Damage Dose (DDD) method [17] .

2.3.1 Displacement Damage Dose (DDD) method

The DDD concept relies on the proportionality existing between the degradation of the cell parameter Y and the defects introduced by the displacement damage. For mono-energetic irradiation experiments, the $\mathrm{DDD}(\xi)$, in units of MeV g^{-1}, is computed as:

$$\mathrm{DDD}(\xi) \;=\; \mathrm{NIEL}(\xi) \times \Phi\,. \tag{2.22}$$

If the energy dependency of the RC of the Y parameter is linearly proportional to the NIEL, the plot of Y versus DDD for different particles and energies leads to a unique degradation curve. It follows that, with the knowledge of the damage coefficient of a given parameter Y for a reference particle/energy, it is possible to predict the degradation of Y after irradiation with other particle types with different

energies. The DDD analysis shall be applied separately for each single parameter of interest, as the damaging effectiveness of the introduced defects affects the different solar cell parameters in different ways. Moreover, the RC-NIEL linear correlation for the Y parameter may be violated due to a non-linear relationship between the NIEL and the damaging effectiveness of a given defect. The non-linearity is most appreciated when combining degradation data due to low-NIEL particles (electrons) with high-NIEL particles (protons). Therefore, an electron and proton DDD for each Y parameter has to be calculated separately. The approach adopted in this work to treat the degradation data of each cell parameter relies on the revisited NRL method laid down in [40]. The procedure consists of two main steps:

1. The NIEL describing the energy-dependent degradation of the Y parameter is found by adjusting the values of E_d related to the single atomic species of the cell active layer material. The experimental Y data are fitted with the expected relation given by Eq. 2.21, with Φ replaced by the electron DDD (D_e) in Eq. 2.22. The optimum E_d values are obtained as the ones that minimize the fit rms error. The resulting NIEL describes well the energy-dependent electron degradation of the Y parameter. Only the electron data are considered in this step, as the electron NIEL is more sensitive to the E_d values as the proton NIEL in the energy range of interest.

2. The E_d values determined in step 1) are used to calculate the proton DDD (D_p). If a mismatch is observed between the Y-D_e and Y-D_p curves, D_p is multiplied by a correction factor $\mathrm{R_{ep}}$ so that the two curves Y-D_e and Y-D_p coincide.

The total dose considering mono-energetic particle experiment is thus obtained as $\mathrm{DDD} = \mathrm{R_{ep}^{-1}}\, D_\mathrm{e} + D_\mathrm{p}$, where the factor $\mathrm{R_{ep}}$ is used to convert the electron dose in an equivalent proton dose. In a multi-energetic environment expressed by the functions $\phi_\mathrm{e}(\xi)$ and $\phi_\mathrm{p}(\xi)$, the total dose is computed as:

$$\mathrm{DDD} = \int_\xi \left(R_\mathrm{ep}^{-1}\, \mathrm{NIEL_e} \cdot \phi_\mathrm{e} + \mathrm{NIEL_p} \cdot \phi_\mathrm{p} \right) \mathrm{d}\xi \,. \tag{2.23}$$

2.3.2 Limits of applicability

In order to reproduce the degradation effects due to the amount of DDD experienced in space, on-ground solar cell testing campaign with electron and proton irradiation experiments are required. The choice of the particle type and energy for on-ground testing is subjected to two main constraints. The first imposes that the irradiated volume should be big enough to contain the longest cascade triggered by the recoil with the highest energy. This condition is invalidated only in high-energy proton cases (>50 MeV), which are not of concern for this study. The second condition imposes a constraint on the maximum thickness allowed for the active regions of the solar cell. The projectile particle loses energy as it travels through the solar cell. The energy of the particle is thus position-dependent within the cell. The DDD method entails constant particle energy throughout the whole irradiated thickness. If the solar cell is thin enough, the particle slow-down is negligible and the DDD

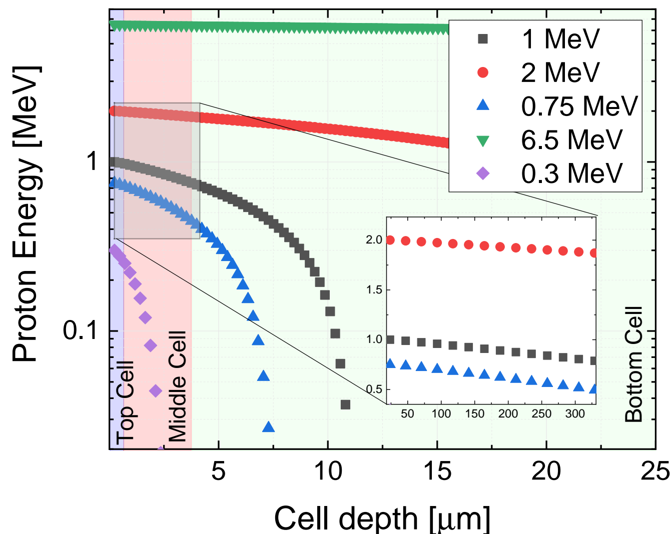

Figure 2.8 – Energy loss in ionization events of proton with different initial energies impinging normally on a representative triple-junction solar cell structure. The data are obtained with the help of the SRIM code [25].

method can be applied. For electrons this is of no concern, since the range at typical energies of interest is by far beyond the typical cell thicknesses. Low-energy protons, however, can invalidate the DDD method for common space architectures.
A simulation of the proton transport through a typical triple-junction solar cell structure is performed with the SRIM code and reported in Fig. 2.8 for different proton initial energies ranging from 0.3 MeV to 6.5 MeV.
The proton slow-down is negligible for all proton energies with regards to the top cell. This is not the case for the middle cell. The Bragg peak of a 0.3 MeV proton lies exactly within the middle cell active layer. Therefore, 0.3 MeV protons cannot be used in the DDD method for the GaAs middle sub-cell. The Bragg peak of a 0.75 MeV proton lies in the bottom cell, nevertheless the DDD approach is still not strictly applicable for the middle cell since the proton energy varies significantly within the solar cell layer. For these cases, care must be taken in evaluating the degradation data, and appropriate corrections may apply.

2.3.3 Physical interpretation

The DDD can be interpreted as the amount of energy per unit mass of traversed material that a particle radiation loses via non-ionizing collisions which generate displacements, and is thus proportional to the number of simple Frenkel pairs generated in the material in the first collision event. The method is customarily used in space radiation modeling to describe the degradation of the solar cell macroscopic parameters such as J_{SC}, V_{OC} and P_{MP} in a complex radiation environment. The need of ad-hoc, empirically-determined factors such as E_{d} values and $\mathrm{R_{ep}}$ is due to a non-direct physical relationship existing between the solar cell macroscopic parameter degradation and the number of displacements theoretically introduced by the particle radiation. A physical interpretation of the DDD should aim to identify the microscopic solar cell parameters which are more closely related to the displacement

defects. In this thesis, the DDD is applied on the introduction rate of radiation-induced defects sampled via defect spectroscopy techniques.
At this physical level of damage, the interpretation of the DDD method is much more straightforward and can lead to physical insights related to the macroscopic parameter degradation, as well as to a better understanding of the empirical factor adopted in the DDD method.

2.4 Radiation damage coefficients

The ultimate effect of crystal defects affecting the electrical and optical properties of the semiconductor device is understood in terms of energy levels introduced in the band gap of the active material. The radiation-induced levels result in several effects: reduction of recombination lifetime and diffusion length of carriers in the solar cell layers, increase in carrier trapping cross-sections, change in majority carrier concentration (i.e., compensation) and enabling of carrier trap-assisted tunneling. For very high-dose radiation, other material parameters such as the mobility can be reduced. The carrier non-radiative recombination occurring at the defect site is one of the most deteriorating mechanism for the solar cell electrical performance. The density of states E within the band gap associated to the presence of the crystal point defect has usually a sharp feature and it can be discretized in a single energy level E_t. For a given point defect structure and a surrounding ordered lattice, the associated E_t can be theoretically estimated via ab-initio calculation methods such as the density functional theory (DFT). Several repositories of numerically-calculated energy levels associated to different types of native point defects in GaAs are present in the literature [41, 42]. However, the calculated values exhibit rather big quantitative differences among different authors.
As the energy level is exposed to electron and hole fluxes, four main interaction of the defect with free carriers can occur: capture and emission of electrons from the conduction band E_C and capture and emission of holes from the valence band E_V. The capture rate of electrons (n) and holes (p) in an empty trap (here the term empty is relative to the type of carrier to be captured) is determined by the free carrier availability at the respective bands and the average probability per unit time that an electron or hole is captured into the empty state. The latter is denoted as capture constant $c_\mathrm{n,p}$ [43]. If v_th denotes the carrier velocity at the edge of its respective band, then $c_\mathrm{n,p} = v_\mathrm{th} \cdot \sigma_\mathrm{n,p}$, where $\sigma_\mathrm{n,p}$ are the capture cross-sections for n and p, defined in the same way as for nuclear interactions. The carrier emission rate from the trap depends on the number of carriers populating the trap and on the emission constant $e_\mathrm{n,p}$, defined in analogy to $c_\mathrm{n,p}$. At the thermal equilibrium, the state occupancy probabilities are governed by the Fermi-Dirac statistics, and the following relationship between $e_\mathrm{n,p}$ and $c_\mathrm{n,p}$ exists:

$$\frac{e_\mathrm{n,p}}{c_\mathrm{n,p}} = \exp\left(- |E_\mathrm{t} - E_\mathrm{C,V}|/kT \right), \tag{2.24}$$

with k being the Boltzmann constant. For non-degenerate semiconductors, the net recombination rate of charge carriers U via a deep energy level E_t and homogeneously

distributed within the material with a concentration N_t in cm^{-3} is expressed by [43]:

$$U = \frac{\sigma_\mathrm{n}\sigma_\mathrm{p}v_\mathrm{th}N_\mathrm{t}(pn - n_\mathrm{i}^2)}{\sigma_\mathrm{n}\left(n + n_\mathrm{i}e^{\frac{\mathrm{E_t - E_i}}{\mathrm{kT}}}\right) + \sigma_\mathrm{p}\left(p + n_\mathrm{i}e^{\frac{\mathrm{E_i - E_t}}{\mathrm{kT}}}\right)}. \tag{2.25}$$

In Eq. 2.25, n_i and E_i denote the intrinsic carrier concentration and intrinsic Fermi level, respectively. According to the values of n and p, the sign of Eq. 2.25 is positive or negative according to whether recombination or generation rate prevails, respectively, driving the system back to its thermodynamic equilibrium. The value of U is governed by the electrical properties of the irradiation-induced defects, namely N_t, E_t and $\sigma_\mathrm{n,p}$. The carrier recombination rate plays a major role in the current distribution through the device governed by the continuity equations, which can be written in the one-dimensional case:

$$\begin{aligned} \frac{\partial n}{\partial t} &= G - U + \frac{1}{q}\frac{\partial}{\partial x} \times \left(q\mu_\mathrm{n}nF + qD_\mathrm{n}\frac{\partial n}{\partial x}\right); \\ \frac{\partial p}{\partial t} &= G - U - \frac{1}{q}\frac{\partial}{\partial x} \times \left(q\mu_\mathrm{p}pF - qD_\mathrm{p}\frac{\partial p}{\partial x}\right). \end{aligned} \tag{2.26}$$

In Eq. 2.26, G is the generation rate due to optical excitation, $\mu_\mathrm{n,p}$ are the carrier mobilities, $D_\mathrm{n,p}$ are the diffusion constants and F is the electric field.
The understanding of the defect influence on the solar cell electrical parameter starts from Eq. 2.25. We shall next obtain relationship on the variation of U when the solar cell is irradiated with a mono-energetic particle beam with a variable fluence Φ. Equation 2.25 can be rewritten as:

$$U = \frac{pn - n_\mathrm{i}^2}{\tau_\mathrm{p}\left(n + n_\mathrm{i}e^{\frac{\mathrm{E_t - E_i}}{\mathrm{kT}}}\right) + \tau_\mathrm{n}\left(p + n_\mathrm{i}e^{\frac{\mathrm{E_i - E_t}}{\mathrm{kT}}}\right)}, \tag{2.27}$$

where $\tau_\mathrm{n,p}$ are the non-radiative carrier lifetimes associated to the defect energy level:

$$\tau_\mathrm{n,p} = \frac{1}{\sigma_\mathrm{n,p}v_\mathrm{th}N_\mathrm{t}}. \tag{2.28}$$

If the irradiation is such that collisions generate isolated point defects well spaced and distributed within the lattice, N_t is linearly dependent on the particle fluence Φ via:

$$N_\mathrm{t}(\Phi) = N_\mathrm{t}(0) + k_\mathrm{t}\Phi\,. \tag{2.29}$$

The coefficient k_t denotes the defect introduction rate. If the defect is already introduced in the crystal during the growth process, $N_\mathrm{t}(0)$ denotes its initial concentration, also referred to as begin-of-life (BOL) concentration.
The carrier lifetime $\tau_\mathrm{n,p}$ associated to each defect is influenced by the defect electrical parameters via Eq. 2.28 If $\sigma_\mathrm{n,p}$ is an invariant defect property on Φ, in any region of the solar cell $\tau_\mathrm{n,p}$ can be written as:

$$\frac{1}{\tau_\mathrm{p,n}(\Phi)} = \frac{1}{\tau_\mathrm{p,n}(0)} + k_\tau\Phi\,, \tag{2.30}$$

with $k_\tau = \sigma_{\mathrm{p,n}} v_{\mathrm{th}} k_{\mathrm{t}}$. The value $\tau_{\mathrm{p,n}}(0)$ is the BOL lifetime prior to irradiation. The non-radiative lifetime dominates over all the other lifetime contributions and therefore it influences the carrier diffusion length in the material, which in turns affects the collection efficiency of the solar cell. The carrier diffusion length $L_{\mathrm{n,p}}$ is governed by $L_{\mathrm{n,p}} = \sqrt{D_{\mathrm{n,p}} \tau_{\mathrm{n,p}}}$. Assuming the electron and hole mobility $\mu_{\mathrm{n,p}}$ to be radiation-independent, an expression for $L_{\mathrm{n,p}}$ is obtained:

$$\frac{1}{L^2_{\mathrm{p,n}}(\Phi)} = \frac{1}{L^2_{\mathrm{p,n}}(0)} + k_{\mathrm{L}} \Phi \,, \tag{2.31}$$

where $k_{\mathrm{L}} = D^{-1}_{\mathrm{p,n}} k_\tau = D^{-1}_{\mathrm{p,n}} \sigma_{\mathrm{p,n}} v_{\mathrm{th}} k_{\mathrm{t}}$.
We shall now use these equations to describe the Φ-dependencies of the solar cell dark current parameters as well as the photovoltaic parameters, namely J_{SC} and V_{OC}. The degradation of each parameter Y is expressed as its post-irradiation remaining factor RF:

$$\mathrm{RF}(Y) = Y(\Phi)/Y(0) \,, \tag{2.32}$$

where $Y(0)$ denotes the BOL value of the parameter Y prior to irradiation.

2.4.1 Dark current

Insights on the junction material quality are obtained from the current density-voltage (J_{dark}-V or simply J-V) characteristics of the device measured under dark conditions. According to the formalism developed by Shockley and co-workers [43, 44], the dark current in a single-junction solar cell is described with the conventional two-diode model:

$$J_{\mathrm{dark}} = J_{01}(e^{qV/kT} - 1) + J_{02}(e^{qV/2kT} - 1) \,. \tag{2.33}$$

In Eq. 2.33, the term J_{01} denotes the drift-diffusion current density whereas the term J_{02} denotes the recombination current density occurring in the space-charge region (SCR) of the solar cell. We shall next consider an abrupt, asymmetric n$^+$-p junction solar cell with $N_{\mathrm{a}} \ll N_{\mathrm{d}}$, N_{a} being the concentration of the acceptor atoms in the p-type (absorber) and N_{d} the concentration of the donor atoms in the n-type material (emitter). The schematic of the junction is sketched out in Fig 2.9. Under low-level injection and with Δn denoting the excess minority carriers in the p-type semiconductor, Eq. 2.27 in the base reduces to:

$$U = \frac{\sigma_{\mathrm{n}} \sigma_{\mathrm{p}}\, v_{\mathrm{th}} N_{\mathrm{t}} \Delta n N_{\mathrm{a}}}{\sigma_{\mathrm{p}} \left[N_{\mathrm{a}} + n_{\mathrm{i}} \exp\left(\frac{E_{\mathrm{i}} - E_{\mathrm{t}}}{kT}\right) \right]} \approx \frac{\Delta n}{\tau_{\mathrm{n}}} . \tag{2.34}$$

A similar relation holds for holes in the n-type material. As the majority carrier population in the neutral regions is by far larger than the minorities, the recombination rate is governed by the minority capture rate. It results that the recombination rate is fairly independent of the energy level position of the recombination center within the band gap, provided that the levels are deep enough so that the majority emission is negligible. A complete expression for J_{01} is obtained by solving Eq. 2.26

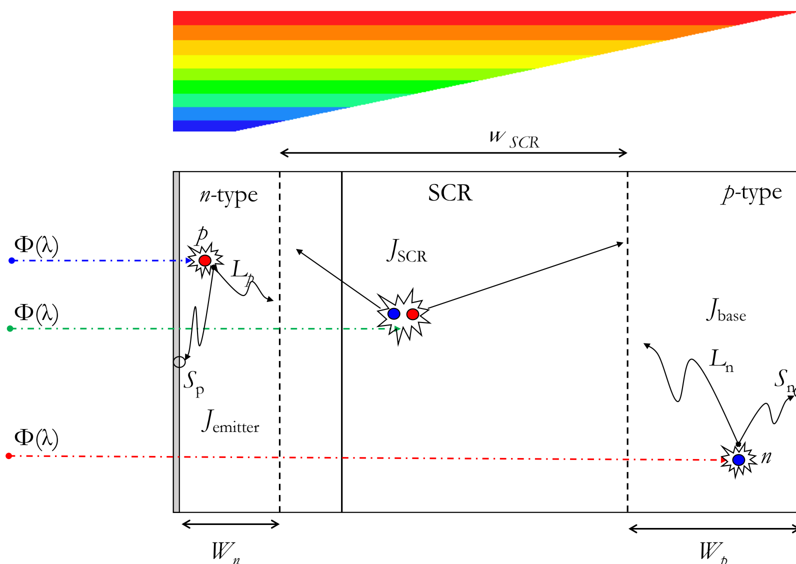

Figure 2.9 – Schematic 1D representation of an abrupt, asymmetric n$^+$-p junction.

with Eq. 2.34 in the neutral regions:

$$J_{01} = \frac{qD_n n_i^2}{L_n N_a} \times \frac{1 + \frac{D_n}{S_n L_n} \tanh \frac{W_p}{L_n}}{\tanh \frac{W_p}{L_n} + \frac{D_n}{S_n L_n}} + \frac{qD_p n_i^2}{L_p N_d} \times \frac{1 + \frac{D_p}{S_p L_p} \tanh \frac{W_n}{L_p}}{\tanh \frac{W_n}{L_p} + \frac{D_p}{S_p L_p}} . \tag{2.35}$$

W_p and W_n are the width of the neutral regions in the p-type and n-type material, respectively; S_n is the recombination velocity of electrons at the back interface, whereas S_p is the respective quantity for holes at the front interface. If $L_n << W_p$ and $L_p << W_n$, minority-carriers recombine before reaching the external interfaces. By using the linear approximation for the hyperbolic tangent functions, the J_{01} term becomes:

$$J_{01} = J_{01,n} + J_{01,p} = \frac{qD_n n_i^2}{N_a\sqrt{D_n \tau_n}} + \frac{qD_p n_i^2}{N_d\sqrt{D_p \tau_p}} . \tag{2.36}$$

The current is dominated by the recombination in the neutral regions of the materials. Assuming negligible carrier removal contribution and by substituting Eq. 2.30 in Eq. 2.36 we obtain:

$$J_{01}(\Phi) = J_{01,n}(0)\sqrt{1 + k_{\tau_n}\tau_n(0)\Phi} + J_{01,p}(0)\sqrt{1 + k_{\tau_p}\tau_p(0)\Phi} \tag{2.37}$$

If the base contribution $J_{01,n}$ outweighs the emitter $J_{01,p}$, the approximated expression of Eq. 2.37 can be used so that:

$$J_{01}(\Phi) \approx J_{01}(0)\sqrt{1 + k_\tau \tau(0)\Phi} , \tag{2.38}$$

and in terms of remaining factor:

$$RF(J_{01}) = \sqrt{1 + k_{J_{01}}\Phi} , \tag{2.39}$$

with $k_{J_{01}} = \tau_n(0) k_{\tau_n}$.
This relation, however, should be handled with care for several reasons. First and foremost, the assumption of $S_{n,p} = 0$ has been made, whereas a rigorous analysis should account also for $S_{n,p}(\Phi)$ as the quality of the interface inevitably degrades with irradiation and in thin-film solar cells this may lead to performance degradation [45]. Moreover, the minority-carrier lifetime in the base (τ_n) and emitter (τ_p) of GaAs cells have very different BOL values and degradation rates, thus invalidating the approximation made in Eq. 2.38.
The term J_{02} accounts for the current density generated by the recombination occurring within the SCR. As n and p are comparable and position-dependent within the SCR, the position of the energy level in the band gap plays a role in determining the net recombination rate. By assuming a single, discrete level located at mid-gap position, a simplified expression for J_{02} results [46]:

$$J_{02} = \frac{\pi}{2} \frac{kTn_i}{F\,\tau_{SCR}}, \tag{2.40}$$

where F is the electric field at the maximum recombination point in the SCR, corresponding to the location where $c_n n = c_p p$, and $\tau_{SCR} = \sqrt{\tau_n \tau_p}$ is the SCR lifetime corresponding to the geometrical mean of τ_n and τ_p in the SCR. Also in this case, it is possible to write:

$$J_{02}(\Phi) = J_{02}(0)\left(\sqrt{1+\tau_n(0)k_{\tau_n}} + \sqrt{1+\tau_p(0)k_{\tau_p}}\right) \approx J_{02}(0)\left(1 + k_{\tau_{scr}}\tau_{scr}\right) \tag{2.41}$$

which then leads to:

$$RF(J_{02}) = 1 + k_{J_{02}}\Phi, \tag{2.42}$$

with $k_{J_{02}} = \tau_{SCR} k_{\tau_{SCR}}$. The relation found for J_{02} in Eq. 2.42 is more reliable than the corresponding J_{01} equation, as the Φ-dependence of J_{02} is dominated by the SRH lifetime τ_{SCR} which follows inevitably Eq. 2.30. A more detailed investigation on the J_{02} term is carrier out in Chapter 5.

2.4.2 Short-circuit current density

The photo-current density J_{SC} is the current generated by the photon spectrum $\phi_\gamma(\lambda)$ and collected by the junction while operating in short-circuit conditions. Denoted as $\alpha(\lambda)$ the absorption coefficient of the material, the generation contribution G can be written according to the Lambert-Beer law:

$$G(\lambda, x) = \alpha(\lambda)\phi_\gamma(\lambda, 0)\exp(-\alpha x), \tag{2.43}$$

where $\phi_\gamma(\lambda, 0)$ is the photon flux at the surface of the material ($x = 0$) and x denotes the depth into the solar cell. We shall now calculate the current generation in the n^+–p junction sketched out in Fig. 2.9 in a configuration where the photon spectrum comes from the emitter side and $x = 0$ corresponds to the emitter surface. J_{SC} is the sum of the three current components generated in the emitter (W_e), the base (W_p) and the SCR (W_{SCR}) of the solar cell:

$$J_{SC} = \int_\lambda \int_{W_n+W_p+W_{SCR}} (J_{emitter} + J_{base} + J_{SCR})\, d\lambda dx. \tag{2.44}$$

Each contribution is obtained by using appropriate formula for G (Eq. 2.43) and U (Eq. 2.34) and by solving Eq. 2.26 in the device region of interest. The current in the emitter can be written as [47]:

$$J_{\text{emitter}} = \frac{q\phi_\gamma(1-R_\gamma)\alpha L_{\text{n}}}{\alpha^2 L_{\text{n}}^2 - 1} \times$$
$$\times \left[\frac{\left(\frac{S_{\text{p}} L_{\text{p}}}{D_{\text{p}}} + \alpha L_{\text{p}}\right) - e^{-\alpha W_{\text{n}}} \left(\frac{S_{\text{p}} L_{\text{p}}}{D_{\text{p}}} \cosh \frac{W_{\text{n}}}{L_{\text{p}}} + \sinh \frac{W_{\text{n}}}{L_{\text{p}}}\right)}{\frac{S_{\text{p}} L_{\text{p}}}{D_{\text{p}}} \sinh \frac{W_{\text{n}}}{L_{\text{p}}} + \cosh \frac{W_{\text{n}}}{L_{\text{p}}}} - \alpha L_{\text{p}} e^{-\alpha W_{\text{n}}} \right], \quad (2.45)$$

where $R_\gamma(\lambda)$ and $\alpha(\lambda)$ are the wavelength-dependent reflection and absorption coefficients, respectively. The current in the base layer of the solar cell is expressed as [47]:

$$J_{\text{base}} = \frac{q\phi_\gamma(1-R_\gamma)\alpha L_{\text{n}}}{\alpha^2 L_{\text{n}}^2 - 1} e^{-\alpha(W_{\text{n}}+W_{\text{SCR}})} \left\{ \alpha L_{\text{n}} - \right.$$
$$\left. - \frac{\frac{S_{\text{n}} L_{\text{n}}}{D_{\text{n}}} \left(\cosh \frac{W_{\text{p}}}{L_{\text{n}}} - e^{-\alpha W_{\text{p}}}\right) + \sinh \frac{W_{\text{p}}}{L_{\text{n}}} + \alpha L_{\text{n}} e^{-\alpha W_{\text{p}}}}{\frac{S_{\text{n}} L_{\text{n}}}{D_{\text{n}}} \sinh \frac{W_{\text{p}}}{L_{\text{n}}} + \cosh \frac{W_{\text{p}}}{L_{\text{n}}}} \right\}. \quad (2.46)$$

The current in the SCR is obtained under the assumption that photo-generated carriers are swept out in the respective neutral regions by the high electric field preventing any recombination ($U = 0$):

$$J_{\text{SCR}} = q\phi_\gamma(1-R_\gamma) e^{-\alpha W_{\text{n}}} (1 - e^{-\alpha W_{\text{SCR}}}) \quad (2.47)$$

In contrast to the saturation current densities, no simple equation describing the degradation of the photo-current density from the fundamental physical damage can be derived. There have been few attempts to arrive at an analytical relationship starting from fundamental physical laws [48, 49]. However, the authors adopted assumptions in their calculations which are not of general validity and not suitable for GaAs-based solar cell degradation. That is the reason why the J_{SC} degradation is usually described by the semi-empirical relationship:

$$\text{RF}(J_{\text{SC}}) = \frac{J_{\text{SC}}(\Phi)}{J_{\text{SC}}(0)} = 1 - C \log\left(1 + \frac{\Phi}{\Phi_{\text{crit}}}\right). \quad (2.48)$$

This equation implies that J_{SC} is characterized by a two-stage degradation behavior: it remains fairly constant for $\Phi < \Phi_{\text{crit}}$, whereas for $\Phi > \Phi_{\text{crit}}$ a linear behavior J_{SC}–$\log(\Phi)$ results, with the parameter C defining the slope of the characteristic curve. The C parameter tends to be constant for a given solar cell material, so that the parameter Φ_{crit}^{-1} can be treated as the radiation coefficient (RC) for J_{SC}, as defined in Section 2.3. It should be pointed out, however, that Φ_{crit}^{-1} does not correlate directly

with the physical damage introduced into the solar cell due to the semi-empirical nature of Eq. 2.48
The reason behind the two-stage degradation mechanism can be qualitative understood from the influence of $L_{\rm n,p}$ on the base and emitter collection efficiency, respectively. By focusing only on the base contribution, $L_{\rm n}$»$W_{\rm p}$ at BOL and all carriers generated in $W_{\rm p}$ are collected under the assumption of $S_{\rm n} = 0$. A similar situation occurs under irradiation for $\Phi < \Phi_{\rm crit}$, as long as the former relationship between $L_{\rm n}$ and $W_{\rm p}$ holds true. This leads to the first degradation stage, where $L_{\rm n}$ degrades following Eq. 2.31 but no $J_{\rm SC}$ degradation is observed. As $\Phi > \Phi_{\rm crit}$ and $L_{\rm n}(\Phi) < W_{\rm p}$, carrier loss mechanism affects $J_{\rm base}$ and thus $J_{\rm SC}$, marking the onset of the second degradation stage.

2.4.3 Open-circuit voltage

The open-circuit voltage $V_{\rm OC}$ is a consequence of the band bending due to photo-generated carriers collected but not extracted from the solar cell. Under the assumption that $J_{\rm SC}$ is voltage-independent, $V_{\rm OC}$ is calculate imposing $J_{\rm tot} = J_{\rm SC}$ - $J_{\rm dark} = 0$, where $J_{\rm tot}$ is the total current extracted from the cell. If $J_{\rm dark}$ in Eq. 2.33 is dominated solely by one contribution denoted as $J_{\rm 0x}$, $V_{\rm OC}$ is determined as:

$$V_{\rm OC} = x\,\frac{kT}{q}\log\left(\frac{J_{\rm SC}}{J_{\rm 0x}}\right), \tag{2.49}$$

where x is 1 or 2 according to which $J_{\rm 0x}$ contribution prevails. It is then possible to write the $V_{\rm OC}$ dependence in a compact form:

$$\begin{aligned} V_{\rm OC}(\Phi) &= x\frac{kT}{q}\log\left[\frac{J_{\rm SC}(0) - C\log\left(1+\dfrac{\Phi}{\Phi_{\rm crit}}\right)}{\left(J_{\rm 0,x}(0) + k_\tau\tau(0)\Phi\right)^{x/2}}\right] \\ &\approx V_{\rm OC}(0) - \frac{x^2}{2}\frac{kT}{q}\log\left(1 + k_\tau\tau(0)\,\Phi\right). \end{aligned} \tag{2.50}$$

In Eq. 2.50, the logarithmic Φ-dependence of $J_{\rm SC}$ can be neglected. As for the $J_{\rm SC}$ case, we can rewrite Eq. 2.50 in remaining factor terms as:

$$\begin{aligned} \mathrm{RF}(V_{\rm OC}) &= 1 - C\log\left(1+\frac{\Phi}{\Phi_{\rm crit}}\right); \\ C &= \frac{1}{V_{\rm OC}(0)}\frac{x^2}{2}\frac{kT}{q}, \end{aligned} \tag{2.51}$$

with $\Phi_{\rm crit}^{-1} = k_\tau\tau(0)$ in this case.
In most cases, however, both current contribution show up in the $J_{\rm dark}$ of a GaAs solar cell at current regime where $V_{\rm OC}$ is determined. In order to determine the

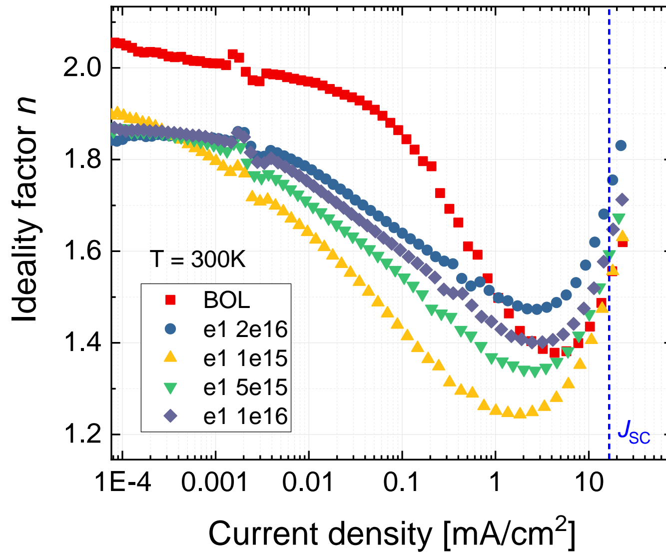

Figure 2.10 – Local ideality factor n as a function of the dark current density in (In)GaAs middle component cells at BOL and after irradiation with 1 MeV electrons at different fluence values.

major contribution of J_{dark} around V_{OC}, the voltage-dependent ideality factor n of the junction is monitored:

$$n(J_{\text{dark}}) = \left[\frac{kT}{q}\frac{\mathrm{d}\ln(J_{\text{dark}})}{\mathrm{d}V}\right]^{-1}. \tag{2.52}$$

For instance, the n-J_{dark} plot for the middle GaAs component cells at BOL and after 1 MeV electron irradiation at different Φ values is shown in Fig. 2.10. If J_{dark} is dominated by J_{01} then $n = 1$, whereas in the J_{02} case $n = 2$. In the current regime where $J_{\text{dark}} = J_{\text{SC}}$, n values range from 1.5 to 1.7 for the BOL as well as the irradiated cases. Moreover, the current at V_{OC} is already affected by the series resistance R_{s} effect, leading to the upward kink visible in Fig. 2.10. We shall deduce that the assumption of single dominant contribution in J_{dark} at V_{OC} is rather theoretical than representative of real cases. Most likely, both contribution are affecting the V_{OC} and the relative contribution varies with Φ due to the different Φ-dependencies of J_{01} and J_{02} as in Eq. 2.39 and 2.42. Therefore, Eq. 2.50 is not strictly suitable for space solar cells. Nevertheless, Eq. 2.50 is used to describe the experimental V_{OC} degradation data with a good margin of error.

Parameter	RCs
N_{t}	k_{t}
τ	$k_{\tau} \approx \sigma v_{\mathrm{th}} k_{\mathrm{t}}$
L	$k_{\mathrm{L}} = D^{-1} k_{\tau}$
J_{01}	$k_{\mathrm{J}_{01}} = \tau(0) k_{\tau}$
J_{02}	$k_{\mathrm{J}_{02}} = \tau_{\mathrm{SCR}}(0) k_{\tau_{\mathrm{SCR}}}$
J_{SC}	empirical $\Phi_{\mathrm{crit}}^{-1}$
V_{OC}	$\Phi_{\mathrm{crit}}^{-1} = \tau(0) k_{\tau}$

Table 2.1 – Summary table of the radiation damage coefficients RCs.

Chapter 3

Experimental Setups

3.1 Solar Cell structure

3.1.1 Triple-junction solar cell

The lattice-matched, space-grade triple-junction (3J) solar cell analyzed in this work targets a 30 % BOL efficiency. The representative cell architecture, sketched out in Fig. 3.1 (a), consists of three p-n shallow junctions where the p-type polarity is preferred for the thicker cell base (absorber), whereas thin n-type layers are used for the emitters. A review on the radiation response of different solar cell architectures is reported in [45, 50].

The cell is grown lattice-matched on a 4-inch, p-type Ge substrate via nucleation and following sequential growth of epitaxial layers via MOCVD.

The bottom Ge sub-cell is formed by As diffusion into the Ge substrate during the growth. The middle sub-cell consists of an $In_{0.01}Ga_{0.99}As$ junction featuring higher-band gap minority carrier barrier layers for back-surface field (BSF) and front-surface field (FSF). The thickness of the $In_{0.01}Ga_{0.99}As$ base is about 1.5 μm, smaller than the typical 3 μm design of a fully-absorbant GaAs cell. A distributed Bragg reflector at the back of the sub-cell reflects part of the utilizable photons, thus enhancing the effective absorption length in the cell and compensating the reduced current generation due to the thinner absorber. The thin base design, combined with the distributed Bragg reflector, increases the radiation-hardness of the sub-cell.

The top junction is formed by a lattice-matched $Ga_{0.5}In_{0.5}P$ junction with GaInP BSF and AlInP window layer. Each sub-cell is electrically connected in series via heavily-doped tunnel junctions ensuring low voltage losses and optical transparency.

An anti-reflective coating (ARC) is deposited on top of the AlInP window layer in order to reduce the reflectivity of the cell at the wavelengths of interest.

The wafers are processed in 2 cm $\times$ 2 cm solar cells. Ohmic contacts are realized with Au layers deposited on top of the cells via photolitography and vapour deposition techniques in a gridfinger pattern.

External connectors are applied via Ag strips welded at the Au/Ge top and bottom contacts. The overall thickness of the cell is determined mainly by the Ge substrate thickness, which ranges from 50 μm to 150 μm according to the device design.

The sub-cell band gaps of 0.66 eV, 1.41 eV and 1.89 eV are achieved with this solar

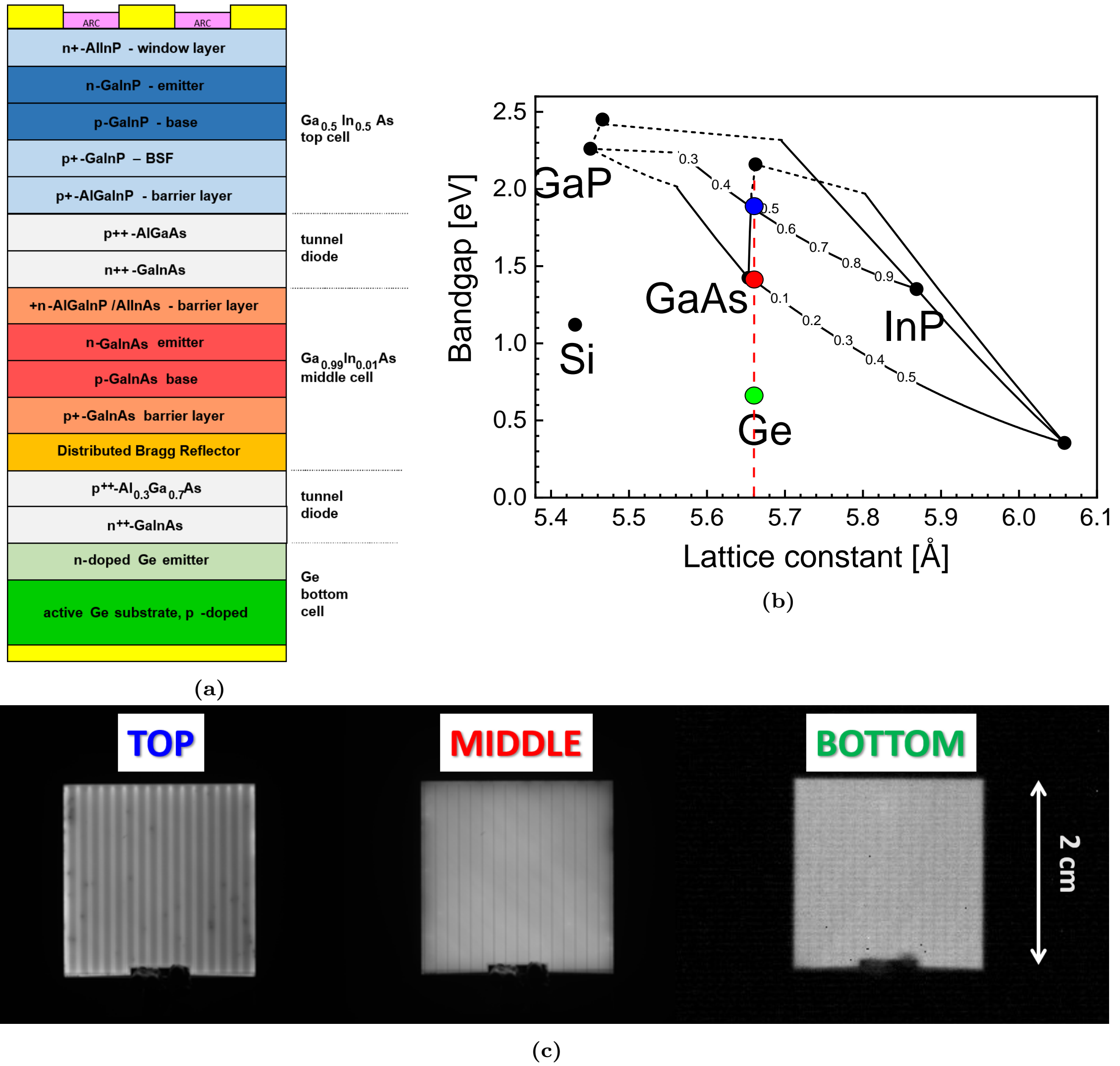

Figure 3.1 – (a) Schematic device structure, (b) lattice constant-band gap plot and (c) electroluminescence signal from each sub-cell of the reference 3J solar cell.

cell configuration, and the lattice constants are shown in Fig. 3.1 (b).
All epitaxially-grown sub-cells benefit of very high-quality opto-electronic materials. Moreover, the quality of the epi-layer is rather homogeneous throughout the area of the device. The spatially-resolved electroluminescence intensity is detected for each sub-cell with high dynamic resolution CCD cameras. The case for an exemplary 3J cell at BOL is shown in Fig. 3.1 (c). For top and middle sub-cell electroluminescence a 1024 x 1024 pixel Si sensor is used, whereas a 320 x 256 pixel HgCdTe is adopted for the Ge bottom cell.
The sub-cell band gaps are engineered to exploit efficiently the AM0 spectrum. In Fig. 3.2 (a), the EQE signal of a reference 3J solar cell is plotted after correction procedures illustrated in [51]. The AM0 spectrum is superimposed with a dashed line. The peak of the AM0 spectrum up to 700 nm is absorbed by the top cell. The absorption of the long wavelength (800-900 nm) in the middle sub-cell is enhanced by the Bragg reflector. The spectrum tail ($>$ 1000 nm) is absorbed by the Ge sub-cell. The top and middle sub-cells are very stable and reproducible from batch to batch.

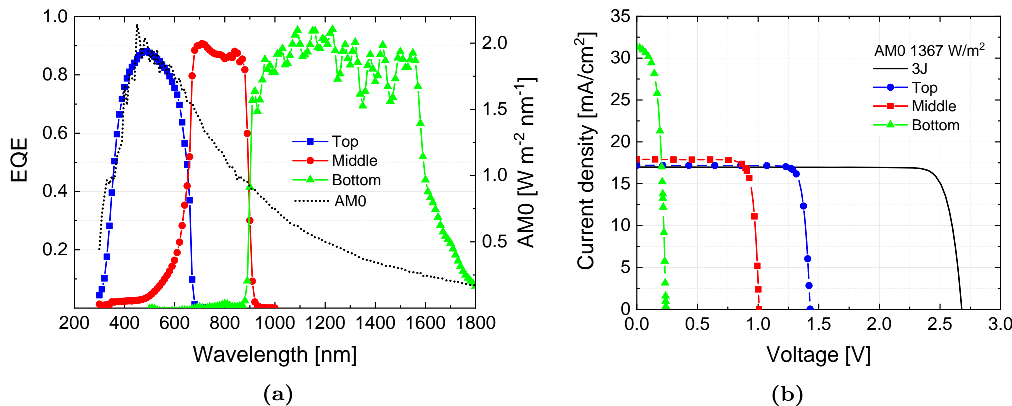

Figure 3.2 – (a) External quantum efficiency and (b) light J-V characteristics under AM0 spectrum of 3J solar cells and individual sub-cells.

Typical BOL photo-current average values of $17.14\,\mathrm{mA/cm^2}$ and $17.82\,\mathrm{mA/cm^2}$ are achieved for the top and middle cell, respectively. The bottom sub-cell electrical and optical properties, on the other hand, vary strongly with the production batch, as they are very sensitive to the wafer growth conditions and to the temperature variations during the MOCVD growth of the entire cell. It results that the BOL photo-current varies significantly from cell to cell. For our samples, a variation in a range between $28.86\,\mathrm{mA/cm^2}$ and $35\,\mathrm{mA/cm^2}$ is observed. As the bottom current density levels are higher than the ones in the middle and top sub-cells, the Ge bottom cell is never limiting the current of the whole 3J cell at BOL conditions. Therefore, the uncontrolled current of the bottom cell does not affect the performance of the overall 3J cell.

3.1.2 Component cells

The component cells, also referred to as iso-type cells in the literature, are a set of solar cell representative of individual sub-cells of a multi-junction solar cell architecture. In our study, the set of component cells consists of a top, middle and bottom component cell. Each component cell is fully representative of the respective sub-cell in the 3J structure described in the previous section. The epitaxial growth of the component cells follows a similar procedure as of the 3J stack, although a p-n junction is only formed at the sub-cell of interest, whereas the remaining sub-cell layers are grown using the same doping type for absorber and emitter layers. The component cells allow the electrical characteristics of the single sub-cells to be probed, while the entire optical properties of the cell structure are similar to the original 3J cell. The set enables the complete electrical characterization of the single sub-cells of the 3J stack. The opto-electronic properties of the individual sub-cells can be probed as well, as the entire optical filtering system is similar to the original 3J structure. This is shown exemplary in Fig. 3.2 (b), where the individual sub-cell J-V curves under AM0 conditions are plotted for the BOL case. The J-V of the 3J cell is also plotted with a black line. It is worth noting here, that the J_{SC} of the top cell corresponds to the J_{SC} of the 3J cell, as the top cell is limiting the 3J current at BOL conditions.

3.1.3 Mesa-diodes

The mesa-diode structures are designed and fabricated at Fraunhofer ISE for defect analysis in GaAs. The devices are designed to exhibit an overall SCR capacitance in the measurable range of the DLTS setup described in Section 3.2. A strongly asymmetry in the layer doping levels is necessary for junction DLTS. Given the fixed material-specific parameters, the total capacitance is adjusted by reducing the mesa area of the device. The epi-layers to form the p-n junctions were grown on a suitable 4-inch GaAs substrate. Circular structures with steep edges, referred to as mesa-structures, were fabricated using photolithography and a wet chemical etching processes. Several mesa-structures are etched out of the same wafer, while the deep etch ensures that each p-n junctions is separated from the others. Metal contacts are deposited by metal evaporation on the back of the wafer and on the top of each mesa-diode. For the front contact, a more accurate photolithography process is required to ensure that the evaporated metals lie exactly on the mesa-structure and no short circuit at the edge of the device is produced. The mesa-diodes were processed in three different form factors, with total area ranging from $0.15\,\mathrm{mm}^2$ to $1.02\,\mathrm{mm}^2$. The largest device ensures a total capacitance value without external applied voltage already below the 20 nF instrument limit. A microscope image of the $1.02\,\mathrm{mm}^2$ mesa-diodes is shown in Fig. 3.3 (a). For the defect analysis in GaAs, the p^+-n and n^+-p GaAs mesa-diode structures illustrated in Fig. 3.3 (b) were used. The n^+-p diodes were grown on a p-type substrate and are representative of a standard shallow-junction GaAs solar cell. The p^+-n diodes, grown on an n-type substrate, featured an AlGaAs/GaInP double hetero-structure grown on top of the p^+-n GaAs junction. The double heterostructure was not designed to be part of this experiment and it does not influence the defect spectroscopy analysis.

3.2 Experimental techniques

3.2.1 Irradiation experiments

Accelerated degradation tests for a given solar cell technology under space radiation environment are performed by mono-energetic irradiation experiments. The scope of the experiments is to accumulate an amount of non-ionizing dose into the solar cell. According to the standard DDD method [17], only one energy is required for proton testing. In the case of electrons, on the other hand, the higher sensitivity to the material threshold energy for displacement implies a number of irradiation energies equal or higher than two.
A brief description of the irradiation facilities where samples from this dissertation were irradiated are laid down in the following sections. They are routinely used by the European Space Agency (ESA) for radiation testing and solar cell qualification for space.

Electron irradiation facility

The electron irradiation experiments are performed at two different facilities: the IRI electron accelerator at TU Delft and the Sirius facility at the Ecole polytech-

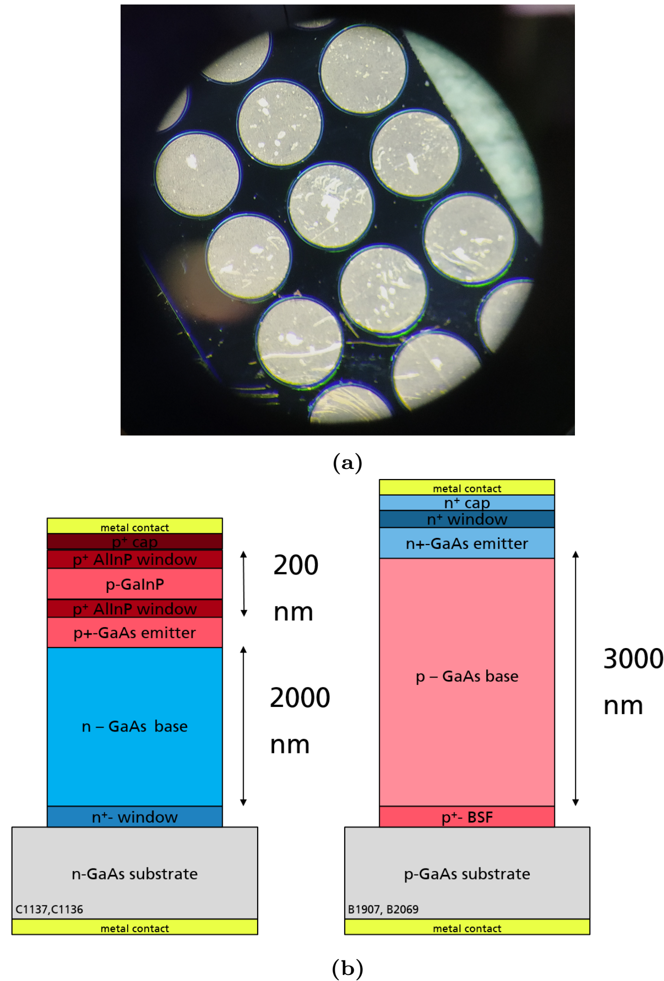

Figure 3.3 – (a) Microscope imaging of the 1.02 mm^2 mesa-diodes; on the top metal layer the scratches due to device contacting are visible. (b) Mesa-diode schematic structure grown at Fraunhofer ISE for defect analaysis in the n-type (left) and p-type (right) GaAs material.

nique in Paris. The IRI facility at TU Delft is a Van der Graaf accelerator which provides electron energies up to 3 MeV. The irradiation is performed under inert gas atmosphere. The fluence dosimetry is performed with a pre-calibration of the beam current based on radiachromic films. The Sirius irradiation facility is a pelletron accelerator which can be modulated to produce electron acceleration from 150 keV up to 2.5 MeV [52]. The fluence dosimetry is performed with a pre-calibration by measuring the current induced by the beam in a thick copper plate. The irradiation sample is kept in a cryostat at a vacuum level of 10^{-3} mbar. The vacuum line of the cryostat is disconnected from the vacuum line of the accelerator, which reaches a higher vacuum level of 10^{-7} mbar. The vacuum line separation, obtained via a thin window, cause electron scattering. This leads to the fact that the actual fluence at the sample surface, measured via the current induced in the thick copper plate, is always lower than the actual fluence in the accelerator line [53].

The irradiation flux in both facilities is set to $5{\times}10^{11}\,\mathrm{cm}^{-2}\mathrm{s}^{-1}$. Most of the electron degradation data available in the space solar cell community relies on irradiation experiments carried out at the TU Delft facility in the past decades.

Proton irradiation facility

The proton irradiation experiments are performed at the ion accelerator ARAMIS of the Centre de Sciences Nucleaires et de Sciences de la Matiere (CSNSM) of the University Paris-Sud. The accelerator is of a Van de Graaf type. The proton beam is generated in the accelerator by a Penning positive ions source generating H^+ ions. The irradiation is performed at a vacuum of 10^{-5} mbar, and the fluence dosimetry is performed with a pre-calibration by measuring the current induced on a metal plate between the cryostat and the beamline. In proton irradiation experiments it is important to limit the sample temperature increase during the irradiation. No temperature sensing and control on the sample is performed during the irradiation experiment. This poses a constraint on the maximum ion flux, set to a value of $10^9\,\mathrm{cm}^{-2}$ according to the relevant space standards [22].

3.2.2 Characterization methods

Current-Voltage characterization

Current density-voltage (J-V) characterization of the solar cells, both in dark and under illumination, were performed at Airbus Defence and Space. The light characteristics are measured using a Keithley 2420 source-meter and an AEG triple-source AM0 solar simulator, calibrated with Casolba 2005 standards. The illumination intensity was uniform over the active area of the solar cell measured. The measurement are performed while keeping the solar cells at a temperature of 300 K by using a water-cooled thermostat equipped with Pt100 temperature sensors. The same source-meter was used for the dark I-V characterization of the solar cells. In order to exclude series resistance effect at high-bias regime, the dark characteristics were also measured in a Suns-V_{OC} as well as pulsed fashion. In the Suns-V_{OC} case, three pulsed diode lasers are used as light source, with wavelength centered at 975 nm, 803 nm and 450 nm. The pulsed lasers are capable of inducing photo-current values in the solar cells up to 10 times the reference AM0 values. The J-V curves were also measured in a pulsed fashion for high current levels. In this case, a Keithley 2430C pulsed source-meter was used.

External quantum efficiency

The External Quantum Efficiency (EQE) characterization was performed at Airbus Defence and Space. A Spequest Quantum Efficiency set-up from RERA Solutions is used to measure the EQEs. The system uses both Xenon and Halogen light sources. The EQE data in multi-junction solar cells are corrected for measurement artifacts according to the procedure illustrated in [51].

Capacitance-Voltage characterization

The Capacitance-Voltage (C-V) characterization was performed at Airbus Defence and Space. An Hewlett Packard 4192A LF impedance analyzer is used, combined with a Keysight 16048A teas lead. The measurements were performed in parallel capacitance-conductance configuration, by using a fixed carrier frequency of 2 kHz

and varying the voltage applied to the cell. The characteristic were measured in dark condition and the solar cells were put on a thermostat with a temperature regulated at 300 K by means of Pt100 sensors.

Admittance characterization

The admittance characterization of the solar cells was performed at Airbus Defence and Space in a thermo-vacuum chamber setup. The vacuum system, consisting of a controller and a vacuum pump, is capable of reaching high-vacuum pressures down to 10^{-7} mbar. The solar cells are arranged on a thick Cu plate with a thin Ni coating, equipped with heaters and cooling pipes for liquid nitrogen flow. The measurement setup allows measurement in the temperature range $80\,\mathrm{K} < T < 370\,\mathrm{K}$. The solar cells are glued within dedicated slits with RTV silicone to the main plate. The RTV has good thermal conductivity and facilitates the removing of the solar cell after the experiments without significant cracking risk. A Pt100 temperature sensor is sandwiched between each solar cell and the copper plate in order to estimate the real temperature with a precision of about 0.5 K. The sample positioning is made in a way that solar cell connectors lay naturally over the holding rods, so that they can be clamped with the contacts without significant mechanical stress. Each contact of the solar cell is connected to the BNC connector terminal via 20 cm balanced cables. The vacuum chamber is equipped with 5 BNC terminal connector, in order to allow the measurement of five solar cells per temperature run. The setup is used also for temperature-depedent dark J-V characterization.
The admittance of the solar cell is measured with an auto-balancing bridge circuit implemented in the E4980a precision LCR meter from Keysight technologies, equipped with a Keysight 160248A teas lead. The frequency of the test signal varies in the range $20\,\mathrm{Hz} < f_{\mathrm{ac}} < 2\,\mathrm{MHz}$. The ac amplitude at the output terminal is controlled so that the actual ac voltage applied to the solar cell is kept constant over the whole frequency range. Data averaging improves significantly the signal-to-noise ratio of the admittance measurements, especially in the low-frequency range. The bias voltage is fixed at 0 V. The accuracy of the capacitance measurements over the specific range was better than 20 pF.

Deep-level transient spectroscopy

The deep-level transient spectroscopy (DLTS) characterization of mesa-diodes was performed with a modified SULA conventional DLTS system at the Fraunhofer ISE. The setup is composed of a cryostat with a sample holder equipped with thermal heaters and liquid He compression system, allowing temperatures between $20\,\mathrm{K} < T < 400\,\mathrm{K}$. The temperature control regulator is realized with a LakeShore 331 Temperature Controller equipped with two temperature sensors placed in the proximity of the sample holder. Measurements are performed under high vacuum condition of about 10^{-7} mbar. The pulse generator provides the 1 MHz test signal for the background capacitance measurements C_{SCR} as well as repetitive pulses for the transient measurements. The capacitance meter from SULA technologies uses a self-balancing bridge circuit to detect fast capacitance transient, and it can also be used for static C-V measurements. The range can be set over five different scales to

improve the signal-to-noise (SNR) ratio. The maximum capacitance value measurable with this instrument is 20 nF, thus posing a constraint on the maximum size of the sample suitable for DLTS. In order for the self-balancing bridge circuit to operate, the current through the device during the measurement should not exceed the value of 100 μA, according to the instrument specifications. Every examined device is checked beforehand for leakage current exceeding this limitation. The capacitance value is amplified with a gain factor adjustable according to the specific sample. Several pulses are applied with adjustable pulse time t_p and emission time t_e. A National Instrument digital acquisition card (DAQ) is used to record all the transients, which are then averaged to improve the SNR ratio. The transient data are filtered and correlated numerically with the double boxcar method [54] by using variable sampling times t_1 and t_2 while keeping constant the ratio t_1 / t_2. In this way, the DLTS spectra at several rate windows $t_\mathrm{w}^{-1} = (t_2 - t_1)^{-1}$ can be achieved with a single temperature scan.
The transient averaging, as well as the correlation analysis, is performed with the LDLTS software developed at Fraunhofer ISE.

3.2.3 Defect spectroscopy methods

Admittance Spectroscopy

Admittance spectroscopy (AS) is a steady-state capacitance spectroscopy method adopted for the characterization of deep levels in semiconductors. Pioneered by Walter *et al.* in [55], the method allows the electrical characterization of majority-carrier traps in a semiconductor to be performed by analyzing the temperature and frequency-dependent admittance of a p-n junction. The AS analysis has been integrated in capacitance simulation software such as SCAPS [56,57] and it is widely adopted in a wide range of semiconductor materials [58,59].
Let us assume a discrete, deep level, homogeneously distributed in the p-layer of a $\mathrm{n^+}$-p GaAs junction with a concentration N_t, acting as an hole trap. In order to be defined as a deep level in p-type material, the defect shall have an associated energy level $E_\mathrm{t} > E_{\mathrm{F_p}}$, where $E_{\mathrm{F_p}}$ denotes the Fermi level in the p-type neutral region. Let us assume that the trap is an acceptor-like level [0/-], i.e., its charge state is negative when emptied of a hole, whereas neutrum when filled with a hole. The contribution of the trap to the depletion layer capacitance C_SCR under the stimulus of an external ac bias $\delta v = v_\mathrm{ac} \exp(2\pi f t)$ with amplitude v_ac and frequency f is modeled using the analytical approach described by Blood and Orton in [60]. The defect level is exposed to a hole flux $p \cdot v_\mathrm{th}$ which depends on the position of the Fermi level E_F. Assuming a negligible barrier lowering in the SCR due to the junction electric field (Poole-Frenkel effect), the hole capture rate c_p and the emission rate e_p per unoccupied state are governed by the following relationships at thermal equilibrium:

$$
\begin{aligned}
c_\mathrm{p} &= \sigma_\mathrm{p} v_\mathrm{th} p = \sigma_\mathrm{p} v_\mathrm{th} \cdot N_\mathrm{V} \exp\left(-\frac{E_\mathrm{F} - E_\mathrm{V}}{kT}\right); \\
e_\mathrm{p} &= \frac{g_0}{g_1} c_\mathrm{p} \exp\left(\frac{E_\mathrm{F} - E_\mathrm{t}}{kT}\right) = \frac{g_0}{g_1} \sigma_\mathrm{p} v_\mathrm{th} N_\mathrm{V} \exp\left(-\frac{E_\mathrm{t} - E_\mathrm{V}}{kT}\right).
\end{aligned}
\tag{3.1}
$$

N_V is the effective density of states in the valence band, whereas g_1 and g_0 are the degeneracy factors when the state is empty or occupied by a hole, respectively. In the first half of the δv positive cycle, the Fermi level modulation δE_F in the SCR leads to a trap filling process with rate c_p and a modulation of the defect charge state per unit area δq_t. In the second half of the positive cycle, the filled traps are emptied by hole emissions with rate e_p. The same applies to the negative ac cycle. If δq_a denotes the charge variation due to the ionized acceptors N_a at the edge of the depleted region, the current oscillation per unit area in response to the applied ac bias is $\delta i = \mathrm{d}(\delta q_\mathrm{a} + \delta q_\mathrm{t})/\mathrm{d}t$.

The charge modulation δq_t responds directly to the driving bias δv, provided that

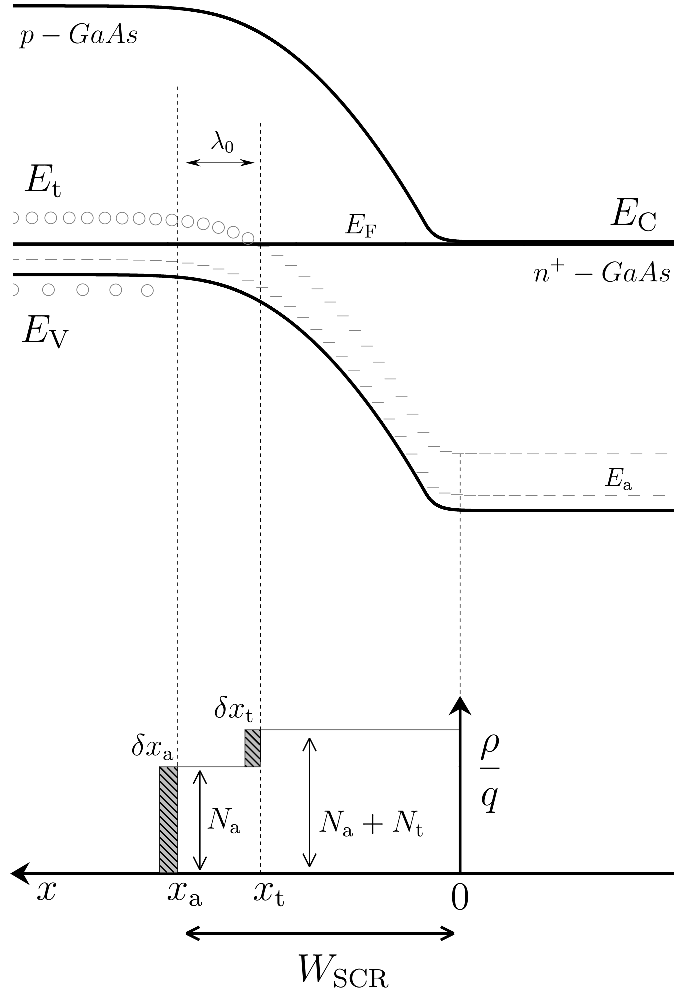

Figure 3.4 – Band diagram and charge distribution ρ/q in a n$^+$-p GaAs junction with a deep level located at $E_\mathrm{t} = 0.3\,\mathrm{eV}$ above E_V. The symbol "o" indicates the state filled with an hole, whereas the symbol "-" indicates a state emptied of an hole.

.

$f \ll e_\mathrm{p}/\pi$. In this low frequency regime, the charge contribution in the depletion capacitance is due to both N_a and N_t: $C_\mathrm{LF} = \epsilon/x_\mathrm{a,t} = C_\mathrm{SCR} + \Delta C$, where

$$x_\mathrm{a,t} = \frac{N_\mathrm{a}}{N_\mathrm{a}+N_\mathrm{t}} x_\mathrm{a} + \frac{N_\mathrm{t}}{N_\mathrm{a}+N_\mathrm{t}} x_\mathrm{t}\,. \tag{3.2}$$

x_a is the region where the acceptor atoms contribute in the capacitance, i.e., the whole SCR width W_{SCR}, whereas x_t is the portion of the SCR where N_t atoms are ionized. The portion of the SCR where only the acceptor atoms contribute in the capacitance is denoted as $\lambda_0 = x_a - x_t$, and it is computed as:

$$\lambda_0 = \sqrt{\frac{2\epsilon_0\epsilon_{rel}(E_t - E_{F_p})}{qN_a}}, \tag{3.3}$$

where ϵ_0 is the permittivity of vacuum and ϵ_{rel} is the material dielectric constant. The schematic is sketched out in Fig. 3.4 for the case of a hole trap located 0.3 eV above E_V. At the position $x = x_t$, $E_t = E_F$. By making use of Poisson's equation in the SCR, the capacitance contribution ΔC associated with the deep level is evaluated as:

$$\frac{\Delta C}{C_{SCR}} = \frac{N_t}{N_a}\left(\frac{1 - \frac{x_t}{W_{SCR}}}{1 + \frac{N_t x_t}{N_a W_{SCR}}}\right), \tag{3.4}$$

For $N_t \ll N_a$ Eq. 3.4 can be further simplified to

$$\frac{\Delta C}{C_{SCR}} = \frac{N_t}{N_a}\frac{\lambda_0}{W_{SCR}} = \frac{N_t}{N_a} \cdot \sqrt{\frac{E_t - E_{F_p}}{q\,V_{bi}}}, \tag{3.5}$$

where V_{bi} is the junction built-in voltage. At higher frequencies the trap cannot emit holes during the emitting cycle since $f \gg e_p/\pi$, therefore $\delta q_t = 0$ and $C_{HF} = C_{SCR} = \epsilon/W_{SCR}$ only due to N_a, with $W_{SCR} = x_a$. A frequency dependent expression for the depletion capacitance per unit area is obtained [60] from the complex part of $(2\pi f)^{-1} \cdot \delta i/\delta v$:

$$C(f) = C_{SCR} + \frac{\Delta C}{1 + (f/f_t)^2}. \tag{3.6}$$

Its derivation considers the change in majority carrier concentration in the depletion region based on the combined response of the shallow acceptors as well as the trap to the applied bias. The occupation probability of the trap is calculated with the help of c_p and e_p according to Eq. 3.1. The characteristic frequency f_t defines the transition between the two states of the trap behavior and is derived as

$$f_t = \frac{e_p}{\pi} \cdot \left(1 + \frac{x_t N_t}{W_{SCR} N_a}\right), \tag{3.7}$$

The term in the brackets of Eq. 3.7 expresses the coupling between the response of the deep level and the shallow acceptors.
The C-f characteristic exhibits a step-like behavior centered at $f = f_t(T)$ according to Eq. 3.6. At any given temperature, f_t is the frequency point with maximum derivative and is easily identified in a measured spectrum as the peak of the functional -$f\mathrm{d}C/\mathrm{d}f$. The depletion capacitance C_{SCR} is the value measured when ideally no deep level contributes and no carrier freeze-out occurs, i.e. $f \gg \max[e_p]$ and $f \ll \tau_\epsilon^{-1}$, with τ_ϵ denoting the dielectric relaxation time of the dopant atoms in GaAs.

In the real case of n deep levels characterized by a continuous distribution of available states in the band gap centered around the energy value E_{t_0}, the term N_t in Eq. 3.5 is replaced by the total density of states $N_T(E)$. For each defect level, a Gaussian-shaped distribution is considered, characterized by a density function:

$$N_T(E) = \frac{N_t}{\lambda\sqrt{2\pi}} \exp\left[-\frac{1}{2}\left(\frac{E - E_{t_0}}{\lambda}\right)^2\right], \tag{3.8}$$

where N_t is the total concentration and λ is the distribution width defining the localization of the electrons in the level. The total capacitance is thus obtained by integrating over all energies E in the band gap. If all energy levels are not used in absolute terms, but referenced to the valence band according to $E' = E - E_V$, the following expression is derived:

$$C = C_{SCR} + \sum_{k=1}^{n} \frac{C_{SCR}}{\lambda_k\sqrt{2\pi \cdot q V_{bi}}} \frac{N_{t,k}}{N_a} \times \\ \times \int_{E'_{F_p}}^{E'_{F_p}+qV_{bi}} \frac{\sqrt{E' - E'_{F_p}} \exp\left[-\frac{1}{2}\left(\frac{E'-E'_{t_0,k}}{\lambda_k}\right)^2\right]}{1 + \left\{\frac{\pi f \exp\left[E'/(kT)\right]}{\sigma_{p,k} v_{th} N_V}\right\}^2} dE'. \tag{3.9}$$

The value E'_{F_p} is obtained as $E'_{F_p} = E'_i - kT \cdot \ln(N_a/n_i)$, where E'_i and n_i are the intrinsic Fermi level position and the intrinsic carrier concentration, respectively. Deep levels outside the integral boundaries in Eq. 3.9 do not cross E_F in the p-side SCR, and thus cannot contribute to the capacitance.
The advantage of the AS method lies in the simple measurement setup to acquire C-f-T data. By employing standard LCR meters available on the market, detection level of $N_t/N_{a,d} = 10^{-3}$ can be easily achieved. In addition, the constraints on the maximum device capacitance are relaxed. The method is thus suitable for the analysis on actual solar cells, e.g., 2 cm× 2 cm GaAs-based component cells.

Deep-Level Transient Spectroscopy

The deep level transient spectroscopy (DLTS) is a transient capacitance spectroscopy method adapted to the characterization of deep levels in semiconductors. Pioneered by Lang *et al.*, [54], the technique aims to study the electrical characteristics of majority- and minority-carrier traps in semiconductors by analyzing the transient capacitance signal in response to bias pulses. Originally developed to study defects in a single-polarity material by means of a Schottky junction, the method is also suitable to probe the low-doped material in an asymmetric p-n junction.
Let us consider an abrupt asymmetric n^+-p junction in a negative reverse bias condition V_R at $t < 0$, with a deep level located at E_t above E_V with concentration N_t. Let us assume that the trap is an acceptor-like level [0/-], i.e., its charge state is negative when emptied of a hole, whereas neutral when filled with a hole. Neglecting the portion of the depleted region in the n^+ material, the SCR width extends in the p-type region from the semiconductor junction $x = 0$ till x_R. The situation is sketched out in Fig. 3.5. The deep level crosses the Fermi level E_F in the p-type

material at a specific location (identified by x_t in Fig. 3.4). The crossing defines the portion $\lambda_0 = x_R - x_t$ shown in Fig. 3.5. In the region of the SCR from 0 to $x_R - \lambda_0$, the traps are emptied of holes and the net charge distribution equals $N_a + N_t$; in the portion between $x_R - \lambda_0$ and x_R the level is filled with holes and the net charge distribution equals N_a. The charge configuration representative of the situation at $t < 0$ is not the one depicted in Fig. 3.5. The situation is more similar to the one sketched out in Fig. 3.4. In summary, at $t < 0$ we have:

$$\begin{aligned} \frac{\rho}{q} &= N_a \;\; \text{for} \;\; x_R < x < x_R - \lambda_0; \\ \frac{\rho}{q} &= N_a + N_t \;\; \text{for} \;\; x_R - \lambda_0 < x < 0; \end{aligned} \tag{3.10}$$

If the junction is perturbed at $t = 0$ with a pulse of duration t_p and amplitude V_F with $V_R < V_F \leq 0$, the SCR is reduced from x_R to x_F. During the pulse, the trap is then exposed to a hole flux $p \cdot v_{th}$, triggering capture processes with capture rate c_p per unoccupied state, as in Eq. 3.1. As a result, the traps in the region x_R-$\lambda_0 < x < x_F$- λ_0 (which were emptied at $t < 0$) are now filled with holes. If t_p is long enough with respect to c_p^{-1}, we can assume that all traps N_t in this SCR portion are filled. Therefore, at $0 < t < t_P$ we have:

$$\begin{aligned} \frac{\rho}{q} &= N_a \;\; \text{for} \;\; x_R < x < x_F - \lambda_0; \\ \frac{\rho}{q} &= N_a + N_t \;\; \text{for} \;\; x_F - \lambda_0 < x < 0; \end{aligned} \tag{3.11}$$

At $t = t_P$, the junction bias is brought back to the original V_R condition. The trapped holes in the region x_R-$\lambda_0 < x < x_F$- λ_0 are thermally emitted to the valence band with

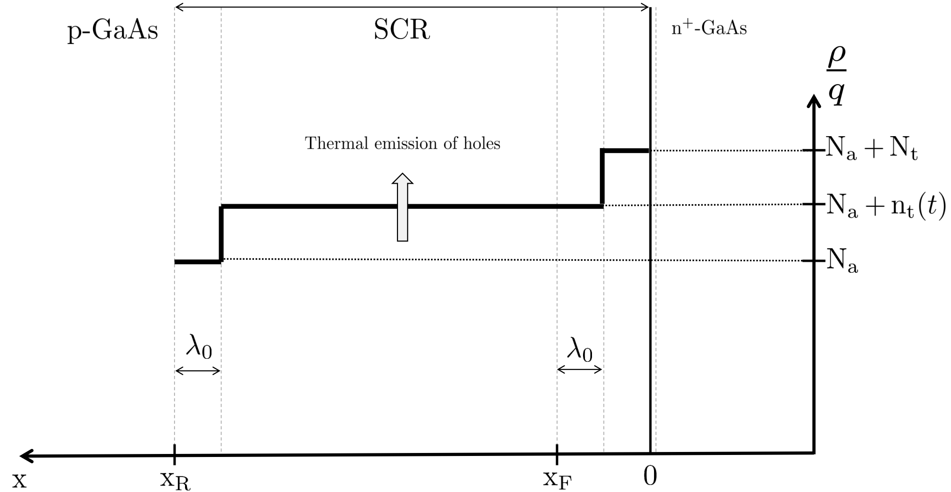

Figure 3.5 – Charge distribution ρ/q during a DLTS transient in an n$^+$-p GaAs junction. The holes – captured at the defect level during the filling pulse – are thermally emitted during the transient as the junction is reverse biased, thus producing a charge variation. The figure is a modified version taken from [60]

an emission rate defined by the trap properties according to Eq. 3.1. The situation of the net charge is depicted in Fig. 3.5, where the emission process is highlighted by the arrow. The emission process can be described by the hole occupation function of the trap level $n_\mathrm{t}(t)$:

$$n_\mathrm{t}(t) = N_\mathrm{t} \cdot \exp\left(-e_\mathrm{p} t\right). \tag{3.12}$$

Therefore, at $t > t_\mathrm{P}$ the net charge distribution is given by:

$$\begin{aligned}
\frac{\rho}{q} &= N_\mathrm{a} \quad \text{for} \quad x_\mathrm{R} < x < x_\mathrm{R} - \lambda_0;\\
\frac{\rho}{q} &= N_\mathrm{a} + n_\mathrm{t}(t) \quad \text{for} \quad x_\mathrm{R} - \lambda_0 < x < x_\mathrm{F} - \lambda_0;\\
\frac{\rho}{q} &= N_\mathrm{a} + N_\mathrm{t} \quad \text{for} \quad x_\mathrm{F} - \lambda_0 < x < 0;
\end{aligned} \tag{3.13}$$

The capacitance C measured at $t = t_\mathrm{p}^+$ is thus lower than the value C_SCR measured at $t < 0$ due to the contribution of the charge accumulated in the traps. This contribution is quantified by the term $\Delta C_0 = \Delta C(t_\mathrm{p}^+)$. Since the trapped carriers are majority carriers, the sign of ΔC_0 is negative. The charge transient described by Eq. 3.12 leads to a likewise capacitance transient $\Delta C(t)$, which is monitored by means of a fast capacitance meter operating with a high-frequency carrier. A detailed expression for $\Delta C(t)$ is given in [60] by employing the rectangular transient charge model to relate the trapped charge transient $\rho/q(x,t)$ and the change in x_R and V. In the dilute limit $N_\mathrm{t} \ll N_\mathrm{a}$, the capacitance transient assumes the form of an exponential decay:

$$\Delta C(t) = \Delta C_0 \exp\left[-t/\tau_\mathrm{e}(T)\right], \tag{3.14}$$

where the emission time constant $\tau_\mathrm{e} = e_\mathrm{p}^{-1}$ is temperature-dependent according to Eq. 3.1.
The double boxcar method, proposed first by Lang in [54], is an useful tool to determine the defect properties from capacitance transients acquired at different device temperature T. The method requires the sampling of the capacitance transients at two instants t_1 and t_2, defining the window time $t_\mathrm{w} = t_2 - t_1$. Denoted g the calibration factor which accounts for the gain of the measurement system, the DLTS signal S is defined as the difference between the capacitance values sampled across t_w, which can be written with the help of Eq. 3.14:

$$S(T) = g\Delta C_0[\exp\left(-t_1/\tau_\mathrm{e}(T)\right) - \exp\left(-t_2/\tau_\mathrm{e}(T)\right)]. \tag{3.15}$$

The function S-T has a peak of amplitude S_pk. The condition for this peak are found by differentiating S with respect to τ_e:

$$\tau_\mathrm{e}(T) = \tau_\mathrm{e,ref} = t_\mathrm{w} \ln\left(\frac{t_2}{t_1}\right). \tag{3.16}$$

By substituting Eq. 3.16 in Eq. 3.15, it follows that the peak value S_pk is only dependent on ΔC_0 and the ratio t_1/t_2. Therefore, if $\tau_\mathrm{e,ref}$ is changed by changing t_1 and t_2 such that their ratio remains constant, the relation between S_pk and ΔC_0

remains independent on the choice of $\tau_{\mathrm{e,ref}}$. In this way, the emission rate $e_{\mathrm{p}}(T)$ can be determined by the peak position T_{pk}, and the Arrhenius plot e_{p}/T^2 yields the apparent activation energy $E_{\mathrm{t}}' = E_{\mathrm{t}} - E_{\mathrm{V}}$ and capture cross-section σ_{p}:

$$\frac{e_{\mathrm{p}}}{T^2} = \nu \exp - \frac{E_{\mathrm{t}}'}{kT}, \tag{3.17}$$

where ν is the pre-exponential factor containing σ_{p} according to Eq. 3.1.
The peak height S_{pk} is extracted directly from the measured spectra, from which ΔC_0 can be inferred taking into account that the ratio $\Delta C_0/S_{\mathrm{pk}}$ is constant and for our setup equals 3.1. The trap concentration can be then evaluated with [60]:

$$\frac{\Delta C_0}{C_{\mathrm{SCR}}} = \frac{N_{\mathrm{t}}}{2N_{\mathrm{a}}} \left[\left(1 - \frac{\lambda_0}{x_{\mathrm{R}}}\right)^2 - \left(1 - \frac{\lambda_0}{x_{\mathrm{P}}}\right)^2 \right], \tag{3.18}$$

with λ_0 obtained from Eq.3.3. Equation 3.14 and 3.18 relate the capacitance transient to the deep level parameters.
If a forward pulsed voltage is applied to the junction, injection of minority carriers into the SCR occurs. Minority carrier traps can thus be detected in the DLTS signal as well. The minority carrier capture and emission processes from the level to the conduction band E_{C} is described the same way as in the majority carrier case, with the only exception that the capacitance contribution ΔC_0 is positive.
The relation between ΔC_0 and S_{pk} remains constant under the assumption that the capacitance transient has a mono-exponential decay described by Eq. 3.14. This is a typical response of simple point-defects in a periodic lattice structure, whose associated density of states within the band gap can be discretized in one single energy level. If the capacitance transient is non-exponential, the measured DLTS spectrum as in Eq. 3.15 is distorted and the peak assumes a broad feature. Several causes may be responsible for a non-exponential transient. Among the most relevant for deep levels in III-V:

- If the carrier emission involves phonon-assisted tunneling, then the emission rate depends upon the the different electric field at the different position x within the SCR; this effect can be usually identified by probing the emission rates at different locations in the SCR where the trap is exposed to different electric fields.

- The emission rate at a particular trap site depends upon the local environment in the crystal; in an alloy semiconductor with three or more atomic species, there is a significant statistical variation in the nearest neighbor species which leads to a distribution of values of e_{p} through the sample. Broadening of DLTS spectra has been observed to increase with increasing alloy composition and this has been ascribed to such alloy fluctuations [61].

- A similar situation may be caused by highly damage regions where the damage is clustered; the internal electric fields at defect cluster sites may also play a significant role in the broadened spectrum.

The broad features of the peaks resulting from non-exponential transient can be studied as a capacitance transient due to a continuous distribution of deep levels within the band gap. Equation 3.14 is then modified in [62]:

$$\Delta C(t) = \int_E g(E)\Delta C_0 \exp\left(-t/\tau_\mathrm{e}\right)\mathrm{d}E\,, \tag{3.19}$$

where the transient weighting function $g(E)$, assuming a deep level described by a Gaussian density of states function around E_{t_0}, can be written as:

$$g(E) = \frac{1}{\lambda\sqrt{2\pi}} \exp\left[-\frac{1}{2}\left(\frac{E - E_{\mathrm{t}_0}}{\lambda}\right)^2\right]. \tag{3.20}$$

The magnitude of the parameter λ in Equation 3.20, referred to as energetic disorder of the defect, is a measure of the alloy broadening of the impurity level.
A final remark is necessary on the type of devices required for DLTS measurements. The high sensitivity needed in the fast-rate capacitance measurements required in DLTS imposes a technological constraint on the maximum measurable capacitance value, which thus limits the applicability of the method to dedicated structures exhibiting capacitance values below the measurable range. In our setup, devices with a capacitance up to 20 nF can be measured. The method is thus not suitable for the 2 cm × 2 cm component cells. Therefore, we use DLTS on dedicated mesa-etched diode structures. The upside of the DLTS technique is the superior sensitivity to low defect concentration, reaching detection factor as low as $N_\mathrm{t}/N_\mathrm{a,d} = 10^{-5}$.

Interpretation of the Arrhenius plot and Meyer-Neldel rule

Both AS and DLTS allows the majority carrier trap E_t and $\sigma_\mathrm{p,n}$ to be determined from the assessment of the trap emission rate $e_\mathrm{p,n}$ and the linear fit of the Arrhenius plot with Eq. 3.1. The same defect sampled in different devices can exhibit a variation of the emission rate which leads to a scattering of the apparent E_t' and $\sigma_\mathrm{p,n}$ data. The data scattering can be partially explained by the influence of the electric field on the trap emission rate, as explained in Section 7.4.4. Another reason for the data scattering is the so-called Meyer-Neldel rule (MNR) [63], an empirical relationship that is observed in a wide range of thermally-activated processes. The MNR is recurring in semiconductor traps [64]. Evidences of MNR have been observed in Cu(In,Ga)Se_2 and InGaAsN alloys [65]. The most physically satisfying explanation is based on the realization that there is a considerable contribution of entropy change in the carrier emission process [66]. The concept of the change in entropy can be viewed as an alteration of the ionic potential when a hole moves from the trap to the valence band. Thermodynamically, the energy of deep states is better described by a Gibbs Free energy G_t rather than the "normal" energy E_t. For a hole trap, $E_\mathrm{t} - E_\mathrm{V} = \Delta G_\mathrm{t} = \Delta H_\mathrm{t} - T\Delta S_\mathrm{t}$ where ΔH_t and ΔS_t are the change in enthalpy and entropy, respectively, associated with the hole emission event. In defect electrical characterization, the term ΔS_t is usually neglected, so that $E_\mathrm{t} - E_\mathrm{V} \approx \Delta H_\mathrm{t} = E_\mathrm{t}'$. A more rigorous expression for Eq. 3.1 should include both effects. The MNR states that $\Delta S_\mathrm{t} = \Delta H/T_\mathrm{iso}$ where the constant T_iso is the termed isokinetik temperature.

By rewriting Eq. 3.1 for a trap obeying the MNR we obtain:

$$e_{\mathrm{p}} = \frac{g_0}{g_1}\sigma_{\mathrm{p}} v_{\mathrm{th}} N_{\mathrm{V}} \exp\left(\frac{E'_{\mathrm{t}}}{kT_{\mathrm{iso}}}\right) \exp\left(-\frac{E'_{\mathrm{t}}}{kT}\right) = \nu \exp\left(-\frac{E'_{\mathrm{t}}}{kT}\right) . \tag{3.21}$$

According to Eq. 3.21, the following relationship is found for $\ln(\nu)$ and ΔH:

$$\ln(\nu) = A + \frac{\Delta H}{kT_{\mathrm{iso}}}, \tag{3.22}$$

where A is a constant. By plotting the scattered data of E'_{t} and $\ln(\nu)$, a linear relationship is found with slope $(kT_{\mathrm{iso}})^{-1}$.
If a scattering of trap data does not satisfy the MNR rule, the trap properties are different and therefore it is likely that they belong to different structural defects. Therefore, the MNR empirical approach was proposed as a tool to identify trap signature from similar defects in compounds [67]. The method is, however, purely empirical, and an exhaustive physical explanation is still missing.
In this thesis, we use the MNR correlation to check for similarity in the trap signatures detected in $In_{0.01}Ga_{0.99}As$ component cells and GaAs mesa-diodes.

Chapter 4

Photovoltaic Parameter Degradation

The first and most direct approach in studying the displacement damage effects on solar cells is to look at the degradation of the macroscopic PV parameters. In solar array design, the degradation of the solar cell P_{MP} is the main focus, followed by J_{SC} and V_{OC}. As we are aiming to characterize the damage in III-V material at a deeper physical level, only the latter two parameters are investigated in detail, as P_{MP} is a direct consequence of J_{SC}, V_{OC} and the device structure. Space-grade 3J solar cells and related component cells described in Section 6.2 were irradiated with 1 MeV and 3 MeV electrons and 1 MeV and 2 MeV protons at different fluence values Φ. The cell parameters were extracted from the light J-V curves measured under AM0 spectrum at 300 K, as described in Section 6.2. The cells were measured three times: I) before irradiation; II) after irradiation; III) after irradiation and ECSS standard annealing. The ECSS standard annealing stage [22] comprises of

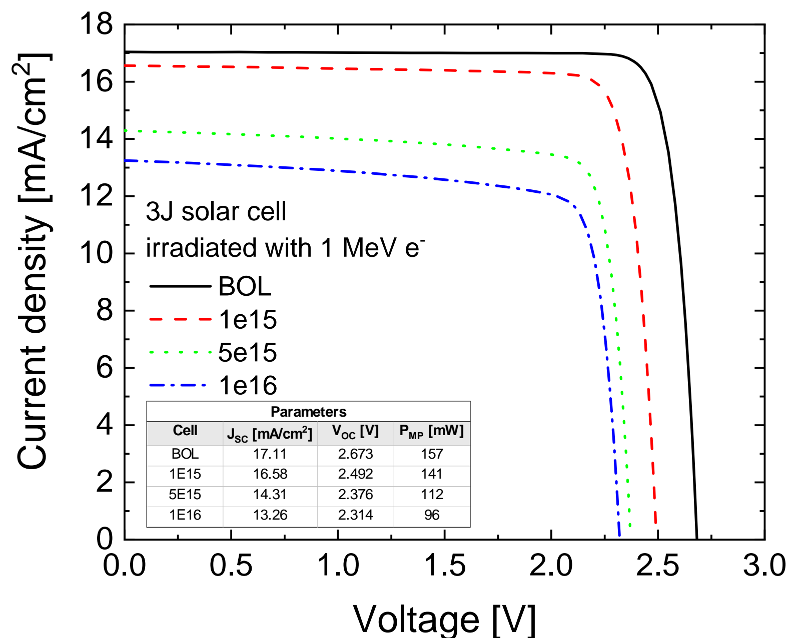

Figure 4.1 – Light J-V characteristics of 2 cm × 2 cm 3J solar cells at BOL and after 1 MeV electron irradiation with standardized ECSS annealing. The irradiation fluence values are reported in the legend in unit of cm^{-2}. The photovoltaic cell parameters are reported in the inset table.

two steps: I) 48h under AM0 condition at $T = 300\,\mathrm{K}$; II) 24h in dark conditions at $T = 333.15\,\mathrm{K}$. Comparing the values before (BA) and after (AA) the annealing stage facilitates the understanding of the photo-thermal process on the PV parameters. Representative light J-V curves for the 3J solar cell at BOL condition as well as after irradiation with 1 MeV electrons at different fluence values are depicted in Fig. 4.1.

4.1 Fitting of the remaining factors

The degradation analysis is performed by studying the dependencies of the parameter remaining factors (RF), as defined in Eq. 2.32, as a function of the DDD calculated with Eq. 2.22. Only top and middle component cells are analyzed, as the DDD analysis is not applicable to the bottom component cells for the reasons explained in Section 2.3.2. The fitting of the RF for J_{SC}, $\mathrm{RF}(J_{\mathrm{SC}})$, and V_{OC}, $\mathrm{RF}(V_{\mathrm{OC}})$, was performed with the equation:

$$\mathrm{RF} = 1 - C \log\left(1 + \frac{\mathrm{DDD}}{D_{\mathrm{crit}}}\right). \tag{4.1}$$

Eq. 4.1 is similar to Eq. 2.48 and 2.51, with Φ replaced by DDD and Φ_{crit} replaced by D_{crit}. The quality of each fit is quantified by the residual sum of squares (RSS):

$$\mathrm{RSS} = \sum_{\mathrm{i}=1}^{m} \left(\mathrm{RF_i} - \mathrm{RF_{i,fit}}\right)^2 \tag{4.2}$$

where m is the number of data points and $\mathrm{RF_{i,fit}}$ are the simulated degradation values with Eq. 4.1. The fitting routine of the degradation data of the 3J cell, as well as each component cell, is performed according to the procedure outlined in Section 2.3.1. In summary, first the $\mathrm{RF}(J_{\mathrm{SC}})$ data from electron-irradiated cells are fitted with Eq. 4.1 by varying the E_{d} values of the material atomic species. The NIEL calculated with the resulting values of E_{d} are then used to calculate the proton DDD. If a mismatch between the proton and electron degradation data is observed, a correction factor $\mathrm{R_{ep}}$ is calculated to account for the different effectiveness of electron and proton DDD.

4.2 $In_{0.01}Ga_{0.99}As$ middle component cell

The middle $In_{0.01}Ga_{0.99}As$ sub-cell is the most radiation sensitive sub-cell of the 3J stack and it becomes the current-limiting sub-cell for higher irradiation fluence Φ. The DDD analysis on this sub-cell is achieved by neglecting the 1% In concentration in the NIEL calculation. The NIEL for the GaAs component cell is thus calculated by considering a 1:1 composition of Ga and As. The NIEL fitting procedure is performed on the J_{SC} degradation data by varying Ga and As E_{d} from 10 eV up to 50 eV. For each E_{d} combination, the J_{SC} data are fitted against the DDD by using Eq. 4.1 . The best combinations of Ga and As E_{d} obtained from the J_{SC} fitting routine are plotted in the contour plot in Fig. 4.2 (a) for the BA case. From Fig. 4.2 (a) it is possible to evaluate the best combinations of E_{d} values leading

to the NIEL calculation providing the optimum RF(J_{SC}) fit. The minimum RSS values lie on a characteristic hyperbole. All the E_d pairs on this hyperbole leads to an adequate NIEL describing the electron-induced degradation in $In_{0.01}Ga_{0.99}As$ component cells. As Ga and As threshold energies are likely to be similar, we refer to the best solution as the NIEL calculated with $E_d = 21$ eV for both Ga and As atoms. In Fig. 4.2 (b) the same plot is reported for the AA case. A slight shift of the contour plot is observed, and the optimum E_d values becomes 20 eV. A variation of the E_d in the NIEL fitting routine indicates that the J_{SC} annealing is somewhat dependent on the energy of the electron irradiation. This difference is, however, negligible when comparing the calculated DDD. By using 21 eV, the J_{SC} remaining factors are plotted against the DDD in Fig. 4.3 (a).

The grey open symbols are the BA data measured after irradiation, whereas the coloured filled symbols are the AA data. The proton data matches well the electron degradation curve. This is representative of the fact that the radiation coefficient (RC) of J_{SC}, i.e., Φ_{crit}^{-1}, depends linearly on the NIEL in both the low-NIEL and high-NIEL range. It results that J_{SC} degradation is described by a pure function of the DDD only. An overall J_{SC} recovery is observed after the ECSS annealing stage, deduced from a D_{crit} increase of about 20%. This is representative of a slight recovery of the cell J_{SC} after the annealing stage. The amount of beneficial annealing for each irradiation case is better understood from the box-plot reported in Fig. 4.3 (b), where the relative changes of J_{SC} before and after annealing ($\Delta J_{SC}/J_{SC,(BA)}$) are reported for all fluence values. It should be noted that the fluence influences the amount of relative defect recovery via Eq. 2.29 and Eq. 2.2. Multiple defects undergo reordering processes and each of them has a different impact in determining J_{SC}. Therefore, a determination of the Φ-dependent relative J_{SC} recovery is not straightforward. From the analysis reported in Fig. 4.3 (c) it results that for all cases J_{SC} experiences

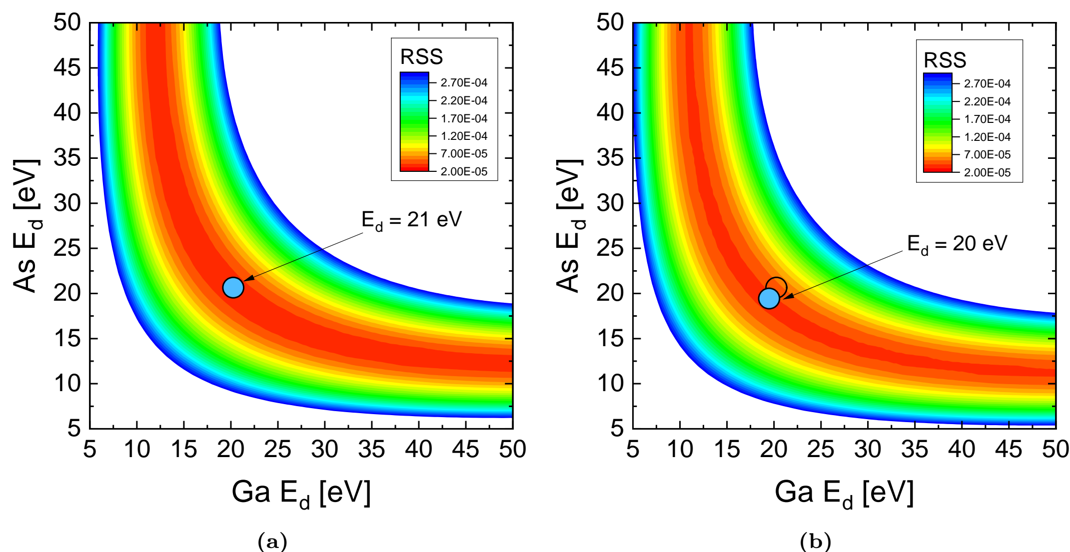

Figure 4.2 – Residual sum of squares (RSS) contour plot obtained by fitting of the J_{SC} electron degradation data in $In_{0.01}Ga_{0.99}As$ component cells as a function of the Ga and As threshold energies E_d. The plot in (a) shows the results for the cells measured before annealing (BA), whereas (b) shows the results for the cells after annealing (AA).

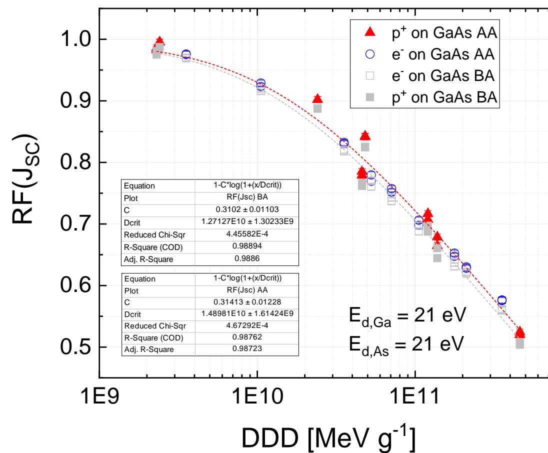

(a)

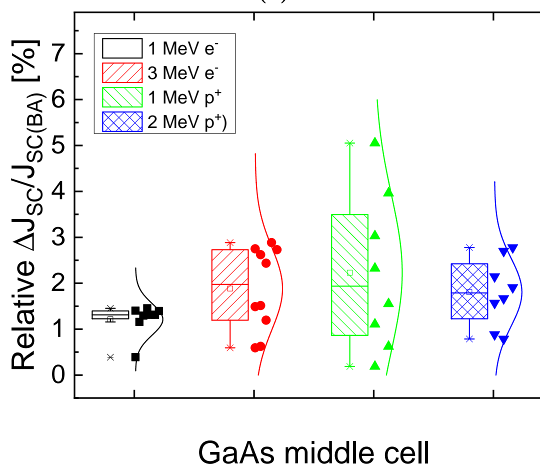

(b)

Figure 4.3 – (a) Remaining factors of the J_{SC} in $In_{0.01}Ga_{0.99}As$ component cells as a function of the DDD, calculated with $E_d = 21$ eV for Ga and As. (b) Relative change of the J_{SC} parameter after ECSS annealing.

a beneficial recovery effect, ranging for most of the cases from 1% to 3% of the vale measured after irradiation and regardless of the type and energy of the particle radiation induced damage.

A similar analysis is performed for the cell V_{OC}. The same NIEL with $E_d = 21$ eV is adopted. The V_{OC} remaining factors are plotted in Fig. 4.4 (a) for the BA and AA case. The experimental data are fitted separately for the electron and proton case with Eq. 2.51. A different degradation behavior is observed for the electron and proton cases. This is explained by the different C factor due to the different slopes of the V_{OC}-log(Φ) plot. From the theoretical derivation of Eq. 2.51 we shall conclude that a different C factor in the V_{OC} fitting can only be traced back to a different dominating recombination contribution J_{0x} in J_{dark}. If the proton dose is multiplied by a factor $R_{ep} = 2.5$, the proton data overlaps with the electron data. This is shown in Fig. 4.4 (b). The fitting of both set of data is performed with Eq. 2.51.

The V_{OC} recovery after the annealing effect is not as pronounced as for the J_{SC}. The relative parameter changes after annealing are reported in Fig. 4.4 (c). In the proton case, no effect is observed and the data are spread around 0. In the electron case,

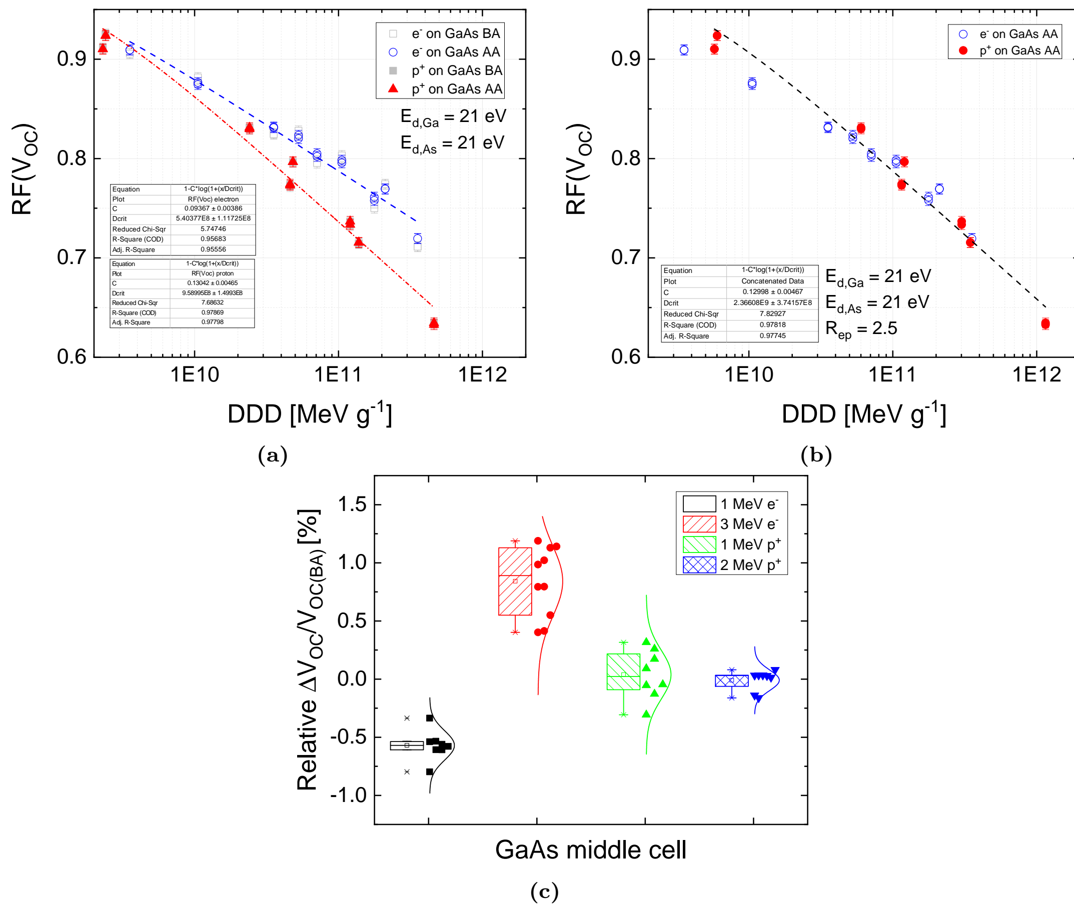

Figure 4.4 – (a) Remaining factors of the V_{OC} in $In_{0.01}Ga_{0.99}As$ component cells as a function of the DDD, calculated with $E_d = 21$ eV for Ga and As. The proton dose is corrected with the R_{ep} factor in (b). (c) Relative change of the V_{OC} parameter after ECSS annealing.

on the other hand, it is interesting how in the 1 MeV case the V_{OC} exhibits even an additional degradation following ECSS annealing, whereas for the 3 MeV case a recovery up to 1% occur. Despite the low absolute value, the energy-dependent V_{OC} recovery should be traced back to an alike energy-dependent annealing dynamics of some defects in the p-type GaAs material following electron irradiation. For proton irradiation, no absolute recovery of the V_{OC} is observed. The higher damaging effectiveness of protons is already observed in the BA case ($R_{ep} = 2.5$) and the annealing does not influence the R_{ep} value. Therefore, the physical reason for the proton dose correction is ascribed to a different damaging effectiveness of V_{OC}-affecting defects which are formed at 300 K and are rather stable at 333.15 K.

4.3 $Ga_{0.5}In_{0.5}P$ top component cell

The top $Ga_{0.5}In_{0.5}P$ sub-cell is the highest band gap sub-cell of the stack, and thus is responsible for the highest contribution to the 3J cell V_{OC}. The top cell is designed to be current limiting at BOL. The same analysis performed for the middle $In_{0.01}Ga_{0.99}As$ cell is performed for the top cell. The determination of the proper NIEL for the $Ga_{0.5}In_{0.5}P$ material is performed on the J_{SC} degradation data. In

contrast to $In_{0.01}Ga_{0.99}As$, all three atomic species should be taken into account for the proper NIEL determination. This complicates the representation with contour plots as done for $In_{0.01}Ga_{0.99}As$ sub-cells. Several combinations of (Ga, In, P) E_d leads to an optimum NIEL for the J_{SC} degradation. For instance, the best E_d combinations are found as the values that produce a J_{SC} fit result with $2.7{\cdot}10^{-5} < RSS < 3{\cdot}10^{-5}$. The E_d combinations are reported in the contour plot shown in Fig. 4.5. All combinations shown in Fig. 4.5 produce a similar NIEL curve in the electron energy range of interest. For sake of simplicity, we shall assume the combination (21, 21, 53) eV for the BA case and (21, 24, 72) eV for the AA case.

The resulting NIEL for the AA case is about 30% lower at 1 MeV electron as compared to the BA case. As the difference between the BA and AA NIEL in terms of RSS is negligible, we shall refer to the BA NIEL to consistently calculate the DDD in $Ga_{0.5}In_{0.5}P$ material.

The J_{SC} remaining factors and relative recovery after annealing are illustrated in Fig. 4.6 (a) and (b), respectively.

Also in the $Ga_{0.5}In_{0.5}P$ case, the proton data matches the electron data in both BA and AA cases, as observed in Fig. 4.6 (a). The J_{SC} degradation is thus described as a pure function of the DDD only. Moreover, a J_{SC} recovery is observed in all cases ranging from 0.5% to 3% as shown in Fig. 4.6 (b).

The V_{OC} remaining factors are plotted in Fig. 4.7 (a) without and (b) with application of the required R_{ep} factors. In the BA case, both proton and electron data collapse onto a single degradation curve and no R_{ep} correction is necessary as for the middle cell case. This is representative of similar V_{OC} damage introduced by both low-NIEL (electrons) and high-NIEL (protons) particles. The ECSS annealing leads to a V_{OC} recovery up to 4% in the electron case, whereas no recovery is observed for the proton case. This is also visible in the relative change plot of Fig. 4.7 (c). This effect was already observed in p^+-n GaInP solar cells [68], although a physical

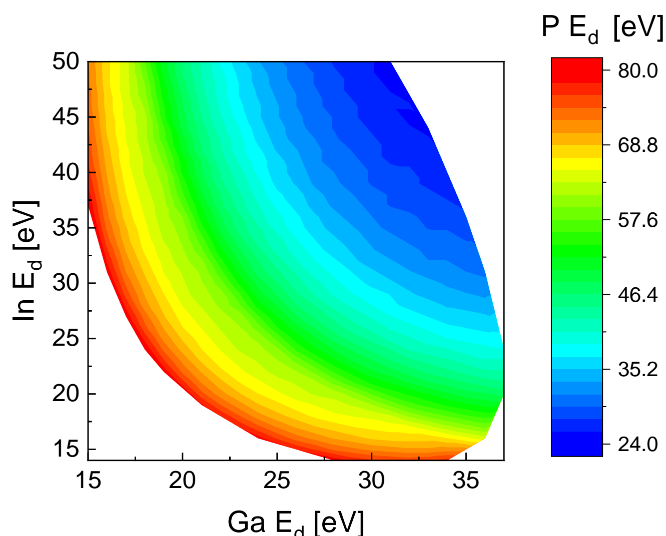

Figure 4.5 – Best Ga, In and P E_d combinations obtained by fitting of the J_{SC} degradation data for $Ga_{0.5}In_{0.5}P$ component cells. The combination shown in the contour plot are the ones producing a fitting result with $2.7{\cdot}10^{-5} < RSS < 3{\cdot}10^{-5}$.

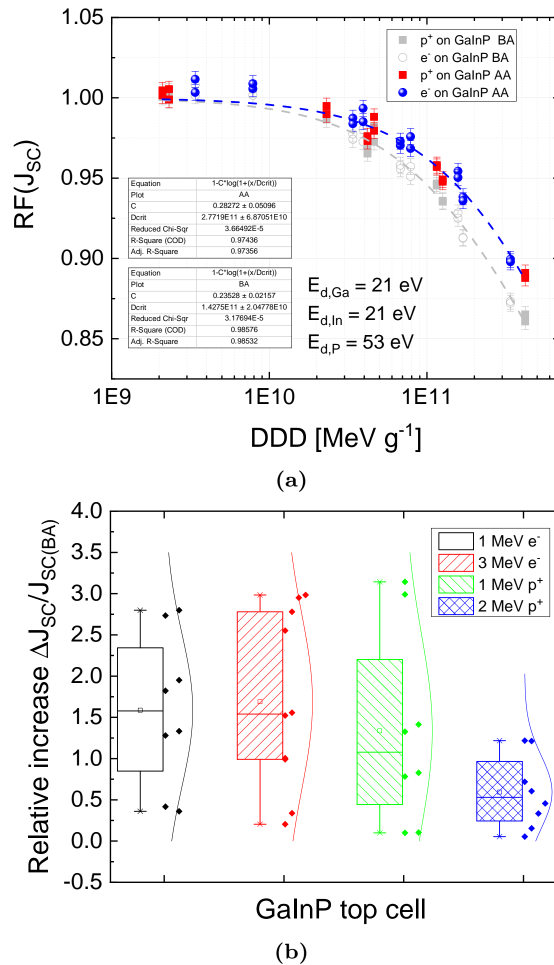

Figure 4.6 – (a) Remaining factors of the J_{SC} in $Ga_{0.5}In_{0.5}P$ component cells as a function of the DDD, calculated with $E_d = 21$ eV, 24 eV and 53 eV for Ga, In and P, respectively. (b) Relative change of the J_{SC} parameter after ECSS annealing.

explanation is still missing. In the AA case, an $R_{ep} = 2.5$ factor is thus required for the proton and electron data to collapse into an unique curve as a function of the DDD. In this case, the origin of the R_{ep} is associated to different V_{OC} recovery observed after annealing of $Ga_{0.5}In_{0.5}P$ irradiated with electrons and protons. As the defect reordering processes leading to V_{OC} recovery are influenced by the initial defect configuration at $T = 300$ K, we can speculate that despite similar V_{OC} damaging effectiveness (no R_{ep} factor required in the BA case), the structural configuration of the V_{OC} damaging defects introduced by proton and electron doses in $Ga_{0.5}In_{0.5}P$ are different, thus leading to a different V_{OC} recovery.

Overall, the top cell exhibits an superior intrinsic radiation hardness and recovery properties with respect to the middle cell, as already shown at a semiconductor level in [69].

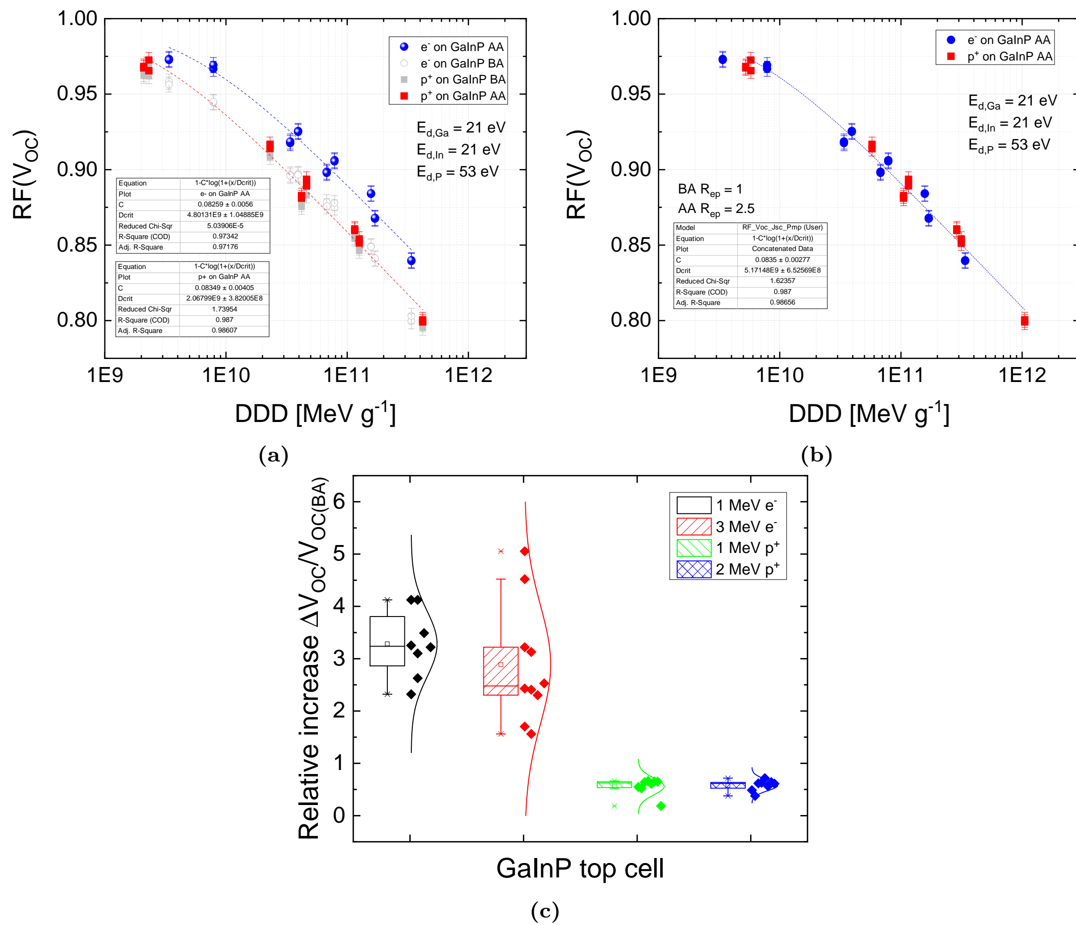

Figure 4.7 – (a) Remaining factors of the V_{OC} in $\mathrm{Ga_{0.5}In_{0.5}P}$ component cells as a function of the DDD, calculated with $E_{\mathrm{d}} = 21\,\mathrm{eV}$ for Ga and As. The proton dose is corrected with the $\mathrm{R_{ep}}$ factor in (b). (c) Relative change of the V_{OC} parameter after ECSS annealing.

4.4 3J solar cell

The 3J solar cell suffers from both the degradation effects of the top and middle sub-cells. The bottom Ge sub-cell, which is not analyzed in this work, also contributes to the degradation of the 3J cell. However, its contribution has in general a lower impact compared to the other sub-cells. This is mainly due to the fact that the Ge bottom cell produces a much higher photo-current than the remaining sub-cells. For typical irradiation doses and temperature conditions in regular space mission, the Ge bottom cell is never in a current limiting regime [53]. As it is the lowest band gap sub-cell, its contribution to the overall cell V_{OC} is small.
The J_{SC} electron degradation data are fitted with the GaAs NIEL. The fitting procedure for the J_{SC} of the 3J solar cell yields a similar hyperbolic curve of Ga and As E_{d} as for the middle cell case, which is expected as GaAs degrades faster than $\mathrm{Ga_{0.5}In_{0.5}P}$ and it operates in current limiting mode. We calculate the NIEL with the standard 21 eV value to be consistent with the analysis of the limiting middle cell reported before.
The J_{SC} and V_{OC} remaining factors are shown in Fig.4.8 (a) and (b), respectively. In (b), the proton data are already corrected with the $\mathrm{R_{ep}}$ factors. Also for the 3J

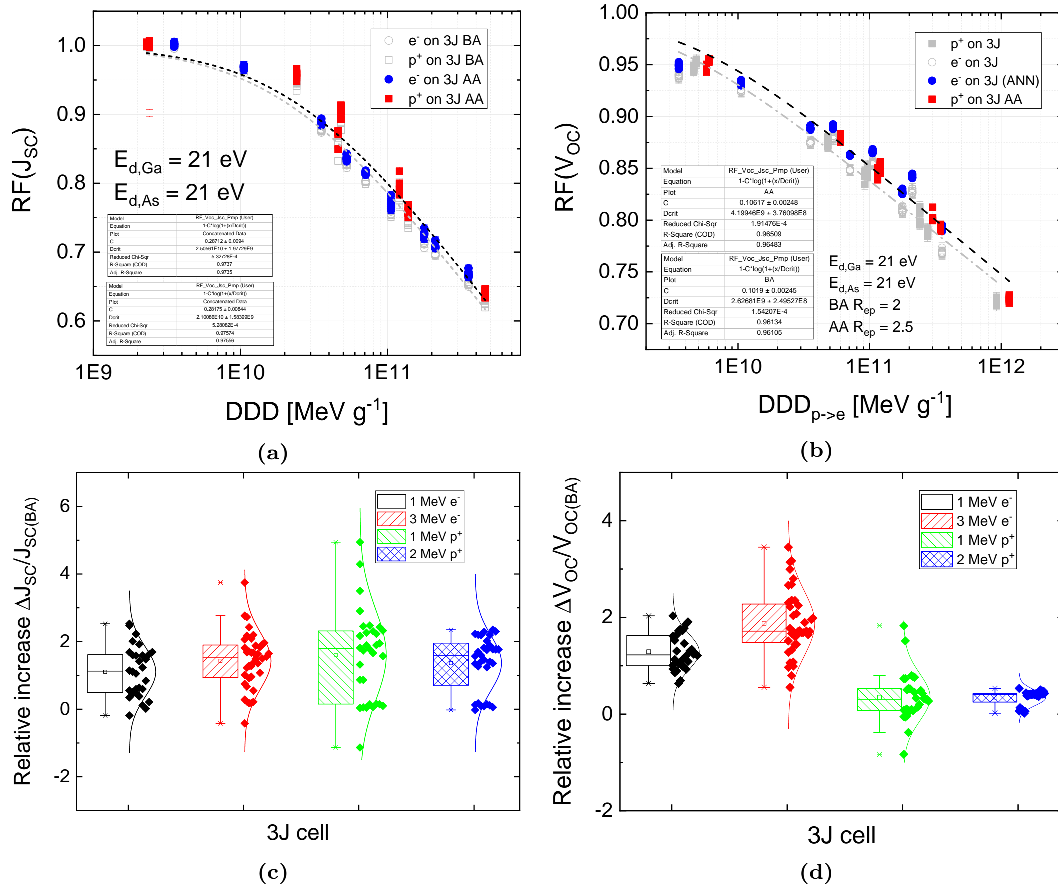

Figure 4.8 – Remaining factors of the (a) J_{SC} and (b) V_{OC} in 3J solar cells as a function of the DDD, calculated with $E_d = 21\,\text{eV}$ for Ga and As. The relative change for J_{SC} and V_{OC} after ECSS annealing is shown in (c) and (d), respectively.

cell, no R_{ep} factor is necessary for J_{SC}. A small recovery effect is observed in both electron and proton irradiated cells, of similar entity compared to the one found in $In_{0.01}Ga_{0.99}As$ middle component cell. In the V_{OC} case, the R_{ep} correction factor is found to be 2 before annealing, and to increase up to 2.5 after annealing. This is readily understood, by considering that the R_{ep} in the 3J cell is a combination of two main corrections required for the middle and top cell voltages. The BA R_{ep} value is mainly due to the different proton dose effectiveness on the voltage of the GaAs sub-cell. A higher R_{ep} value is required in the AA case, as the voltage of the $Ga_{0.5}In_{0.5}P$ cells recovers for the electron irradiation case. The different annealing dynamic is thus responsible for the different R_{ep} correction. From the relative change of the V_{OC} after annealing in Fig.4.8 the two peculiar effects belonging to the middle and top cells are observed: electron with higher energies leads to a more pronounced recovery of the V_{OC}; in the proton-irradiation case, on the other hand, the V_{OC} the effect of the ECSS annealing leads to no significant recovery.

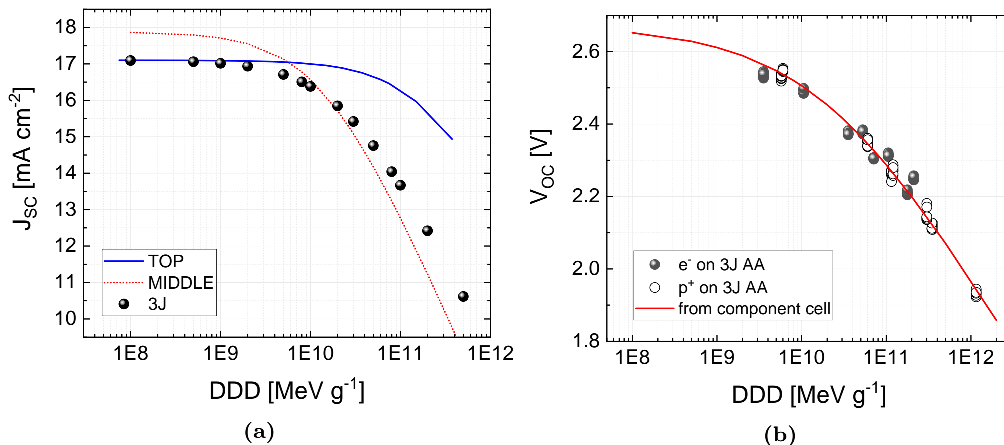

Figure 4.9 – Absolute degradation of the 3J solar cell (a) J_{SC} and (b) V_{OC} as a function of the DDD in GaAs $E_d = 21$ eV for Ga and As atoms. The simulated values obtained via component cell analysis are superimposed. For V_{OC}, the appropriate R_{ep} factors are adopted.

4.5 Quality of component cell-based degradation analysis

The sub-cell electrical degradation data obtained from the component cell analysis are combined to simulate the degradation of the 3J cell. For this analysis, also the bottom component cell data are taken into account. The absolute J_{SC} and V_{OC} degradation measured on 3J cell (symbols) and reconstructed from component cell analysis (lines) are reported in Fig. 4.9 (a) and (b), respectively. The BOL value of J_{SC} in the 3J cell is limited by the top sub-cell. As the irradiation dose increases, the middle sub-cell exhibits more severe current degradation leading to a change of the limiting sub-cell from the top to the middle. This occurs for DDD $> 7{\cdot}10^9$ MeV g^{-1}, which corresponds to a 1 MeV electron fluence of $\Phi \approx 6{\cdot}10^{14}$ cm^{-2}. For higher doses, the degradation of the 3J cell current is determined solely by the degradation of the middle GaAs sub-cell. Despite the good agreement between simulated and actual 3J degradation data, from Fig. 4.9 (a) a misalignment between the middle component cell degradation and the 3J degradation for DDD $> 7{\cdot}10^9$ MeV g^{-1} is observed. The difference diverges to higher values for higher doses. Therefore, the middle sub-cell J_{SC} degradation in 3J solar cell cannot be properly described by using the component cell approach.
Each individual sub-cell contributes in the degradation of the overall 3J cell V_{OC}. The 3J V_{OC} degradation is reproduced with good agreement from component cell analysis, as visible in Fig. 4.9 (b). We can conclude that the approach to component cell for this cell technology gives satisfying results and provides a way to study the radiation damage in the single sub-cells, which are, within reasonable margins, represented by the component cells. At higher doses, the middle component cell degradation data are not anymore fully representative of the actual damage observed in the 3J solar cell.

Chapter 5

Dark Current Degradation

5.1 Two-diode model approach

The dark characteristics of irradiated $In_{0.01}Ga_{0.99}As$ component cells after ECSS standard annealing are fitted with:

$$J_{\text{dark}} = J_{01}(e^{qV/kT} - 1) + J_{02}(e^{qV/nkT} - 1)\,. \tag{5.1}$$

Eq. 5.1 is similar to the standard two-diode model formula in Eq. 2.33, with the only difference that a variable ideality factor n is used for the second exponential term accounting for the recombination current in the SCR.
The extraction of J_{01} and J_{02} from the dark characteristics can pose several challenges. The J_{02} contribution and n are easily extracted since the recombination current dominates the low-medium voltage regime of J_{dark}. The J_{01} contribution, on the other hand, is only observed in the high-voltage bias regime of the solar cell, where the series resistance attenuates J_{dark}. To elude series resistance effects, the dark characteristic is measured in a Suns-V_{OC} fashion, as described in Section 6.2. The dark characteristics measured (symbols) and fitted (lines) with Eq. 2.33 with

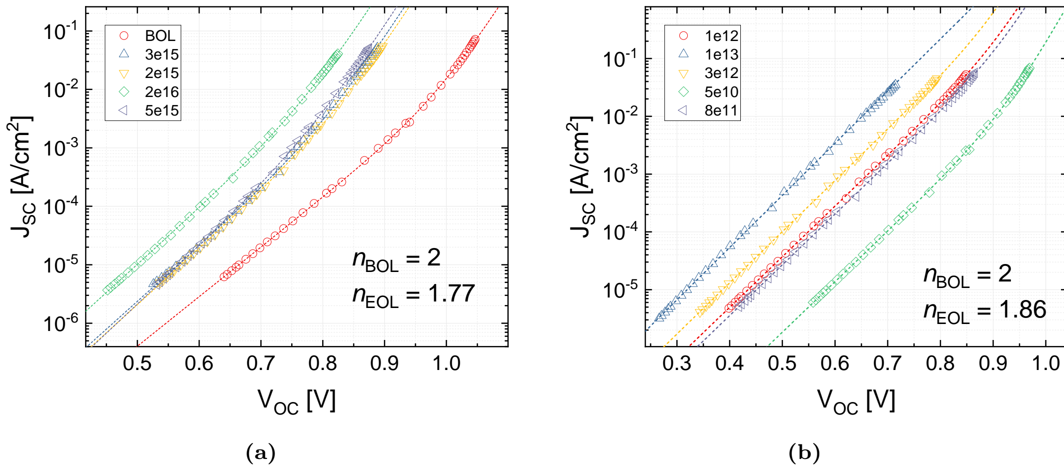

Figure 5.1 – Dark J-V characteristics measured in a Suns-V_{OC} fashion in $In_{0.01}Ga_{0.99}As$ component cells irradiated with 1 MeV electrons and protons at different fluences. Open symbols are the measured data whereas the dotted lines are the fit with Eq. 2.33 with variable n.

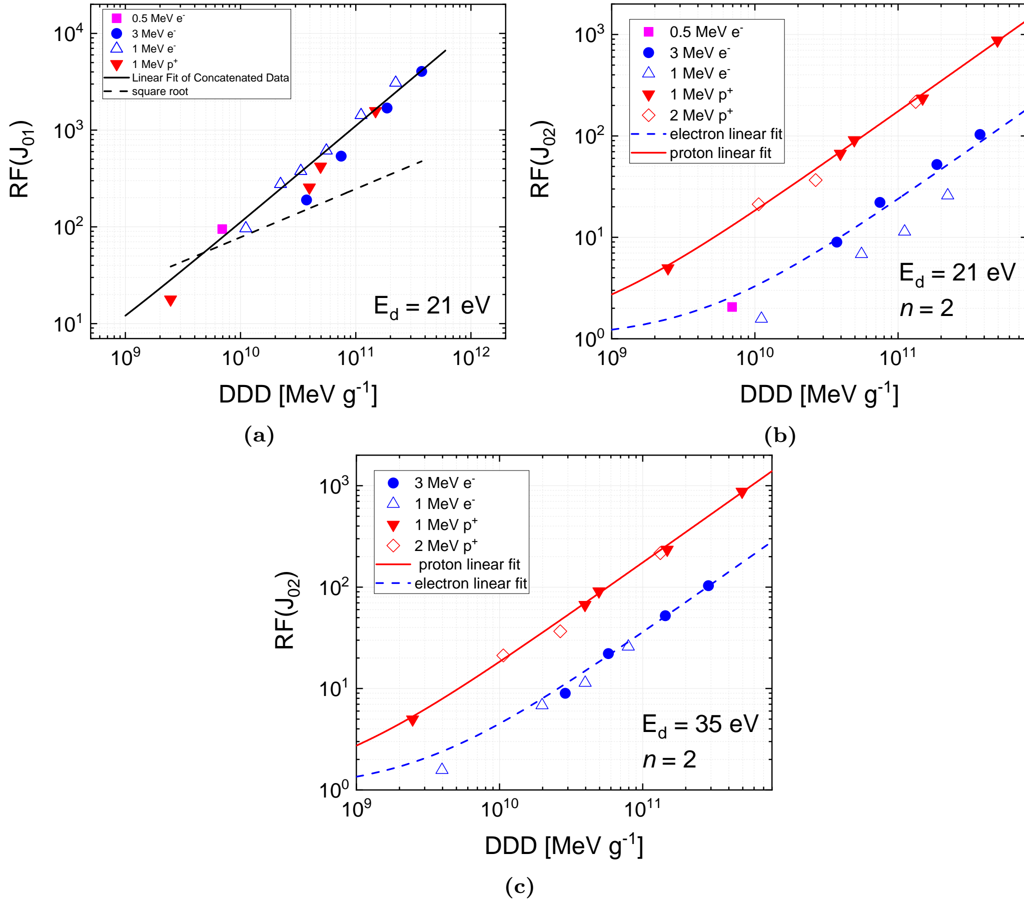

Figure 5.2 – Remaining factors of (a) J_{01} and (b) J_{02} in irradiated $In_{0.01}Ga_{0.99}As$ component cells as a function of the DDD in GaAs calculated with $E_d = 21$ eV. In (b), the J_{02} remaining factors are plotted as a function of the DDD calculated with the $E_d = 35$ eV

variable n are shown in Fig. 5.1 (a) and (b) for the exemplary case of 1 MeV electron and proton irradiation, respectively. The fitting routine with variable n leads to different values of ~1.77 and ~1.86 for the electron and the proton case, respectively. If the dark J-V are fitted with a variable n and each irradiation case produces a slight different n value, the resulting saturation current densities J_{02} cannot be compared. A meaningful degradation analysis on J_{02} entails a fixed n in the fitting process, otherwise small variations of its value would lead to huge variations of J_{02}. Therefore, the dark characteristics are fitted with a constant $n = 2$ for all irradiation cases.

The degradation of J_{01} and J_{02} is studied in terms of remaining factors with the DDD method, as done for the macroscopic PV parameters.

The DDD is calculated by using the same NIEL as determined by the J_{SC} fitting routine in Section 4.2, i.e., assuming $E_d = 21$ eV for Ga and As atoms. The degradation of the J_{01} and J_{02} remaining factors in the exemplary case of the middle $In_{0.01}Ga_{0.99}As$ component cell is depicted in Fig. 5.2 (a) and (b), respectively. The DDD method works well for protons and electrons in the J_{01} case, in analogy with J_{SC}, as both parameters are dominated by the recombination of carriers in the neutral regions of the cell. The same behavior for L_n in the p-type GaAs cells has been

constantly observed and reported by several authors [14], and more recently for a similar $In_{0.01}Ga_{0.99}As$ component cell structure analyzed in this dissertation [70]. It is worth noting that J_{01} exhibits a linear trend with DDD, in contrast to the expected square-root dependence assumed from the theoretical analysis in Eq. 2.39. When the diffusion length of the charge carrier in the quasi-neutral regions is comparable with the layer thickness, a finite surface recombination velocity has to be included in the Shockley diffusion model. Therefore, Eq. 2.36 is no longer strictly valid and Eq. 2.35 should be considered instead. Taking in addition a linear increase of the surface recombination velocities with the DDD into account, the observed linear dependence can be rationalized [71]. However, several other sources of recombination could lead to the linear J_{01} increase observed.

The degradation of J_{02} in Fig. 5.2 (b), on the other hand, shows a big gap between the proton and electron degradation data. An $R_{ep} \sim 9$ is needed to correct the electron dose for this effect [71]. In other words, the DDD of electrons is ~9 times less effective in its impact on J_{02} compared to protons. From this result, a qualitative consideration can be made regarding the degradation of J_{SC} and V_{OC} as well. The current density of the solar cell in short-circuit condition is primarily sensitive to the recombination of minority carriers in the quasi-neutral regions of the p-n junction. Therefore, the independence of L_n and J_{01} on the particle type is consistent with the observed behavior of J_{SC}. On the other hand, V_{OC} has a logarithmic dependence on J_{02}, and this current is not only sensitive to the number of displacements but also to the electrical effectiveness of radiation-induced defects as recombination centers in the band gap. As the degradation of J_{02} is different for proton and electron irradiation, an R_{ep} factor different from 1 is expected for V_{OC} as well. Moreover, the value of $n \neq 2$ implies that the assumption of mid-gap recombination centers is not valid anymore.

In Fig. 5.3 the radiation coefficients (RCs) for (a) J_{SC}, (b) V_{OC} and (c) J_{02} calculated for $In_{0.01}Ga_{0.99}As$ and $Ga_{0.5}In_{0.5}P$ component cells are plotted as a function of the particle NIEL. Data from other ternary and quaternary III-V compound solar cells, not analyzed in details in this dissertation, are plotted for comparison in Fig. 5.3. The symbols are the measured data, whereas the dashed lines are the linear fits which would entail a perfect correlation between RCs and NIEL. It should be reminded that "apparent" linear fits with slopes different from the one reported with dashed lines in Fig. 5.3 imply a non-linear relation in a log-log plot.

A solar cell parameter can be described as a pure function of the DDD only if its RC is linearly proportional to the particle NIEL. The linearity has to be verified across a wide NIEL range as electron and proton NIEL at energies of interest differ by more than three order of magnitude. The RC for J_{SC} exhibit a pure linear trend with the particle NIEL. A similar situation does not exist for V_{OC}, as the data for high-NIEL particles (protons) falls off the linear trend. The ultimate reason for the proton-electron V_{OC} degradation discrepancy is thus ascribed to a non-linearity between the damage coefficient and the particle NIEL. The damage coefficients of J_{02}, reported in in Fig. 5.3 (c), exhibit an even more pronounced non-linearity with the NIEL. The data are best fitted assuming a non-linear relation of the form $RC = NIEL^{\alpha}$, with α ranging between 1.2 and 1.3 according to the different solar cells.

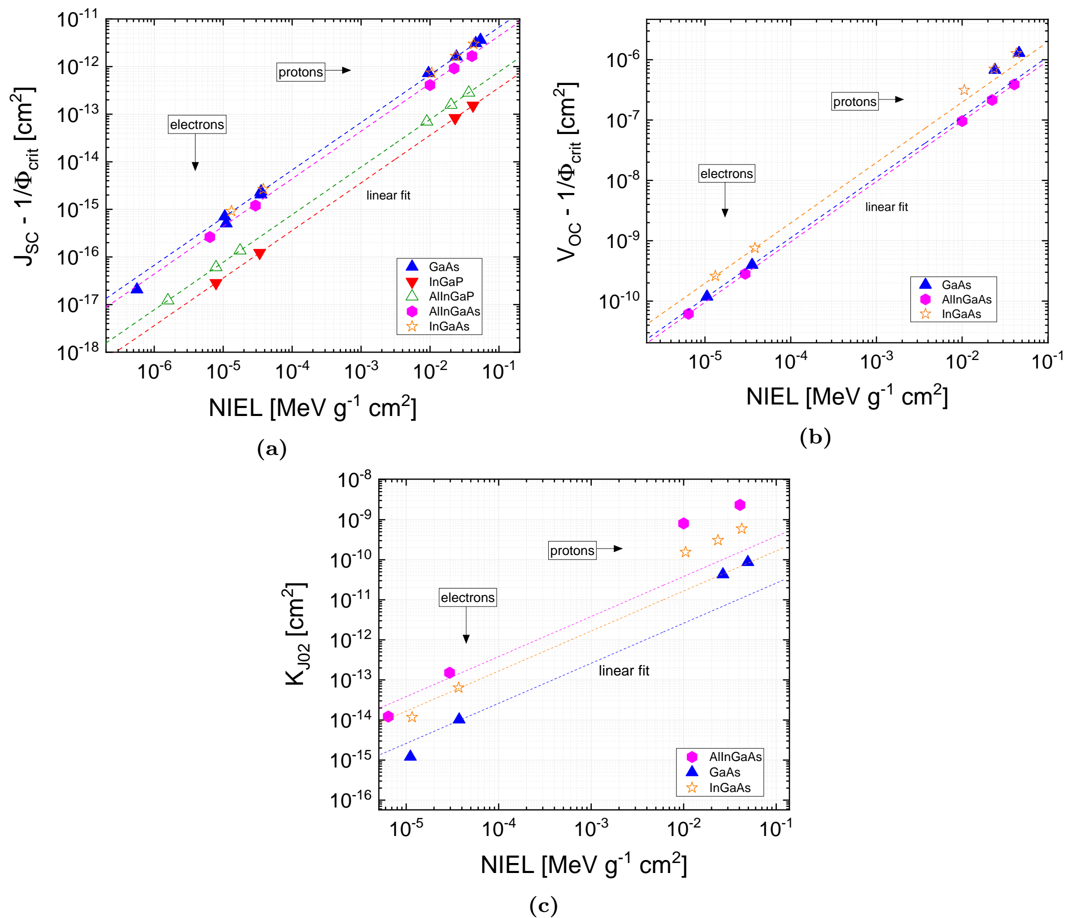

Figure 5.3 – Radiation damage coefficients (RCs) for (a) J_{SC}, (b) V_{OC} and (c) J_{02} obtained from the fitting of the remaining factors in $\mathrm{In_{0.01}Ga_{0.99}As}$ and $\mathrm{Ga_{0.5}In_{0.5}P}$ component cells as a function of the irradiation particle NIEL. The data from other III-V-based component cells, not directly analyzed in this work, are superimposed for comparison.

The results in Fig. 5.3 lead to the conclusion that in III-V solar cell the V_{OC} and J_{02} degradation is not directly proportional to the number of displacements introduced in the active layer of the material. Regardless of the absolute amount of displacements, the damage due to high-NIEL particles (in this case, protons) is more pronounced as compared to the equivalent caused by low-NIEL particles (in this case, electrons). The physical explanation of the non-linearity between the NIEL and the RCs should be traced back to a different electrical effectiveness of the irradiation-induced defects. In order to shed light on this phenomenon, information on defect parameters and their influence on the solar cell PV parameters need to be addressed.

5.2 Recombination current in the space-charge region

To facilitate a more detailed understanding of the different effectiveness of proton and electron displacements on the SCR recombination current, we use a discrete

Shockley-Read-Hall (SRH) recombination model in order to simulate the dark J-V characteristics of irradiated $In_{0.01}Ga_{0.99}As$ component cell[i]. It will be shown that there is a characteristic signature of the type of radiation in the voltage dependence of the junction ideality factor n. By fitting this characteristic curve, it is possible to obtain relative information on the SCR lifetimes associated to mid-gap defect levels.

5.2.1 Shockley-Read-Hall discrete model

When a positive forward bias V is applied across a p-n junction, the defect energy levels act at the same time as trap states and recombination centers [73] in the SCR, according to the values of the imrefs (quasi-Fermi) electrostatic potentials ψ_n, ψ_p for electrons and holes, respectively. In a p-type semiconductor, the energy level is said to behave as a trap state when $E_t > q\psi_p$ and $E_t > q\psi_n$; the holes are trapped in the level, and the re-emission to the valence band is faster than the electron capture rate $(n \cdot \sigma_n)$, thus no recombination occurs. In the volume of the SCR where $q\psi_p < E_t < q\psi_n$, on the other hand, the energy level is referred to as a recombination center, as the carrier emission rate is slower than the relative capture, and non-radiative recombination takes place at the level. The non-radiative recombination kinetic through defect energy levels in the band gap is exhaustively described by the SRH recombination statistics [43]. Assuming only discrete energy levels with negligible thermalization time for trapped carriers compared to the average capture and emission rates, in steady-state conditions the net recombination rate U in the depletion layer is given by Eq. 2.27 where:

$$\begin{aligned} n &= n_i \exp\left[\frac{q(\psi - \psi_n)}{kT}\right]; \\ p &= n_i \exp\left[\frac{q(\psi_p - \psi)}{kT}\right]; \\ E_i &= [E_C - E_V - kT \cdot \ln(N_C/N_V)]/2 = -q\psi\,, \end{aligned} \tag{5.2}$$

with ψ denoting the electrostatic potential.
We shall next choose a spatial reference system on the device structure of Fig. 2.9, the origin of the x axis coinciding with the metallurgical position of the junction, and positive x values toward the p-type region of the cell. The total recombination current density $J_{r,SCR}$ (which replaces the second exponential term in Eq. 5.1) is obtained by integrating $U(x)$ over the SCR width W_{SCR}:

$$J_{r,SCR} = q \cdot \int_{W_{SCR}(V)} U(x)dx\,. \tag{5.3}$$

Let us consider the expression of the recombination rate U as in Eq. 2.27. We shall now define the lifetime asymmetry factor $\chi_\tau = \sqrt{\tau_p/\tau_n}$ and the lifetime geometrical factor $\langle\tau\rangle = \sqrt{\tau_p \cdot \tau_n}$. Since ψ_n and ψ_p are fairly constant in W_{SCR}, it results that $(\psi_p - \psi_n) = V$. Defined $\Delta E_t = E_t$ - E_i, the expression for $U(x)$ due a single

[i]Part of the content of this section is taken from the work in Ref. [71] and [72]

recombination center is derived by substituting Eq. 5.2 in Eq. 2.27:

$$U(x) = \frac{\dfrac{n_\mathrm{i}}{\langle\tau\rangle}\sinh\left(\dfrac{qV}{2kT}\right)}{\cosh\left[\dfrac{q}{kT}\left(\psi - \dfrac{\psi_\mathrm{p}+\psi_\mathrm{n}}{2}\right) + \ln\chi_\tau\right] + \exp\left(\dfrac{-qV}{2kT}\right)\cdot\cosh\left(\dfrac{\Delta E_\mathrm{t}}{kT} + \ln\chi_\tau\right)} \tag{5.4}$$

From Eq. 5.4, it results that the mid-gap states with $E_\mathrm{t} \approx E_\mathrm{i}$ are the most damaging recombination centers. Shallower levels with E_t close to E_C or E_V, on the other hand, are less effective. Integrating Eq. 5.4 according to Eq. 5.3 requires the dependence of the electrostatic potential ψ on the position x in the SCR. Due to the integral nature of $J_\mathrm{r,SCR}$, the maximum contribution of $U(x)$ arises at a position x_m where the recombination rate reaches its maximum value and $\psi(x_\mathrm{m}) = (\psi_\mathrm{p} + \psi_\mathrm{n})/2$. For moderate forward bias V smaller than the built-in voltage V_bi, a linear variation of the electrostatic potential ψ across the SCR can be assumed around x_m:

$$\psi - \frac{\psi_\mathrm{p}+\psi_\mathrm{n}}{2} = \frac{F(x_\mathrm{m})}{2}\cdot(x - x_\mathrm{m}), \tag{5.5}$$

where $F(x_\mathrm{m})$ is the electric field at the position of the maximum recombination rate x_m. In the simpler case of a symmetrically-doped junction, the position $x_\mathrm{m} = 0$ is the metallurgical junction. Thus $F(0) = 2(V_\mathrm{bi}\text{-}V)/W_\mathrm{SCR}$ and Eq. 5.4 assumes the classical Sah-Noyce-Shockley form [46] where the average electric field is used. In an n^+-p junction, the position x_m is shifted toward the p-side of the junction. For strong asymmetrical doping levels $N_\mathrm{d} \gg N_\mathrm{a}$, an expression for $F(x_\mathrm{m})$ is given by solving the Poisson equation in the SCR [74]:

$$F(x_\mathrm{m}) = \sqrt{2kT(\epsilon_0\epsilon_\mathrm{rel})^{-1}\cdot\left[N_\mathrm{a}\ln\left(\frac{N_\mathrm{a}}{n_\mathrm{i}\exp\dfrac{qV}{2kT}}\right) - N_\mathrm{a} + n_\mathrm{i}\exp\frac{qV}{2kT}\right]} \tag{5.6}$$

Combining Eq. 5.6 and 5.5 in Eq. 5.4, the final expression for $U(x)$ becomes:

$$U(x) = \frac{\dfrac{n_\mathrm{i}}{\langle\tau\rangle}\sinh\left(\dfrac{qV}{2kT}\right)}{\cosh\left[\dfrac{qF(x_\mathrm{m})\cdot(x-x_\mathrm{m})}{kT} + \ln\chi_\tau\right] + \exp\left(\dfrac{-qV}{2kT}\right)\cdot\cosh\left(\dfrac{\Delta E_\mathrm{t}}{kT} + \ln\chi_\tau\right)} \tag{5.7}$$

Different analytical and semi-analytical approaches are available in the literature to solve the integral of Eq. 5.3 combined with Eq. 5.7. The most common closed-form solution was proposed by Corkish *et al.* [74], with results very close to the exact numerical solutions for different orders of magnitude of $\langle\tau\rangle$ and χ_τ.
Few consideration on the shape of $U(x)$ allows to treat the integral of in a much easier way for few exceptional cases. At the position $x = x_\mathrm{m}$, the recombination rate

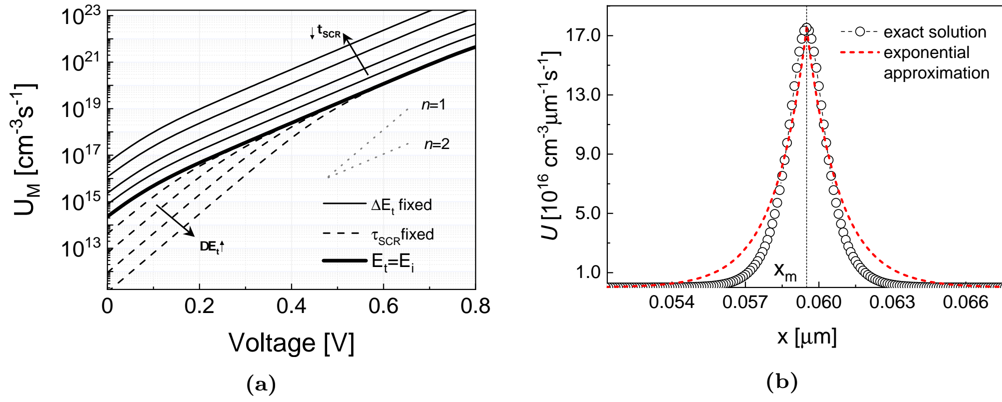

Figure 5.4 – (a) Recombination rate U_{M} as function of the forward bias in a GaAs n^+-p junction simulated with one symmetric ($\chi_\tau = 1$) discrete defect level in the band gap. The dashed curves are obtained using a fixed $\langle\tau\rangle$ value and varying ΔE_{t}. The solid curves are obtained with a constant value of ΔE_{t} and by varying $\langle\tau\rangle$. (b) Recombination rate as a function of the position x-x_{m} in the depletion region for $\Delta E_{\mathrm{t}} = 0$ at an applied bias of 0.3 V. The exact solution is represented by open circles and is obtained with Eq. 5.7, whereas the dotted line shows the exponential model proposed in Eq. 5.10.

in the SCR assumes its maximum value U_{M}:

$$U_{\mathrm{M}} = \frac{\dfrac{n_{\mathrm{i}}}{2\langle\tau\rangle}\exp\left(\dfrac{qV}{kT}\right)}{\exp\left(\dfrac{qV}{2kT}\right) + \cosh\left(\dfrac{\Delta E_{\mathrm{t}}}{kT} + \ln\chi_\tau\right)}. \tag{5.8}$$

In order to facilitate the understanding of the defect parameter influence on the SCR recomination, U_{M} is simulated for a simple GaAs junction SCR for different values of $\langle\tau\rangle$ and ΔE_{t}, and the results are reported in Fig. 5.4 (a). For sake of simplicity, $\chi_\tau = 1$ is assumed. In this case, $\langle\tau\rangle$ becomes the SCR lifetime τ_{SCR}. The solid curves are obtained keeping a constant value of $\langle\tau\rangle$ and varying the position of the recombination center in the band gap ΔE_{t} from 0.05 eV to 0.3 eV. The dashed curves are obtained maintaining a fixed value of ΔE_{t} and decreasing the recombination lifetime from 1 ns to 5 ps. At low voltages, the hyperbolic cosine term in the denominator of Eq. 5.8 dominates, resulting in an overall trend $\exp(qV/kT)$. This term is governed by the energy level ΔE_{t}. At higher voltages, on the other hand, the exponential term in the denominator has the larger influence resulting in an overall slope $\exp(qV/2kT)$. In between, there is a transition region where Eq. 5.8 is effectively approximated by an exponential law $\exp(qV/nkT)$, where n varies between $1 < n < 2$. In the more general case of χ_τ not equal 1, the same interpretation holds with the only difference that the hyperbolic cosine term in the denominator of Eq. 5.8 is governed by both contribution of the energy level and lifetime asymmetry. By considering the two asymptotic cases, it is possible to calculate the transition voltage V_{tr} at which the change in slope occurs. An expression for V_{tr} in the general case of asymmetric lifetime is given [75]:

$$qV_{\mathrm{tr}} = 2\left[\Delta E_{\mathrm{t}} - kT\ln(2) + kT\ln(\chi_\tau)\right]. \tag{5.9}$$

By varying the position of the defect energy level and the lifetime asymmetries, the transition voltage sweeps along the voltage abscissa. The value $\langle\tau\rangle$, on the other hand, has no influence on the slope of the curve. Decreasing $\langle\tau\rangle$ results in an upward shift of the recombination rate. The more general asymmetric case ($\chi_\tau = 1$) can be brought back to a the symmetric case depicted in Fig. 5.4 (a) by considering the value ΔE_t as an equivalent energy level, being the sum of the contribution of the actual energy level and the factor $kT \ln \chi_\tau$. For applied bias $V > V_\mathrm{tr}$, $U(x)$ is strongly peaked in the SCR around $x = x_\mathrm{m}$. The spatial dependence of $U(x)$ is approximated by combining U_M with an exponential decay:

$$U(x) = U_\mathrm{M} \cdot \exp\left(-\frac{qF(x_m)}{kT}\frac{1}{\alpha}|x|\right) \tag{5.10}$$

where $\alpha = \pi/2$ is a constant allowing to fit the exact solution of $U(x)$ with the exponential approximation, as shown in Fig 5.4 (b). As the recombination rate is strongly peaked around x_m, the integration of Eq. 5.3 can be extended from -∞ to $+\infty$, making the total recombination rate independent from the actual value of x_m. By combining Eq. 5.10 and 5.8 in Eq. 5.3, $J_\mathrm{r,SCR}$ can be solved analytically. In the simplest case of $\Delta E_\mathrm{t} = 0$, this leads to the expression in Eq. 2.40. As the voltage dependence of $F(x_\mathrm{m})$ is only contributing to the overall voltage-dependence of $J_\mathrm{r,SCR}$ at bias voltages above 0.8 V, the considerations regarding the slope of U_M applies the same way for $J_\mathrm{r,SCR}$.
The analytic model is further refined by including the contribution of trap-assisted tunneling (TAT) recombination. Because of the high doping levels, the electric field can aid the charge-carriers to tunnel part of the band gap, and eventually they recombine through the defect levels, thus lowering the effective $\tau_\mathrm{n,p}$ and increasing the net recombination rate. At lower temperatures, the tunneling probability increases. This process was extensively described by Hurkx *et al.* [76] for Dirac-like wells. The TAT contribution is directly modeled by re-writing Eq. 2.27:

$$U = \frac{pn - n_\mathrm{i}^2}{\frac{\tau_\mathrm{p}}{1+\Gamma_\mathrm{p}}\left(n + n_\mathrm{i} e^{\frac{\mathrm{E_t - E_i}}{\mathrm{kT}}}\right) + \frac{\tau_\mathrm{n}}{1+\Gamma_\mathrm{n}}\left(p + n_\mathrm{i} e^{\frac{\mathrm{E_i - E_t}}{\mathrm{kT}}}\right)}, \tag{5.11}$$

where Γ_n and Γ_p are the field-effect functions influencing the effective lifetime of the energy level. The contribution can be accounted in the exponential approximation model by employing effective carrier lifetimes $\tau^*_\mathrm{n,p}$ obtained as the ratio $\tau_\mathrm{n,p} \,/\, (1 + \Gamma_\mathrm{n,p}(V))$, where $\tau_\mathrm{n,p}$ are the lifetimes without considering the TAT contribution. The analytic implementation of the $\Gamma_\mathrm{n,p}(V)$ functions is not straightforward. Therefore, $\Gamma_\mathrm{n,p}(V)$ are determined from numerical simulations with the software TiberCad [77]. Since the dependence of $\Gamma_\mathrm{n,p}(V)$ over ΔE_t and V is found to be negligible in most of the cases analyzed, the TAT contribution does not introduce additional complexity in the model.

5.2.2 Fitting of the inverse ideality factor

$J_\mathrm{r,SCR}$ dominates J_dark in irradiated $\mathrm{In_{0.01}Ga_{0.99}As}$ devices up to bias range as high as 0.8 V. The influence of a defect level in the voltage-dependent $J_\mathrm{r,SCR}$, expressed

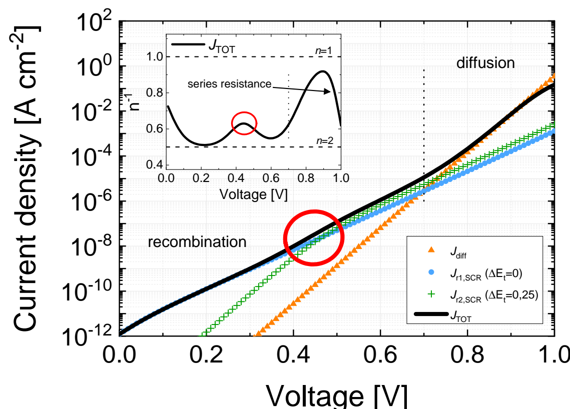

Figure 5.5 – Simulated dark J-V characteristic of a GaAs n^{+}-p junction. The recombination current in the SCR is due to two symmetrical defect levels in the band gap, with different values of $\langle\tau\rangle$ and with energy levels $E_{t,1} = E_i$ (light blue dots), and $E_{t,2}$ shifted 0.25 eV from E_i (green crosses). The contribution of the series resistance and the diffusion component (orange triangles) are included in the model. The inverse ideality factor as function of the applied bias is shown in the inset.

by Eq. 5.8, is monitored by the voltage dependence of the reciprocal ideality factor:

$$n^{-1}(V) = \frac{kT}{q}\frac{\mathrm{d}\ln\left(J_{dark}\right)}{\mathrm{d}V} \tag{5.12}$$

n^{-1} is highly sensitive to the slope change in U_{M} thanks to using the derivative of the logarithm of the dark saturation current with respect to voltage. For a two-diode model and a single-level defect, n^{-1} is constant at a value of 1 in the diffusion regime, and assumes a value of 0.5 in a perfect ($\Delta E_{\mathrm{t}} = 0$) recombination regime ($n = 2$). At higher bias levels, n^{-1} is affected by the series resistance resulting in a downward bending. In reality, however, when several levels away from E_{i} are introduced through particle irradiation, n^{-1} is not constant anymore in the recombination regime.
In order to facilitate the understanding of the energy level influence on the device current, the SRH analytic model is used to simulate the dark J-V characteristic of a GaAs n^{+}-p junction considering two discrete symmetric defects ($\chi_{\tau} = 1$) at $E_{t,1} = E_i$ and $E_{t,1} = E_i + 0.25\,\mathrm{eV}$. The simulation results are shown in Fig 5.5. In the inset of Fig 5.5, the voltage dependence of n^{-1} is reported. The dark current density of the device is simulated as:

$$J_{\mathrm{dark}} = J_{\mathrm{diff}} + J_{\mathrm{r1,SCR}} + J_{\mathrm{r2,SCR}}\,, \tag{5.13}$$

where J_{diff} is the diffusion component expressed by the Shockley equation [44], while $J_{\mathrm{r1,SCR}}$ and $J_{\mathrm{r2,SCR}}$ are the recombination current contributions related to the two defects. On the basis of the individual plots of these contributions, two main regimes can be identified. In the low-bias region below 0.7 V, the current due to recombination in the SCR dominates. For higher bias voltages, J_{diff} dominates, and the ideality factor approaches one. As the current increases, the effect of the series resistance appears, resulting in a decrease of n^{-1} again at high voltages. In the recombination regime, the electrical characteristic of the energy levels completely

determine the n^{-1}-V curve. For a single defect level, there is only a change in the slope from $n = 1$ to $n = 2$ at V_{tr}, which is governed solely by the energy level of the defect. For this example, at ~0.1 V for $E_{\mathrm{t,1}}$ and ~0.45 V for $E_{\mathrm{t,2}}$. In the combination of the two, however, it is possible to reach a turning point in the n^{-1}-V curve as shown in the inset of Fig. 5.5. Its position is again determined by the energy level of the defect with the larger ΔE_{t}. The parameter n^{-1} is sensitive to changes in the slope of the dark current, which are in turn completely determined by the electrical characteristics of the defects in the SCR. With the help of this formalism, it is possible to consider the contributions of discrete energy levels in the band gap of the SCR on the experimentally measured recombination current, provided the diffusion contribution or a series resistance effect are not affecting the overall cell current in the voltage region of interest.
The dark current J_{dark} of irradiated component cells are fitted with:

$$J_{\mathrm{dark}} = J_{01}(\exp(qV/kT) - 1) + J_{\mathrm{r,SCR}} \tag{5.14}$$

To avoid an ambiguous fit, J_{01} is extracted by Suns-V_{OC} measurements in the high-voltage range at $T = 300$ K. The voltage dependence of n^{-1} is used as central functional for the fitting process. The experimental n^{-1}-V characteristic is fitted by including k different energy levels around mid gap. The transition voltage V_{tr} associated to the k-th defect has a key role for the fitting of the n^{-1} characteristics. The fitting parameters to be determined are ΔE_{t}, $\langle\tau\rangle$ and χ_τ which are related to the physical parameters of the k-th energy level. In order to converge to a unique solution, the assumption of symmetrical defects is made. With $\chi_\tau = 1$, $\langle\tau\rangle$ is the SCR lifetime for both carriers τ_{SCR}. The assumption of symmetrical defects is essential, since neither the methods employed in this experiment nor consistent literature data provide information on the actual value of χ_τ for irradiation-induced defects in GaAs. The ΔE_{t} values are chosen to match deep levels in p- and n-type irradiated GaAs listed in the literature [78, 79], consistent with the values detected via defect spectroscopy in Chapter 3.2.3. If a deviation of ΔE_{t} from the real defect energy level is required to properly fit the experimental curve, it can be interpreted as the effect of a defect capture asymmetry factor different from one. The fitting process involves only the overall lifetimes τ^*_{SCR}, where the star indicates that the TAT contribution is also taken into account in the model.
In Fig. 5.6 (a), the n^{-1}-V characteristics at $T = 300$ K are shown for the proton and electron case with an equivalent DDD $\approx 2{\cdot}10^{11}$ MeV g^{-1}, estimated by using $E_{\mathrm{d}} = 21$ eV in the NIEL calculation. The contribution of each defect level is localized in the n^{-1}-V characteristic around the related V_{tr}. n^{-1} is accurately reproduced only when all the required energy levels are included. This is shown exemplary in Fig. 5.6 (b). The assumption of symmetrical defects is equivalent with an uncertainty in the defect energy levels. When fitting the characteristic due to a defect with $\chi_\tau \neq 1$ while adopting a symmetrical model (forcing $\chi_\tau = 1$ in the simulation), the resulting value ΔE_{t} in the fitting of a particular n^{-1} voltage transition can be interpreted as an equivalent energy level, being the difference of the contribution of the actual energy level and χ_τ according to Eq. 5.9. For instance, the difference between the actual and the adopted ΔE_{t} for an asymmetrical level with $\chi_\tau = 10^3$ is 90 meV.

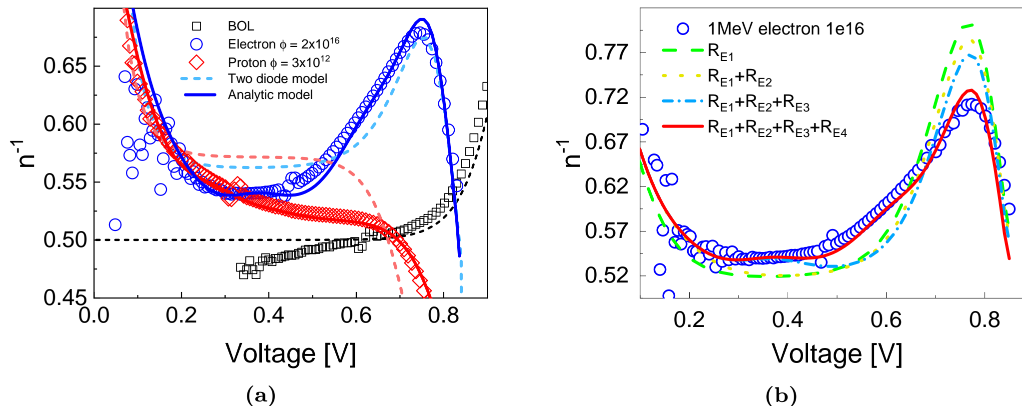

Figure 5.6 – (a) n^{-1}-V characteristics of the unirradiated (black squares), proton (red diamonds) and electron (blue circles) irradiated $In_{0.01}Ga_{0.99}As$ component cells. The dashed curves represent the fit with the two-diode model, whereas the continuous lines are the fit with the recombination model. The two-diode model fit is obtained with $n = 1.78$ in the electron case and $n = 1.75$ in the proton case. (b) Stepwise fitting of the n^{-1}-V characteristic of electron irradiated $In_{0.01}Ga_{0.99}As$ component cells at $\Phi = 10^{16}\,\mathrm{cm}^{-2}$ fluence, using the recombination centers R_{E1-E4}.

The energy range of defects, whose contribution can be detected in the n^{-1}-V plot, is defined by the voltage range where $J_{\mathrm{r,SCR}}$ dominates over J_{diff} as the main current contribution in the dark J-V. Since the ratio $J_{\mathrm{diff}}/J_{\mathrm{r,SCR}}$ is proportional to n_{i}, the dark J-V curve at lower temperatures is dominated up to higher voltages by $J_{\mathrm{r,SCR}}$, thus extending the accessible energy range. To summarize, the following main assumptions for this method have been made:

- Defects are homogeneously distributed in the SCR and can be treated as discrete energy levels in the band gap;
- The recombination centers are symmetric, i.e. the lifetime for electrons and holes are equal and $\chi_\tau = 1$;
- the contribution of each discrete level to the overall current density can be taken into account separately, i.e. inter-band dynamics are not taken into account;

Under this conditions, the SCR lifetime associated to the recombination centers can be extracted by fitting of the n^{-1}-V curves. The weakness of the model employed due to the number of assumptions and simplifications in treating discrete energy levels with symmetric lifetime constraint prevents absolute considerations to be done. Indeed, the method proposed in this section is far from describing the material quality in absolute term. For defect analysis, it suffers the inability to resolve the absolute energy position of the defect levels with respect to E_{C} or E_{V}. The intrinsic symmetry of the SRH statistics ensures that the current contribution of a defect in the SCR is only a function of the absolute value ΔE_{t}, no matter toward which band the energy level is displaced from E_{i}.
However, relative conclusions on the overall SCR lifetime damage between the proton and electron case can be drawn. A summary of the fitting results is reported in Table. 5.1.

	1 MeV p^+					
	R_{P1}	R_{P2}	R_{P3}	R_{P4}	R_{P5}	R_{P6}
	$\lvert E_t - E_i \rvert$ [eV]					
	0.03	0.07	0.15	0.22	-	-
Fluence [cm^{-2}]	τ_{SCR}[ns]					
5e10	6.3	10	(25)	5	-	-
1e12	0.3	0.48	1.2	3	-	-
3e12	0.1	0.3	0.4	-	-	-
1e13	0.04	0.06	0.08	0.12	-	-
	1 MeV e^-					
	R_{E1}	R_{E2}	R_{E3}	R_{E4}	R_{E5}	R_{E6}
	$\lvert E_t - E_i \rvert$ [eV]					
	0.04	0.10	0.21	0.33	0.39	0.45
Fluence [cm^{-2}]	τ_{SCR}[ns]					
1e15	10	-	-	30	-	-
5e15	4.5	18	18	6.7	(50)	10
1e16	2	10	10	3	7	2
2e16	1	3	4	2	3	1

Table 5.1 – Recombination centers in 1 MeV proton and electron irradiated $In_{0.01}Ga_{0.99}As$ component cells. The values in brakets may suffer of large errors.

5.2.3 Fitting results

At $T = 300$ K the detection range in the band-gap is approximately $\Delta E_t < 0.35$ eV due to the onset of J_{diff}. Four recombination centers were used to fit both proton and electron dark J-V and n^{-1}-V characteristics. The resulting lifetimes are reported in Table 5.1. The quality of the model is assessed by solving numerically the drift-diffusion equations with a TCAD simulation software TiberCad [77], and a maximum error on the lifetimes of 50% is found. The TAT contribution is evaluated by means of the implemented Hurkx model in the TiberCad software, and a Γ factor of 2 is found, fairly independent of the applied bias. The recombination current in the dark J-V characteristic is adequately reproduced in both proton and electron cases. The dark J-V and n^{-1}-V characteristics fitted at $T = 300$ K are reported in Fig. 5.7.

The accessible energy range is extended when the solar cells are measured at $T = 210$ K. A temperature lower than 210 K is not accessible, however, since the properties of the charge-carrier transport at the cell BSF have been found to change drastically, thus affecting the dark J-V characteristics and leading to erroneous results in the recombination model. For the electron case, the n^{-1}-V plots at $T = 210$ K are shown in Fig. 5.8 (a). Two additional recombination centers are required, approximately located at $\Delta E_t = 0.38$ eV and 0.45 eV, in order to obtain a good fit. Also, in the 210 K case, numerical simulations show that the factor Γ is a weak function of the voltage, and a constant value of $\sim$3 for the TAT contribution can be considered. For the proton case, on the other hand, the analysis does not lead to any further defect level, since the n^{-1}-V curves are flat along the whole analyzed voltage range. In Fig. 5.8 (b) the measured and simulated dark J-V curves for the whole temperature

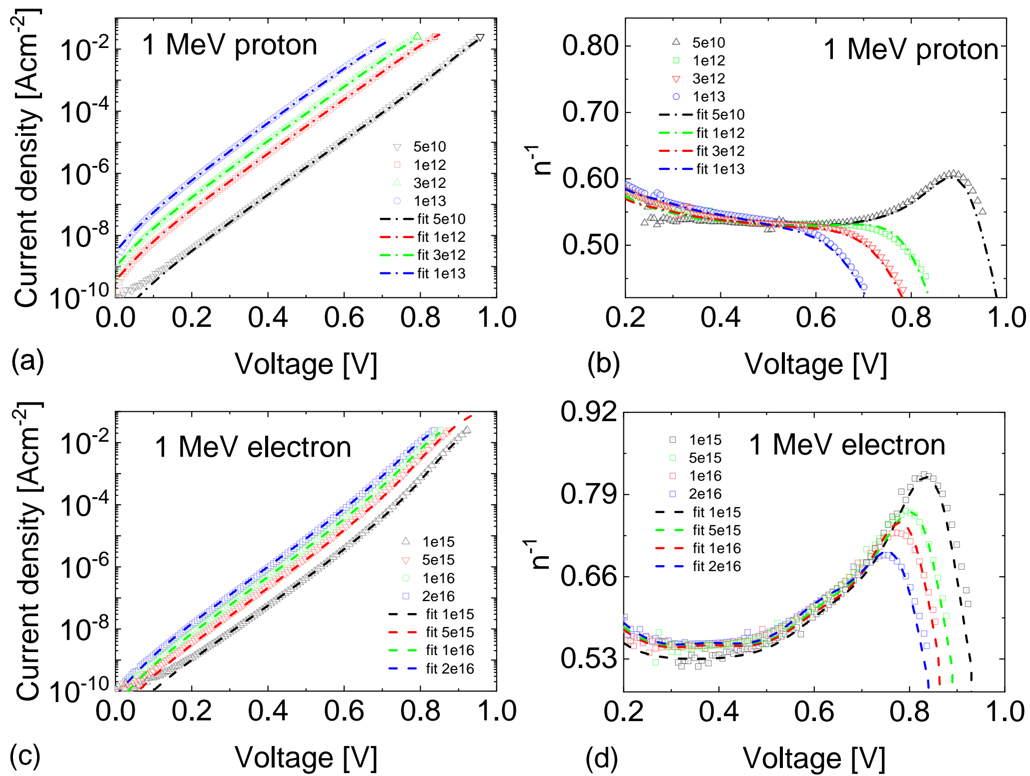

Figure 5.7 – Fitting of the dark J-V characteristics and of the n^{-1}-V for (a,b) 1 MeV proton and (c,d) 1 MeV electron irradiated $In_{0.01}Ga_{0.99}As$ component cells at 300 K.

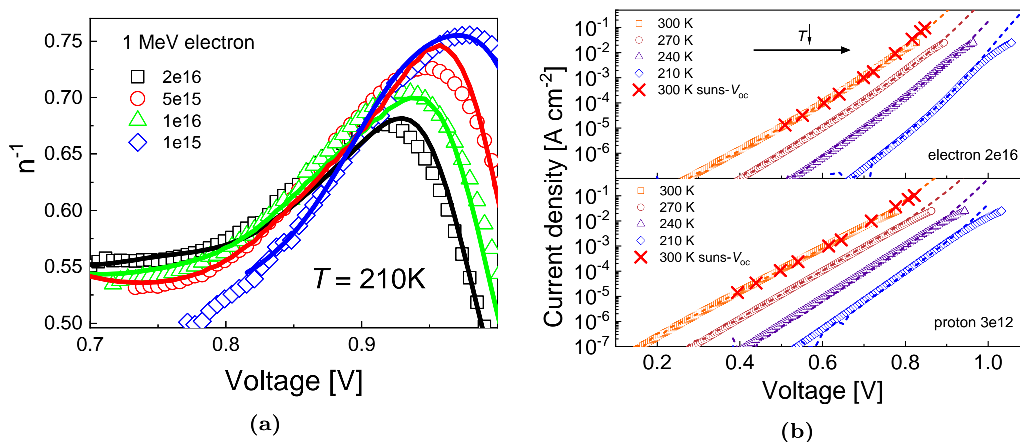

Figure 5.8 – (a) Measured (symbols) and simulated (lines) n^{-1}-V characteristics for 1 MeV electron irradiated $In_{0.01}Ga_{0.99}As$ component cells at various fluence values and at a temperature $T = 210$ K. (b) Temperature-dependent dark J-V characteristics of 1 MeV electron and proton irradiated $In_{0.01}Ga_{0.99}As$ component cells with same amount of DDD deposited, calculated with $E_d = 21$ eV deposited. The symbols are the measured data, whereas the lines are obtained via numerical simulations with the software TiberCad through adjusting the actual lifetime in the neutral regions. The Suns-V_{OC} data measured at $T = 300$ K are also superimposed (red crosses).

range analyzed are reported.

5.2.4 Conclusion on the electron- and proton-induced recombination current

The intrinsic limitations of the simple analytic model to describe the dark current of irradiated $In_{0.01}Ga_{0.99}As$ cells shown in this section prevent absolute considerations on the τ_{SCR} values extracted from the fitting procedure to be made. However, qualitative considerations on the proton-electron difference in $J_{r,SCR}$ degradation can be made. In order to discuss the difference in the proton and electron data, it is instructive to compare the cells with a proton fluence $3\times10^{12}\,cm^{-2}$ to the cell with an electron fluence of $2\times10^{16}\,cm^{-2}$. These two particle-fluence combinations deposit the same displacement damage dose $DDD \approx 2\times10^{11}\,MeV\,g^{-1}$ in the crystal (calculated with $E_d = 21\,eV$), thus leading to a similar degradation of J_{SC}. For the energy levels closer to mid gap, the lifetimes in the proton irradiated samples are one order of magnitude smaller than in the electron case. Assuming a comparable capture cross section for proton and electron-induced defects for these levels close to E_i, protons produce one order of magnitude more defects close to the intrinsic level than electrons, with the associated high effectiveness as recombination centers in the SCR. Since the same amount of non-ionizing energy is deposited in both cases, a significant amount of electron defects must therefore be distributed in a wider energy range. Alternatively, assuming that protons and electrons introduce the same energy levels, the effect can be explained assuming a higher capture cross-section for the proton-induced mid-gap defects with respect to the equivalent electron-induced defects. This would lead to a total defect concentration proportional to DDD, but to a different $J_{r,SCR}$ degradation due to the different capture cross-sections of the mid-gap defects, which in turns leads to a different effectiveness on the V_{OC} degradation. This ambiguity can only be solved by probing the defect electrical properties in irradiated $In_{0.01}Ga_{0.99}As$ by using more accurate techniques such as defect spectroscopy.

Chapter 6

Admittance spectroscopy on $In_{0.01}Ga_{0.99}As$ middle component cell

6.1 Introduction

In irradiated $In_{0.01}Ga_{0.99}As$ component cells following a standardized annealing regime [22], the J_{SC} degradation curve can be fitted with a pure function of the DDD for all electron and proton energies in the range of interest if an adapted threshold energy of $E_d = 21\,eV$ is used in the NIEL calculation, as shown in Section 4.2. The degradation behavior of the open-circuit voltage V_{OC} and the recombination current density J_{02}, however, differ significantly from the J_{SC} trend. In particular, two features were observed in $In_{0.01}Ga_{0.99}As$ cells: I) the proton DDD is more effective than the electron DDD in damaging V_{OC} and J_{02}, as visible in Fig. 4.4 and Fig. 5.2 (b); II) the adapted value $E_d = 21\,eV$ leads to a good fit of the V_{OC} electron data only in the low-medium dose range, and to a poor fit of the J_{02} electron data for all fluence values. For the latter parameter, a higher $E_d = 35\,eV$ would result in a better fit of the high-energy electron spectrum above 1 MeV, as shown in Fig. 5.2 (c). With this E_d value, however, the NIEL of 0.5 MeV electrons would be virtually zero, in contradiction with the slight J_{02} degradation observed for this electron energy, as visible in Fig. 5.2 (b).
In Chapter 4 and 5 it has been shown that $R_{ep}^{V_{OC}} \approx 2.5$ and $R_{ep}^{J_{02}} \approx 9$.
A detailed knowledge of the defects produced by the displacement damage and their electrical effectiveness on the macroscopic cell parameters would allow the physical meaning behind the R_{ep} factors and the adapted E_d values adopted in the treatment of the solar cell remaining factors to be understood. Defect characterization in representative space component cells has only been performed with deep-level transient spectroscopy (DLTS) on ad-hoc mesa diode structures [80] due to the capacitance limits for DLTS measurements. A similar characterization of different solar cell technologies has been performed by several authors [81, 82] by means of non-transient capacitance methods. Admittance spectroscopy proved to be a suitable tool for defect characterization in standardized $2\,cm \times 2\,cm$ $In_{0.01}Ga_{0.99}As$ component cells irradiated with protons and electrons at different energies and fluences[i]. This is beneficial, as the defect analysis can be performed on actual space component cells

[i]Part of the content of this section is taken from the work in Ref. [83]

manufactured for radiation effect analysis. The combined admittance-NIEL analysis suggests physical explanations for the values of E_d and the R_{ep} adopted in the DDD treatment of GaAs-based solar cell degradation data

6.2 Experimental details

For the defect spectroscopy analysis, the acceptor concentration $N_a = 4\times10^{16}\,cm^{-3}$ and the donor concentration $N_d = 10^{18}\,cm^{-3}$ were assumed for the absorber and emitter layers, respectively. All relevant material parameters for $In_{0.01}Ga_{0.99}As$ were taken from literature data [84]. The irradiation history of all samples is summarized in Table 6.1. Following irradiation, the solar cells were annealed in three steps: I) 48h under AM0 condition at $T = 300\,K$; II) 24h in dark conditions at $T = 333.15\,K$ and III) 24h in dark conditions at $T = 370\,K$. Annealing steps I and II were performed in accordance with the relevant ECSS space standards [22], whereas step III was performed to ensure stable conditions during the admittance measurements which were carried out up to this temperature.

The admittance of the solar cells was measured as described in Section 3.2.2, whereas the data analysis was performed on the basis of the theory laid down in Section 3.2.3.

Table 6.1 – Irradiation history of $In_{0.01}Ga_{0.99}As$ Component Cells for defect spectroscopy.

Particle	Energy [MeV]	Fluence [cm^{-2}]	Facility	n. of samples
e^-	0.5	1.4×10^{16}	TU Delft	2
e^-	1	1×10^{15}	TU Delft	1
e^-	1	2×10^{15}	Sirius	1
e^-	1	3×10^{15}	Sirius	1
e^-	1	5×10^{15}	TU Delft	2
e^-	1	1×10^{16}	TU Delft	2
e^-	1	2×10^{16}	TU Delft	2
e^-	3	2×10^{15}	TU Delft	2
e^-	3	5×10^{15}	TU Delft	2
e^-	3	1×10^{16}	TU Delft	2
p^+	1	8×10^{11}	CSNSM Orsay	1
p^+	1	1×10^{12}	CSNSM Orsay	1
p^+	1	3×10^{12}	CSNSM Orsay	2
p^+	1	1×10^{13}	CSNSM Orsay	2
p^+	2	4×10^{11}	CSNSM Orsay	1
p^+	2	2×10^{12}	CSNSM Orsay	1
p^+	2	5×10^{12}	CSNSM Orsay	2

6.3 Admittance evaluation

6.3.1 General considerations

A representative C-f-T spectra for irradiated $In_{0.01}Ga_{0.99}As$ solar cell is illustrated in Fig. 6.1. Two main capacitance steps CS_1 and CS_2 are visible in the blue and orange area of the plot, respectively. On the f-T plane, the projection of the function -$f\mathrm{d}C/\mathrm{d}f$ facilitates to pinpoint the f_t-T tracks. The evolution of CS_1 and CS_2 with temperature occurs separately in different areas of the f_t-T plot without significant overlap: CS_1 in the range $\mathrm{LT} = \{190\,\mathrm{K} < T < 260\,\mathrm{K}\}$ and CS_2 in the range $\mathrm{HT} = \{290\,\mathrm{K} < T < 370\,\mathrm{K}\}$. The drop-off at high frequencies is caused by the resonance of the total cell capacitance with the stray inductance of the external circuit. At low temperatures, the hole conduction at the BSF hetero-interface [85] results in a big capacitance drop. It limits the accessible frequency range and masks the effect of potential shallower levels below 190 K.
The fitting of the C-f-T surface with Eq. 3.9 requires the knowledge of the exact value of $C_{\mathrm{SCR}}(T)$ from which in turn $N_{\mathrm{a}}(T)$ and later $N_{\mathrm{t_0}}$ can be accurately determined. Theoretically, C_{SCR} could be easily extracted for every temperature as

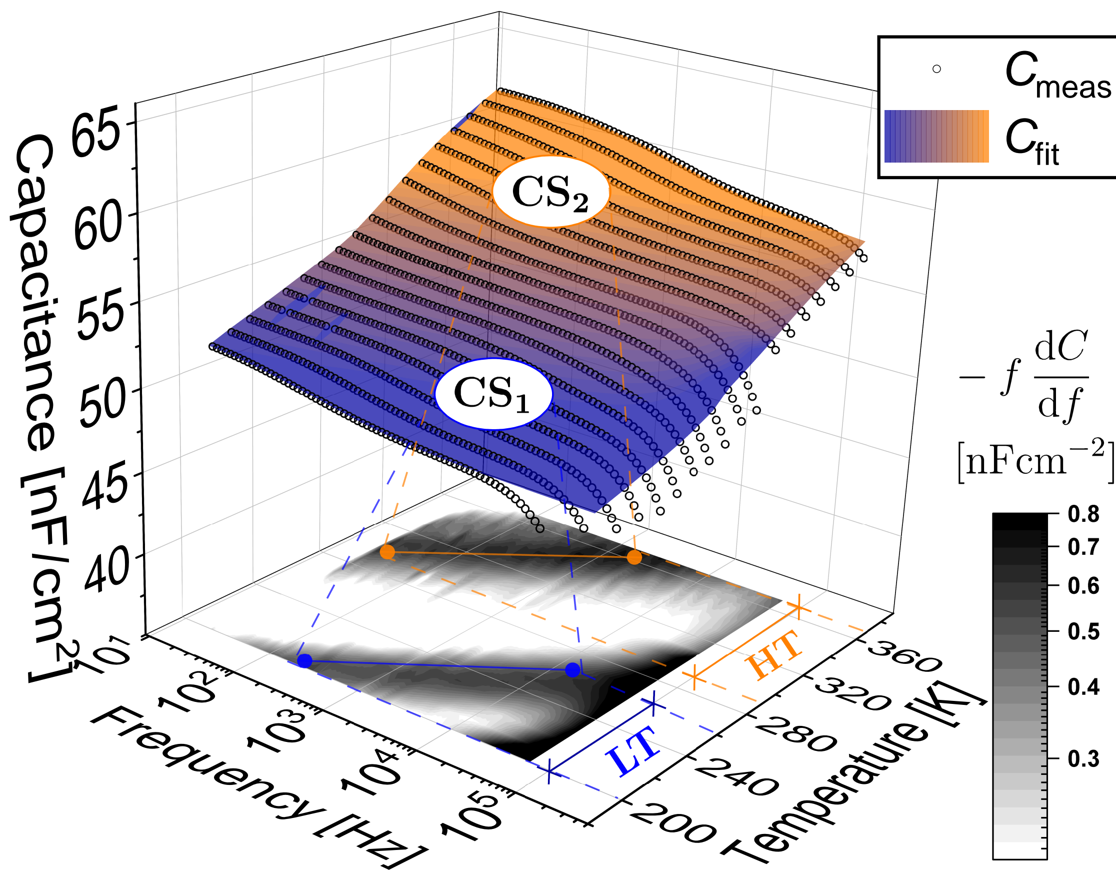

Figure 6.1 – C-f-T spectra of $In_{0.01}Ga_{0.99}As$ component cell irradiated with 3 MeV electron at a fluence of $5 \cdot 10^{15}$ cm^{-2}. Measured data points are represented by open circles, whereas the surface fit is obtained using Eq. 3.9. The surface color map distinguishes two distinct capacitance steps CS_1 (blue area) and CS_2 (orange area). On the f-T plane, the projection of the function -$f \cdot \mathrm{d}C/\mathrm{d}f$ is illustrated.

the capacitance value measured in the high frequency range, although this – as mentioned before – has limited accessibility due to resonance effects. Therefore, C_{SCR} should be included as a fitting parameter in Eq. 3.9. In addition, C_{SCR} is temperature-dependent due to the varying degree of ionization of the dopant atoms on both n- and p-type side of the junction. The temperature dependence is not a linear function over the wide temperature range investigated [56], thus leading potentially to an ambiguous fit. However, its value can be linearized separately in the temperature range LT and HT by using the expression $C_{\mathrm{SCR}}(T) = \alpha T + \beta$, with constants α and β for each temperature regime.
The fitting process is thus split in two separate routines for the LT and the HT regime, leading to the determination of two separate values of $C^{\mathrm{LT}}_{\mathrm{SCR}}(T)$ and $C^{\mathrm{HT}}_{\mathrm{SCR}}(T)$ and avoiding ambiguities arising from single-temperature capacitance data. The splitting of the fitting process allows further simplification in the single routines. The defect responsible for the CS_1 step in the LT regime is always activated in the HT regime, i.e., the f_{t} associated to CS_1 shifts out of the measurable frequency range in the HT regime according to Eqs. 3.1 and 3.7. For this reason, the concentration of the defect responsible for CS_1 can be lumped together with N_{a} in the value of $C^{\mathrm{HT}}_{\mathrm{SCR}}$. This approach is in line with the treatment of all the defects independently from one another, and requires less computational resources. By embracing this approach, it should be noted that the resulting $C^{\mathrm{HT}}_{\mathrm{SCR}}$ includes the contribution of the CS_1 defect concentration and N_{a}, whereas $C^{\mathrm{LT}}_{\mathrm{SCR}}$ is only due to N_{a}. In summary, the splitting of the fitting routine in the LT and HT range allows the temperature dependency of C_{SCR} to be linearized in the two regimes, thus leading to an unambiguous fit. Moreover, it improves the computational efficiency by reducing the number of defects required in Eq. 3.9 per each fitting routine.

6.3.2 Parameter fitting

The number of defects n included in each fitting routine is determined by the number of distinguishable peaks f_{t} found in the functional $-f\mathrm{d}C/\mathrm{d}f$: one single defect – labeled H1 – in the LT range, and three defects – labeled H2, H3 and H4 – in the HT range. The three defects in the HT range are not distinguishable in Fig. 6.1 because of the limitation in the resolution of the plot. The parameters to be determined are E'_{t_0}, N_{t_0}, σ_{p} and λ for each defect, as well as the coefficients α and β which determine $C^{\mathrm{LT,RT}}_{\mathrm{SCR}}(T)$ for the two temperature regimes. The fitting of the C-f-T surface is performed in three steps:

(i) The trap signature $f_{\mathrm{t}}(T)$ is fitted with the Arrhenius equation Eq. 3.7 and 3.1, yielding E'_{t_0} and an initial value of σ_{p}.

(ii) The initial values for α, β, N_{t_0} and λ are chosen manually according to their respective influences on the C-f curves.

(iii) The refined values for σ_{p}, N_{t_0} and λ, as well as the coefficients α and β are obtained with the help of the algorithm that minimize the residual function S_{rms}:

$$S_{\mathrm{rms}} = \sqrt{N^{-1}_{\mathrm{point}} \sum_{T} \sum_{f} \left(C_{\mathrm{meas}} - C_{\mathrm{fit}}\right)^2}, \tag{6.1}$$

where N_{point} is the number of useful data points.

The results of the fitting process for all cells, particle energies and fluences is summarized in Table 6.2. For $E'_{\mathrm{t_0}}$, the uncertainty range of the Arrhenius fit is indicated. The uncertainty associated with the remaining fitting parameters is obtained with a Monte Carlo approach [86], and represents the 95% confidence interval obtained over a set of 100 routines, where the starting values for each parameter is varied randomly in a range of two orders of magnitude with respect to the expected value. It is useful for the manual determination of the starting parameters in step (ii) to consider the contribution of each fitting parameter in the step-like shape of the C-f curve: $C_{\mathrm{SCR}}^{\mathrm{LT,HT}}$ is the baseline capacitance signal, which is easily accessible in the high-frequency range on the lower temperature curves for each regime. The linearization of $C_{\mathrm{SCR}}^{\mathrm{LT,HT}}(T)$ ensures coherent values also at the temperatures where the high-frequency capacitance is not accessible due to the aforementioned limitations. The steepness of the capacitance step is solely determined by the parameter λ in Eq. 3.9. The amplitude of the capacitance step is thus mainly determined by the parameter $N_{\mathrm{t_0}}$. The f_{t} position is determined by $E_{\mathrm{t_0}}$ and σ_{p} according to Eq. 3.7 with $N_{\mathrm{t_0}} \ll N_{\mathrm{a}}$. If $E_{\mathrm{t_0}}$ is fixed by the Arrhenius fit, the position of f_{t} is solely determined by σ_{p}. It should be mentioned that, as $E_{\mathrm{t_0}}$ is fixed for all the irradiated cells, a slight variation within the uncertainty of the energy level is compensated by a large variation of σ_{p} according to Eq. 3.1, thus explaining the high uncertainty of this parameter.
Taking into account the accuracy of the LCR meter and the uncertainty of the doping levels of the cells, a value of $N_{\mathrm{t_0}} \approx 8\times10^{13}\,\mathrm{cm}^{-2}$ represents the minimum concentration sensitivity, resulting in a detection factor $N_{\mathrm{t_0}}/N_{\mathrm{a}} \approx 2\times10^{-3}$. It has to be noted that $\mathrm{CS_1}$ and $\mathrm{CS_2}$, ascribed to the effect of irradiation-induced defects, have been checked against other possible causes, e.g., resistance effects, dielectric relaxation and hetero-interface barriers.
The effect of all defects on the cell capacitance is distributed over the entire f-T domain. It is possible to produce a single plot, which condenses all data of the two f-T domains in a unique curve, so that the effect of all the defects is visible at a glance. This can be achieved by plotting $-f\mathrm{d}C/\mathrm{d}f$ over a scaled frequency axis computed as $fT^2 f_{\mathrm{o}} \exp{(E_{\mathrm{f}}/kT)}$, where f_{o} is a constant and the value E_{f} is an exponential scaling factor, which equals the activation energy of H2 for the spectra in the HT temperature range and of H1 in the LT temperature range. The resulting plot is illustrated in Fig. 6.2 (a), and the single contributions of H2, H3 and H4 in the HT range can be differentiated in the low scaled-frequency range. In addition, the density of states in the $\mathrm{In_{0.01}Ga_{0.99}As}$ band gap extracted from the fitting process is depicted in Fig. 6.2 (b). In the following sections, the defect concentration data are used to study the correlation between the energy-dependent defect introduction rate and the particle NIELs.

Table 6.2 – Defect parameters resulting from the fitting routine of the $In_{0.01}Ga_{0.99}As$ component cell admittance spectra. The first column indicates the irradiation particle, energy (in MeV) and fluence (in cm^{-2}).

cell	H1 $E'_{t_0} = (0.29 \pm 0.03)$ eV			H2 $E'_{t_0} = (0.61 \pm 0.05)$ eV			H3 $E'_{t_0} = (0.68 \pm 0.03)$ eV			H4 $0.45\,\text{eV} < E'_{t_0} < 0.55\,\text{eV}$		
	N_{t_0} [cm^{-3}] $\times 10^{14}$	σ_p [cm^{-2}] $\times 10^{-16}$	λ [eV] $\times 10^{-3}$	N_{t_0} [cm^{-3}] $\times 10^{14}$	σ_p [cm^{-2}] $\times 10^{-16}$	λ [eV] $\times 10^{-3}$	N_{t_0} [cm^{-3}] $\times 10^{14}$	σ_p [cm^{-2}] $\times 10^{-16}$	λ [eV] $\times 10^{-3}$	N_{t_0} [cm^{-3}] $\times 10^{14}$	σ_p [cm^{-2}] $\times 10^{-16}$	λ [eV] $\times 10^{-3}$
e.5 1.4×10^{16}	0.8 ± 0.3	2 ± 1.4	20 ± 9	–	–	–	–	–	–	–	–	–
e1 1×10^{15}	1.5 ± 0.6	4.7 ± 3.4	33 ± 15	–	–	–	–	–	–	–	–	–
e1 3×10^{15}	5.8 ± 1.6	3.4 ± 2.5	14 ± 7.4	0.6 ± 0.4	40 ± 28	19 ± 19	2.5 ± 0.7	20 ± 30	36 ± 38	0.5 ± 0.3	40	78 ± 61
e1 5×10^{15}	9.1 ± 1.6	4.5 ± 2.5	25 ± 7	0.9 ± 0.5	109 ± 80	10 ± 10	3.9 ± 0.6	80 ± 60	46 ± 24	0.7 ± 0.2	109	33 ± 17
e1 1×10^{16}	16 ± 3	3.7 ± 1.6	18 ± 3	1.7 ± 0.3	104 ± 44	11 ± 3	6.9 ± 1.2	83 ± 35	35 ± 6	1.8 ± 0.4	104	50 ± 10
e1 2×10^{16}	33 ± 6	3.5 ± 1.4	17 ± 3	4.8 ± 0.8	82 ± 45	12 ± 4	11 ± 2	77 ± 42	26 ± 5	3 ± 0.5	82	49 ± 8
e3 2×10^{15}	10 ± 3	4 ± 1.7	34 ± 6	4 ± 0.5	67 ± 28	29 ± 5	2.8 ± 0.6	45 ± 19	26 ± 4	2 ± 0.2	67	40 ± 10
e3 5×10^{15}	25 ± 3	4.7 ± 1.5	32 ± 5	12 ± 1.4	72 ± 30	36 ± 5	5.7 ± 0.7	57 ± 24	31 ± 5	6 ± 0.7	72	40 ± 3
e3 1×10^{16}	58 ± 5	3.4 ± 0.9	14 ± 4	28 ± 3.3	76 ± 16	35 ± 3	10 ± 1.3	57 ± 12	31 ± 3	10 ± 1.2	76	40 ± 4
p1 8×10^{11}	3.6 ± 1.3	4.9 ± 3.6	45 ± 8	–	–	–	–	–	–	–	–	–
p1 1×10^{12}	4.6 ± 1.3	4.9 ± 3.6	41 ± 8	3 ± 0.8	191 ± 111	44 ± 6	1.5 ± 0.4	54 ± 39	47 ± 6	2.5 ± 0.7	191	50 ± 6
p1 3×10^{12}	9.5 ± 2	3.9 ± 1.6	26 ± 8	12 ± 2.3	221 ± 93	49 ± 7	3.3 ± 0.6	50 ± 21	46 ± 6	7 ± 1.3	221	40 ± 5
p1 1×10^{13}	34 ± 3.6	3.2 ± 1	39 ± 8	45 ± 2.2	224 ± 51	65 ± 8	5.4 ± 0.6	25 ± 21	35 ± 6	16 ± 0.7	224	30 ± 4
p2 2×10^{12}	–	–	–	3.5 ± 0.7	138 ± 51	70 ± 10	0.2 ± 0.2	125 ± 55	26 ± 4	1.9 ± 0.3	138	84 ± 25
p1 5×10^{12}	10 ± 6.9	4 ± 2.5	61 ± 8	9.7 ± 0.3	147 ± 68	71 ± 10	0.6 ± 0.5	14 ± 10	36 ± 20	4 ± 1.3	147	40 ± 25

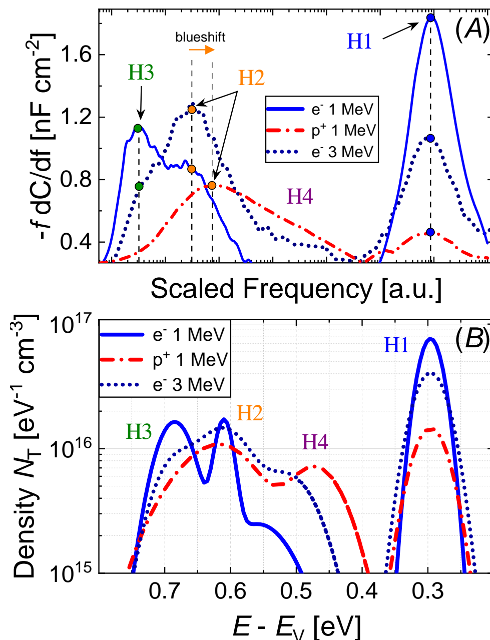

Figure 6.2 – (a) Scaled admittance signal -$f\mathrm{d}C/\mathrm{d}f$ and (b) combined density of states in the band gap of p-type $In_{0.01}Ga_{0.99}As$ component cells irradiated with a similar amount of $\mathrm{DDD}_{21\mathrm{eV}}$ introduced by 1 and 3 MeV electrons and 1 MeV protons.

6.4 NIEL Defect Analysis

6.4.1 Recoil contribution

For purposes which will come clear in the following, we shall now define the contribution of each recoil energy in the total NIEL. The NIEL_0 contribution factor $\chi(E)$, defined as:

$$\chi(E) = \frac{\int_{E_{\mathrm{d}_0}}^{E} E_{\mathrm{R}}\, L\, \frac{\partial \sigma_{\mathrm{Cs}}}{\partial E_{\mathrm{R}}} \mathrm{d}E_{\mathrm{R}}}{\int_{E_{\mathrm{d}_0}}^{E_{\max}} E_{\mathrm{R}}\, L\, \frac{\partial \sigma_{\mathrm{Cs}}}{\partial E_{\mathrm{R}}} \mathrm{d}E_{\mathrm{R}}}, \tag{6.2}$$

quantifies the NIEL_0 contribution of the recoil spectrum from E_{d_0} (physical threshold energy) up to the energy E. From the plots of the $\chi(E)$ factor, reported as a percentage in Fig. 6.3, it is possible to identify the effective recoil spectrum which deposits the DDD for each irradiating particle. For instance, 80% of the damage caused by 1 MeV electrons is due to recoils with energy below 40 eV. The same recoil spectrum accounts for only 40% of the damage in the 3 MeV electron case, and only for 10% of the damage in the 1 MeV proton case. The recoil spectrum triggered by the irradiating particle has several implications on the formation of the defects within the lattice. Recoils with energy just above E_{d_0} can only create one or no additional displacement. Therefore, the displacements produced by 1 MeV electrons, which can trigger recoils up to few tens of eV, are generated in a region of the lattice not populated by many other neighboring point defects. The displaced atoms are most likely isolated – i.e., they do not interact with other closely spaced lattice imperfections. In the proton case, on the other hand, recoils with much higher energy have a large contribution in the NIEL_0. A high-energy recoil can trigger a long-range displacement cascade resulting in the formation of highly-damaged

regions [27] where closely-spaced point defects interact and form stable clusters. The size of these clusters can extend up to several GaAs lattice constants [25].

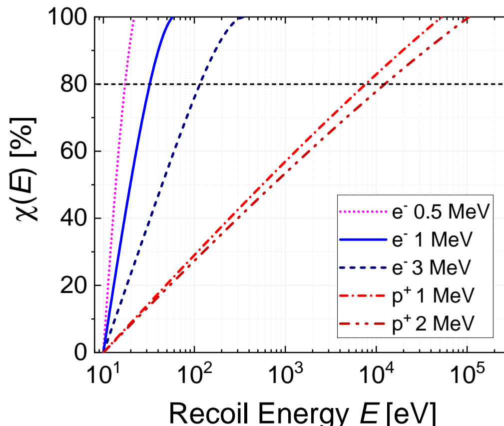

Figure 6.3 – Relative NIEL contribution $\chi(E)$ originating from recoils with energies below E for 0.5, 1 and 3 MeV electrons and 1 and 2 MeV protons in $In_{0.01}Ga_{0.99}As$. The value $\chi(E)$ indicated the contribution, expressed in percentage, of recoils with $E_R < E$.

6.4.2 Fitting of the Defect E_d

The admittance measurements yield individual defect concentrations N_{t_0} and introduction rates $k_t = N_{t_0}/\Phi$ as a function of different particle energies. Therefore, it is a straightforward approach to see whether they can be collapsed onto a single linear characteristic:

$$\begin{aligned} N_{t_0} &= \alpha_k \times \mathrm{DDD}\,; \\ \alpha_k &= \frac{k_t}{\mathrm{NIEL}}, \end{aligned} \tag{6.3}$$

in analogy to what has been done for the PV parameter degradation in Section 4. This implies that k_t is proportional to the deposited particle NIEL in the material with α_k as the scaling constant which allows the experimental k_t data to fall on the NIEL curve. According to Eq. 6.3, α_k is physically interpreted as the defect introduction rate referred to displacement dose introduced by electrons (eDIR) and protons (pDIR). We will refer to the α_k constants as eDIR and pDIR.
As shown in the following, the experimental data fall onto a single straight line if an adapted E_d in the electron case is used. The resulting value E_d is the defect threshold energy and it can be directly related to the physical defect configuration. It represents the minimum recoil energy whose displacements contribute effectively to the final defect structure. When E_d approaches the threshold energy for Ga and As displacement E_{d_0}, the defect unit cell is made up of a single-displacement structure, i.e., a simple Frenkel pairs. When $E_d > E_{d_0}$, on the other hand, the defect unit cell is composed of a more complex structure, such as defects with higher formation energy (e.g., antisites) or multi-displacement defects (e.g., divacancies). The fitting of E_d for a given defect such that the defect introduction rates fall on the same NIEL

curve for all electron energies is therefore a way to draw conclusions on the physical defect configuration in the lattice directly from admittance measurements. Only the electron data are used for this procedure due to the higher sensitivity of the electron NIEL to E_d compared to the proton NIEL in the energy range of interest. It has to be noted that the NIEL is based on a purely analytical calculation. The adapted threshold energy for the defect in question is a way to achieve the correct energy scaling with regard to the introduction rate of different particles. No conclusion on relative contributions of other defects in the displacement damage can be drawn from this fitting alone. When eDIR and pDIR are different, the different particle effectiveness is accounted for by the factor $\mathrm{R}^\mathrm{d}_\mathrm{ep} = \mathrm{pDIR/eDIR}$, defined in analogy to the electrical R_ep. The defect $\mathrm{R}^\mathrm{d}_\mathrm{ep}$ allows D_e to be scaled so that the N_{t_0}-D_e plot falls onto the N_{t_0}-D_p plot.
While a similar approach has also been followed in the past for the solar cell PV parameters, any conclusions in this case were hampered by the fact that only the combined behavior of all defects, weighted by their electrical effectiveness, could be studied. Finally, it has to be noted that since the cells were irradiated at 300 K and all measurements were performed after 370 K annealing, an annealed defect configuration was probed in all cases. Therefore, the defect E_d has a physical meaning only if the annealing dynamics at the maximum temperature experienced by the solar cell are negligible.

6.5 Irradiation-induced defects

H1

The capacitance step CS_1 is characterized by a clear, distinguishable, single peak in the -$f\mathrm{d}C/\mathrm{d}f$ functional, thus allowing an easy determination of $f_\mathrm{t}(T)$. By making use of Eq. 3.7, the energy level associated with the defect, labeled H1, is found: $E'_{\mathrm{t}_0} = 0.29\,\mathrm{eV}$. The fitting of H1 introduction rates with the electron NIEL yields $E_\mathrm{d} = 21\,\mathrm{eV}$, which suggests that the defect is either formed by isolated antisites [87] or a different double-displacement defect. A similar energy level in irradiated p-type GaAs has been already reported in literature [48, 88]. The N_{t_0}-DDD and the introduction rate plots are reported in Fig. 6.4 (a) and (b). In Fig. 6.4 (b), the NIELs computed with different E_d values are superimposed in order to illustrate the sensitivity of the E_d fitting process.
eDIR and pDIR coefficients of 1.4×10^4 and $7.1\times10^3\,\mathrm{g\,cm^{-3}\,MeV^{-1}}$ result, respectively, thus yielding $\mathrm{R}^\mathrm{d}_\mathrm{ep} = 0.5$. The electron dose D_e is twice as effective as the corresponding proton D_p in producing H1.

H2 and H3

The capacitance step CS_2 for electron-irradiated cells is characterized by the presence of two overlapping peaks in the -$f\mathrm{d}f/\mathrm{d}C$ functional, which are attributed to two separate irradiation-induced defects, H2 and H3. The contributions of H2 and H3 are de-coupled by performing a Gaussian de-convolution on the -$f\mathrm{d}f/\mathrm{d}C$ data. In this way, the single $f_\mathrm{t}(T)$ are extracted and fitted with Eq. 3.7, leading to two energy

levels $E'_{t_0} = 0.61$ eV and $E'_{t_0} = 0.68$ eV for H2 and H3, respectively. In the proton case, on the other hand, the peak associated with H3 is only detectable in the higher fluence cases. The NIEL analysis on the electron data yields E_d values for H2 and H3 of 38 eV and 9 eV respectively. These values might be affected by high uncertainty, however, due to lack of data for electron energies below 1 MeV. The low E_d value for H3 suggests that it can be ascribed to a single-displacement defect, i.e., a Frenkel pair. On the other hand, H2 can be ascribed to a more complex defect structure. The energy level of H2 has been associated in the literature to the double donor [++/+] configuration of the EL2 defect [41, 79], possibly due to As antisites (As_{Ga}).
The N_{t_0}-DDD plots are reported in Fig. 6.4 (c), whereas the eDIR and R^d_{ep} factor are reported in Fig. 6.4 (d). The defect H3 exhibits an $R^d_{ep} = 0.38$, whereas $R_{ep} = 1$ is found for H2. A begin-of-life H3 concentration of about $(9 \pm 2) \times 10^{13}$ cm^{-3} is obtained in the linear fit of both the N_{t_0}-D_e and N_{t_0}-D_p plots. This indicated that H3 may be present in the material already prior to irradiation.

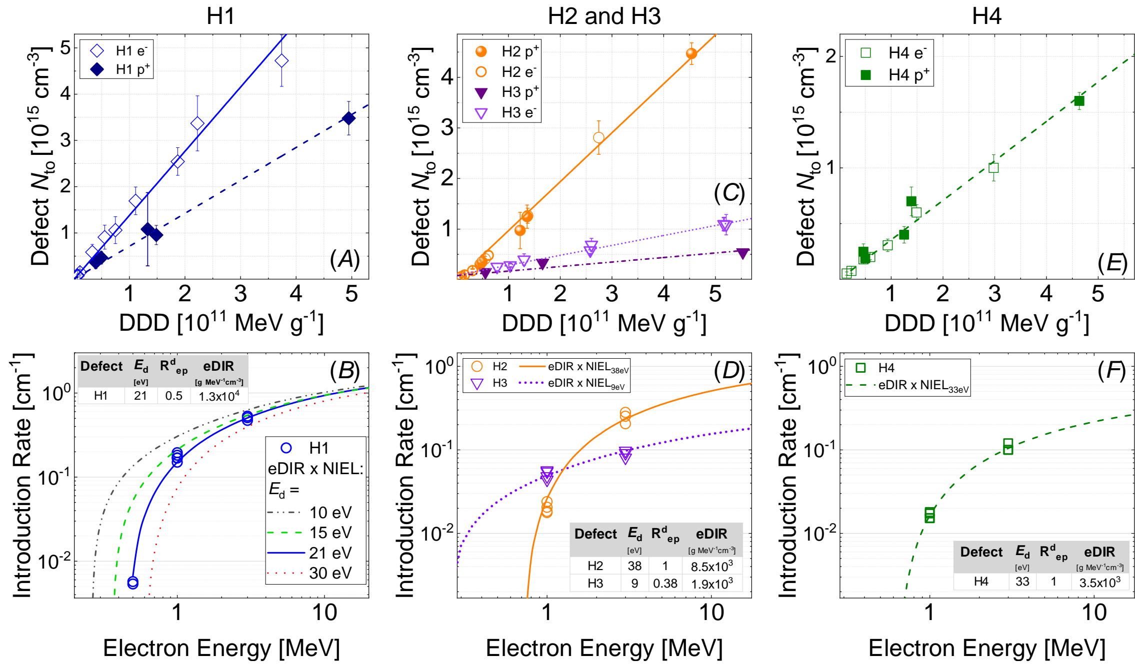

Figure 6.4 – Defect concentration as a function of adapted DDD and introduction rate as a function of particle energy for (a,b) H1, (c,d) H2 and H3, and (e,f) H4 in p-type $In_{0.01}Ga_{0.99}As$ component cells. The adapted DDD for each defect is computed by using the appropriate E_d values, reported in the insets in (b), (d) and (f).

H4

A small shoulder characterizes the H2 peak, as visible in Fig. 6.2 (a) for the proton and 3 MeV electron cases. This capacitance contribution is attributed to the deep level H4. Since only a featureless peak is detected in the -$f\mathrm{d}C/\mathrm{d}f$ plots, it is not possible to determine the trap $f_t(T)$. The H4 contribution is included in the admittance model by using the same value for σ_p as determined for H2. In this way,

the fitting routine yields the apparent H4 energy level, which shows variations in the range $0.45\,\text{eV} < E^*_{\text{t}_\text{o}} < 0.55\,\text{eV}$ for the different samples analyzed. The NIEL analysis yields a value of $E_\text{d} = 33\,\text{eV}$ and $\text{R}^\text{d}_\text{ep} = 1$. Also in this case, the value of E_d suffers of uncertanty due to the lack of electron data below 1 MeV.

6.6 Discussion

6.6.1 Effective defect NIEL*

With the knowledge of the absolute number of defects generated and the associated defect energy E_d, the total displacement damage can be calculated for each irradiating particle type and energy. The actual NIEL introduced, denoted as NIEL*, can be computed by taking into account each single defect introduction rate with the associated threshold energy:

$$\text{NIEL}^* = \rho^{-1} \sum_{i=1}^{n} (k_\text{t} \times E_\text{d})_i \,, \tag{6.4}$$

where ρ is the material density and n is the total number of type of defects introduced into the material; in this case, $n = 4$. The results for H1-H4 are reported in Fig. 6.5. The theoretical NIEL curves, computed using $E_{\text{d}_0} = 13\,\text{eV}$ (NIEL_0) and 21 eV, are also superimposed. The measured NIEL* values deviate from the theoretical NIEL

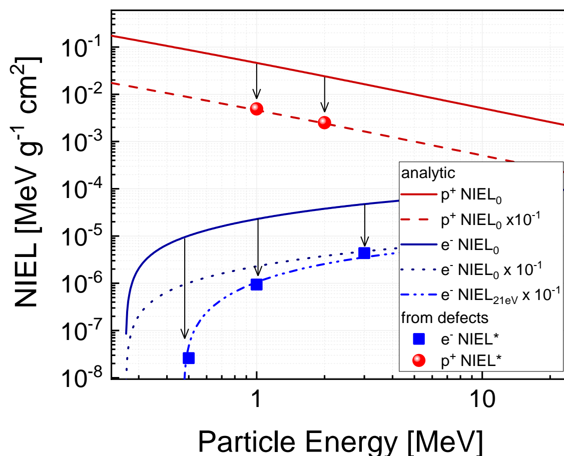

Figure 6.5 – Measured (data points) effective NIEL* in proton and electron irradiated p-type $\text{In}_{0.01}\text{Ga}_{0.99}\text{As}$ computed from defect introduction rates with Eq. 6.2. The theoretical NIEL (solid curves) with different threshold energies and superimposed to the plot.

with $E_\text{d} = 21\,\text{eV}$ by a factor of 10. The missing NIEL* contribution responsible for this gap is expected to arise from defects that cannot be accessed via admittance spectroscopy in p-type samples, i.e., electron traps, defects located below E_{F_p} or defects whose energy level does not lie in the forbidden band gap. A complementary analysis on at least the electron traps located in the upper half of the band gap is required to arrive to a complete estimation of the NIEL*. By considering only the introduction rates of the electron traps E1-E5 detected in irradiated n-type GaAs cells (1 MeV e^- data from Pons *et al.* [89]), an approximated NIEL* close to NIEL_0

can be estimated. It has been demonstrated in the past that these traps are also introduced in p-type GaAs [79]. Therefore, assuming comparable introduction rates of E1-E5 for n- and p-type material, the bulk of the gap between NIEL* and the analytical NIEL is due to the missing contribution of E1-E5 in Eq. 6.4.
Furthermore, it should be mentioned that the calculated NIEL value accounts for the non-ionizing energy deposited by irradiating the material at 0 K. It has been already recognized that the theoretical NIEL is not necessarily proportional to the total number of defects formed after irradiation [27] because of non-linear processes taking place in the lattice, e.g., the formation of clustered regions and the defect annihilation during both the irradiation experiment and the post annealing treatment [90]. Although a general conclusion cannot be drawn based solely on the data available from this analysis, it is remarkable how the NIEL* relative to H1-H4 falls on an attenuated NIEL $\times 10^{-1}$ curve computed with $E_\mathrm{d} = 21\,\mathrm{eV}$, as shown in Fig. 6.5. Despite the fact that the H1 defect with $E_\mathrm{d} = 21\,\mathrm{eV}$ is the most prevalent defect, this E_d value is thus not representative of any particular defect structure, but rather an empirical value with which it is possible to describe the introduction of the effective NIEL* in p-type $In_{0.01}Ga_{0.99}As$ in the form of stable defects H1-H4. It follows that the reference NIEL calculated with $E_\mathrm{d} = 21\,\mathrm{eV}$ can be used to compare a similar level of damage in terms of H1-H4 defects for cells irradiated with different particles and energies. Since no cell electrical parameters were involved in this derivation, it can be further concluded that this threshold energy is a GaAs material-specific parameter, independent of the detailed electrical device design.

6.6.2 Relative defect introduction

Incident particles, depending on their mass and energy, can trigger a vastly different recoil spectrum, as shown in Fig. 6.3. An obvious question is whether this affects the relative introduction probability of different defects. To address this topic further, a DDD of $2 \times 10^{11}\,\mathrm{MeV\,g^{-1}}$ is chosen. With the help of a NIEL with 21 eV, the required fluence of 1 and 3 MeV electrons as well as 1 MeV protons is calculated and the associated number of defects introduced is extracted from Table 6.2 with the help of a linear fit. The use of a $E_\mathrm{d} = 21\,\mathrm{eV}$ is essential for this comparison, since only this threshold energy correctly quantifies the relative contribution of the H1-H4 defects in the overall displacement damage, as previously discussed. The absolute and relative defect concentrations are reported in the pie charts in Fig. 6.6.
The recoil spectrum triggered by the particles has a significant role in defining the relative concentration of the individual defects. As the energetic content of the recoil spectrum increases, it is more likely that defects with high E_d – such as H2 and H4 – are generated, and defects with lower E_d – such as H1 and H3 – account for a smaller fraction of the total damage.

6.6.3 Macroscopic parameter degradation

Due to the different electronic parameters found in H1-H4, a different damaging effectiveness with respect to the solar cell macroscopic electrical parameters is expected. The ultimate cause of a solar cell electrical parameter degradation is the

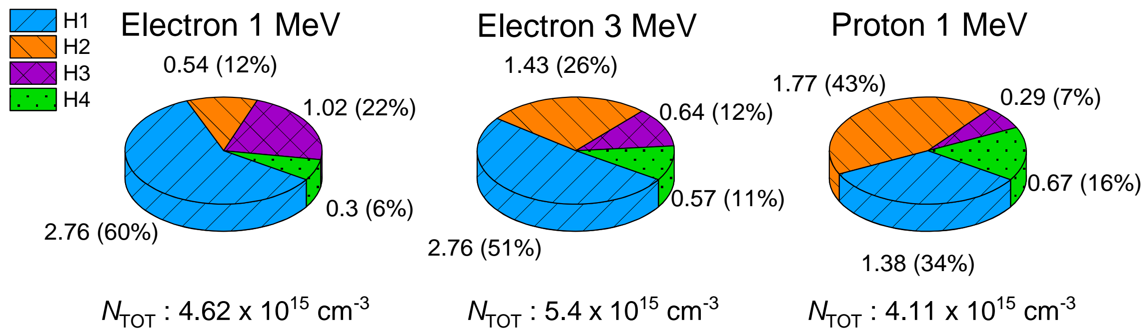

Figure 6.6 – Absolute N_{t_0} (in units of $10^{15}\,\mathrm{cm}^{-3}$) and relative ($N_{t_0}/N_{\mathrm{TOT}}$) defect concentration generated by the same amount of DDD(21 eV) $= 2 \times 10^{11}$ MeV g^{-1} introduced by 1 and 3 MeV electrons and 1 MeV protons in p-type $\mathrm{In_{0.01}Ga_{0.99}As}$ component cells. The total sum of the defects N_{TOT} is also reported for each case.

reduction of the carrier lifetime $\tau_{\mathrm{n,p}}$ within the solar cell neutral (J_{SC}) and depleted regions (V_{OC} and J_{02}), which is related to the defect parameters by $\tau_{\mathrm{n,p}}^{-1} \propto \sigma_{\mathrm{n,p}} v_{\mathrm{th}} N_{t_0}$. If the electronic structure of the defect does not depend on the type and energy of the irradiating particle, its capture properties $\sigma_{\mathrm{n,p}}$ are well defined and identical in the different irradiated cells. As a result, the degradation due to this class of defects occurs due to an increase of N_{t_0} as more displacements occur within the semiconductor. The damaging effectiveness of each defect on the solar cell J_{SC}, J_{02} and V_{OC} can thus be estimated by means of correlation coefficients r resulting from the Pearson analysis between the parameter remaining factors and the defect N_{t_0}. When r approaches +1 (-1), a significant positive (negative) correlation between the parameters is found. The Pearson's r coefficients for H1-H4 defects are reported in the color map of Fig. 6.7. Moreover, the Pearson analysis is extended to the DDD computed with $E_{\mathrm{d}} = 21$ eV ($D_{21\mathrm{eV}}$), which is representative of the actual scaling of the relative abundance of the defects H1-H4 with particle energy, as discussed earlier.

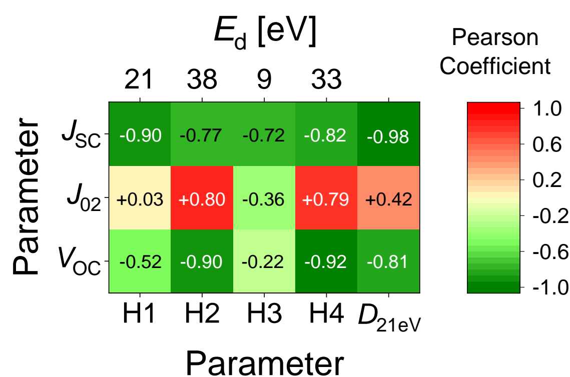

Figure 6.7 – Pearson's r correlation coefficients of the H1, H2, H3, H4 defect concentration and the DDD computed with $E_{\mathrm{d}} = 21$ eV ($D_{21\mathrm{eV}}$) over the solar cell J_{SC}, J_{02} and V_{OC} remaining factors. A value of -1 expresses a good correlation for J_{SC} and V_{OC}, whereas +1 expresses a good correlation for J_{02}.

All defects exhibit a negative correlation with J_{SC} and therefore, they are all damaging J_{SC} to a certain extent. The good correlation of the J_{SC} degradation with $D_{21\mathrm{eV}}$

(r = -0.98) indicates that it is likely that H1-H4 are the main defects responsible for the J_{SC} damage. These results are fully in line with the J_{SC} fit in Fig. 4.3. The total number of defects H1-H4 introduced by particles of different energies varies by a factor of 1.3 at most for the same amount of D_{21eV}, according to the findings shown in Fig. 6.6. Thus the good correlation of J_{SC} with D_{21eV} can also be interpreted in terms of a good correlation to the sum of the defects. From this it can be concluded that the minority carrier capture cross sections of H1-H4 are in a similar range and cannot differ by orders of magnitude.
On the other hand, V_{OC} and J_{02} are mostly damaged by the recombination centers H2 and H4. The defect H1 has a negligible effect on J_{02}, which can be attributed to its asymmetrical position within the band gap, combined with a low σ_p. Despite its apparent deep position in the band gap, the defect H3 does not affect V_{OC} and J_{02}. Hence, it is possible that the defect presents a strong capture asymmetry resulting in a low minority-carrier capture cross section, or most likely, the energy level extracted from the trap signature is overestimated by the substantial effect of a temperature-dependent $\sigma_p(T)$. The latter theory is supported by experimental observations on some deep levels in III-V materials [91], and also by some capture theories [23].
According to Fig. 6.6, particles with higher relativistic mass are expected to damage V_{OC} and J_{02} more for a similar amount of 21 eV NIEL introduced in the cell, because these create a higher contribution of H2 and H4 defects. The best fit of the electron J_{02} data with $E_d = 35$ eV, as shown in Fig. 5.2 (c), is thus in line with the E_d values found for H2 and H4. These defects cannot be formed by 0.5 MeV electrons, whose maximum energy transferable to a Ga or As atom is ~ 23 eV. The only defects that a 0.5 MeV electron can introduce in $In_{0.01}Ga_{0.99}As$ cells are H1 and H3, which exhibit a very low correlation coefficient with J_{02} according to the Pearson map in Fig. 6.7. The J_{02} degradation observed for 0.5 MeV electrons, shown in Fig. 5.2 (c), can be only reconciled by postulating another recombination center characterized by $E_d < 23$ eV. This defect may be energetically located in the upper half of the band gap, out of the detectable range of admittance spectroscopy.

6.6.4 Proton-electron equivalence factors

Although the Pearson analysis yields a good correlation with $r = 0.8$ and 0.79 between the degradation of J_{02} and the concentration of the H2 and H4 defects, when these mid-gap defects are introduced by protons, the damage to J_{02} is more pronounced compared to the equivalent electron case, as shown in Fig. 5.2 (c) where the choice of $E_d = 35$ eV allows a fair comparison of H2-H4 defect introduction. A plausible explanation may be the presence of defects out of the detectable range with a different introduction rate for protons and electrons. Another possible reason could be ascribed to a different capture capability of the same mid-gap defects introduced by protons and electrons. The latter explanation can be rationalized to a certain degree with the help of the admittance spectroscopy results. Analyzing the H2 defect, the distribution width λ^{H2} is found to be not related to the DDD, but rather to the distribution of recoil energies. Using an 80% cutoff in the relative NIEL contribution plot in Fig. 6.3, the energy $E_{80\%}$ is determined. It represents the recoil

energy up to which 80% of the total displacement damage of the incident particle is deposited. As illustrated in Fig. 6.8 (a), a clear correlation is found between $E_{80\,\%}$ and λ^{H2}.

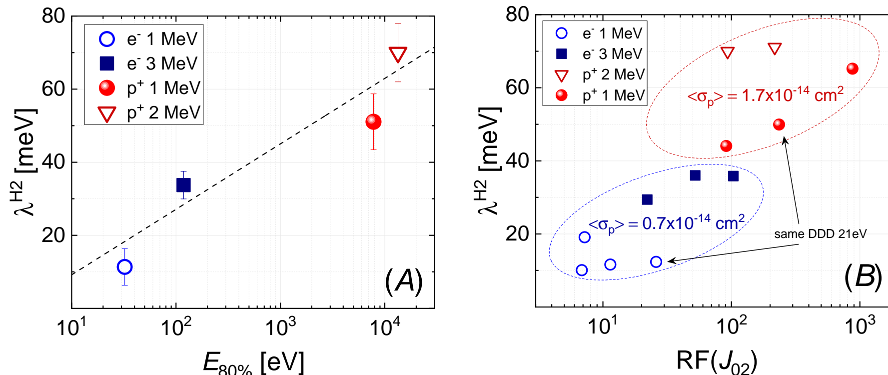

Figure 6.8 – (a) H2 distribution width λ^{H2} as a function of the recoil spectrum $E_{80\%}$ triggered by electrons and protons, obtained as the energy value at which $\chi(E) = 80\%$, and (b) λ^{H2} as a function of the J_{02} remaining factor in irradiated $\mathrm{In_{0.01}Ga_{0.99}As}$ component cells. The average capture cross-section $<\sigma_{\mathrm{p}}>$ for the proton- and electron-induced H2 defect is also reported. Arrows indicate two data points corresponding to a similar level of DDD introduced by protons and electrons, computed in GaAs with $E_{\mathrm{d}} = 21\,\mathrm{eV}$.

This is rationalized considering that higher $E_{80\%}$ values imply larger clusters of defects. The higher electronic disorder of these regions leads to a wide distribution of available energy levels within the band gap, as already observed in literature via DLTS in GaAs cells irradiated with neutrons [92, 93] and protons [94]. Irradiated cells with higher λ^{H2} also exhibit a higher J_{02} remaining factor, as shown in Fig. 6.8 (b). This suggests that the larger band-tails around H2 may be linked to an increased capture capability of the defect in the SCR, thus affecting its damaging effectiveness with respect to J_{02}. In the limit of the uncertainty associated with the fitting of the admittance data, a higher σ_{p} is also observed for proton-irradiated cells compared to the electron case, which causes a slight blueshift of the H2 peak in the $-f\mathrm{d}C/\mathrm{d}f$ plot of Fig. 6.2 (a). This shows how a different particle recoil spectrum can impact the damaging effectiveness of a defect with respect to J_{02}. Although it might not be the only reason, this phenomenon can be linked to the existence of the electrical $\mathrm{R_{ep}}$ factor found for J_{02}. In the V_{OC} case, the existence of the $\mathrm{R_{ep}}$ factor is a direct consequence of the fact that for a moderately high dose level, the V_{OC} is dominated by J_{02}.

6.7 Conclusion

Temperature-dependent admittance spectroscopy was applied to the study of proton and electron radiation damage in $\mathrm{In_{0.01}Ga_{0.99}As}$ component solar cells. With the help of a dedicated fitting routine, four majority carrier defects labeled H1-H4 were identified in the p-type absorber. The key benefit of admittance spectroscopy in contrast to analyzing macroscopic cell performance parameters is the fact that the radiation effects can be analyzed one step closer to the actual physical defect pro-

cesses. The results depend to a lesser degree on the detailed electrical device design and thus can be interpreted more easily in terms of material-specific properties.
In particular the combination of admittance spectroscopy with the NIEL fitting of the defect introduction rate was shown to result in a unique threshold energy for each of the defects, which provides additional insight into their crystallographic configuration. Moreover, it was established that a NIEL with a threshold energy of 21 eV accurately describes the scaling of the relative abundance of H1-H4 with the energy of the incident particle. For a given DDD, the relative fraction of high-energy defect increases with the relativistic mass of the incident particle.
A Pearson analysis was then used to link these results on a defect level to the degradation of the macroscopic cell parameters. The J_{SC} degradation shows a direct correlation with the combined H1-H4 DDD, analytically described by a threshold energy of 21 eV, from which a similar damaging effectiveness of each individual H1-H4 defect on J_{SC} can be concluded. For J_{02}, and thus also for V_{OC} at high doses, the energy level of the defect in the band gap is important. Therefore, H2 and H4 play a major role for these parameters. This explains the fact that a threshold energy of 35 eV describes the DDD dependence of J_{02} very well, except for low-energy electrons. In addition, H2 was found to be more damaging if introduced by protons than by electrons. This behavior was traced back to a broader distribution of the H2 density of states in the band gap in the proton case. It is in line with the existence of an R_{ep} factor for J_{02} and V_{OC} that corrects for the less damaging nature of electron DDD as compared to proton DDD.

Chapter 7

Deep-level Transient Spectroscopy on GaAs Mesa-diodes

7.1 Introduction

The admittance spectroscopy analysis on $In_{0.01}Ga_{0.99}As$ component cells presented in the previous chapter is limited by the temperature-frequency constraints due to a device structure (2 cm × 2 cm component cells) not optimized for capacitance measurements. Moreover, only hole traps in the lower half of the absorber band gap were probed, which do not cover the entire defect energy level spectrum possibly introduced by irradiation. In this section, majority carrier traps are sampled in p- and n-type GaAs material by using DLTS on the mesa-diode structures described in Section 3.2[i]. The results are correlated with the displacement damage analysis in $In_{0.01}Ga_{0.99}As$ component cells reported in Chapter 6. It should be pointed out that the defect analysis in $In_{0.01}Ga_{0.99}As$ component cells and GaAs mesa-diodes is not directly comparable for several reasons:

- The epitaxial growth conditions of GaAs mesa-diodes on GaAs substrate and of $In_{0.01}Ga_{0.99}As$ component cells on Ge substrate is different;
- The In concentration in component cells may affect defect formation and local lattice environment;
- The devices have a slightly different band gap and doping concentrations, therefore a scattering of the trap energy levels is expected due to different electric fields [95];
- The devices are exposed to different type and duration of annealing conditions before defect spectroscopy analysis;

Moreover, other factors not related to the device structure need to be considered as well:

- The electron irradiation of the devices are performed at different facilities, with different irradiation conditions and dosimetry techniques;

[i] Part of the content of this section is subject of a following scientific publication

- The $In_{0.01}Ga_{0.99}As$ cells are analyzed by means of AS whereas GaAs mesa-diodes by means of DLTS. AS and DLTS have different sensitivity within the SCR: AS probes the trap emissions at a specific location where $E_t = E_F$ and the emission rate resonates with the ac bias frequency; DLTS, on the other hand, probes the trap emission in a much wider portion of the SCR defined by the filling pulse width, and thus the emission rate of the traps across the SCR may be weighted by the varying electric field magnitude.

7.2 Experimental details

GaAs mesa-diodes of both absorber polarity, as in Fig. 3.3 (b), were used in this study. In both cases, the nominal dopant concentrations were $10^{17}\,\mathrm{cm^{-3}}$ and $10^{18}\,\mathrm{cm^{-3}}$ for the low- and high-doped layer, respectively. The relevant GaAs material parameters were taken from literature data [84]. The mesa-diodes were irradiated with electrons ranging from 0.35 MeV to 1 MeV at the Sirius facility, and with 1 MeV protons at the CSNSM facility. The irradiation history of the samples is reported in Table 7.1. The irradiation fluence for the electron experiments in the energy range 0.5-2 MeV were chosen to introduce a similar amount of DDD in GaAs calculated with Eq. 2.22, with the NIEL computed as shown in Section 2.2.4 with $E_d = 21$ eV. The mesa-diodes have been kept at room temperature after irradiation. Only majority-carrier DLTS measurements up to a temperature of 300 K were performed, in order to prevent post-irradiation defect reordering. The samples were characterized with DLTS before and after irradiation and after a thermal annealing stage. During the annealing stage, samples were placed on metal plate and were heated up to 333.15 K for 48 h. Temperature and annealing time were taken from relative space standards [22], although no photon annealing was possible for mesa-diodes. During the annealing stage, defect reordering effects are expected as described in Section 2.2.2.
The DLTS measurements were acquired by using a quiescent reverse bias of $V_R = -1$ V, corresponding to a SCR width of 0.17 μm and 0.18 μm for n- and p-samples, respectively. A majority pulse voltage of $V_P = 0$ V was applied, implying a probed SCR slice of ∼50 nm in both cases. The DLTS measurements are illustrated in form of spectra of the measured signal S (Eq. 3.15) normalized by the depletion layer capacitance C_{SCR}, as a function of the device temperature.

Particle	Energy [MeV]	Fluence [$10^{15}\,\mathrm{cm^{-2}}$]	DDD_{21eV} [10^{10} MeV g^{-1}]
e^-	0.35	15	–
e^-	0.5	34	1.7
e^-	0.6	6.6	1.7
e^-	0.75	2.9	1.7
e^-	1	1.5	1.7
e^-	2	0.62	1.7
p^+	1	0.001	5

Table 7.1 – Irradiation history of GaAs mesa-diodes. The fluence values for electron irradiation in the 0.5-2 MeV range have been chosen to introduce a similar amount of DDD_{21eV} in GaAs.

7.3 Data analysis

The apparent position of the energy level E'_t are extracted by fitting of the trap Arrhenius plots with Eq. 3.17. The trap energy level is compared to calculated values of native defects in GaAs via ab-initio simulations [41, 42]. As the literature values differ significantly from author to author, however, only qualitative conclusions may be drawn from them.
The defect concentration is calculated from the DLTS spectra with the standard procedure illustrated in [54] and in Section 3.2.3, based on peak height detection. It should be pointed out that this evaluation procedure leads to reliable trap concentration values only for electron-irradiated samples, which exhibit DLTS spectra comprising of localized peaks and thus allowing the use of Eq. 3.18. For proton-irradiated samples, the peak height detection cannot be applied due to the broad feature of the DLTS spectra. This issue is further discussed in Section 7.5.
The defect introduction rate is computed as $k_\mathrm{t} = N_\mathrm{t}/\Phi$. In the evaluation of k_t, ΔC_0 in Eq. 3.18 is considered to be the only source of error for N_t. We express the uncertainty on N_t by using the relative error μ_N, i.e., the maximum absolute error divided by the averaged value. μ_N accounts for the error in the peak determination (noise at the peak floor) as well as for the statistical variation of the peak heights observed from sample to sample for a similar irradiation condition. μ_N varies from trap to trap and in the worst case it is found to be 0.15. As k_t involves a ratio of two quantities, the relative error on k_t, μ_k, is calculated as the the sum of the contributions of μ_N and the relative error on the fluence μ_Φ. A value of $\mu_\Phi = 0.1$ is provided by the irradiation facility, and it accounts for the uncertainty in the dosimetry determination. Therefore, in the worst case the relative error $\mu_\mathrm{k} \approx 0.25$.
The NIEL describing the introduction rate of each trap is obtained with a procedure similar to the one described in Section 2.3.1. The NIEL dependence of the experimental introduction rate are fitted with:

$$k_\mathrm{t} = \mathrm{NIEL} \cdot \mathrm{eDIR}\,, \tag{7.1}$$

with eDIR defined in Chapter 6. The optimum E_d values for Ga and As atoms are interpreted as the threshold energy for defect formation. In the fitting process, both Ga and As E_d are varied to find the best combination describing the measured introduction rates. If the difference between the resulting Ga and As E_d does not differ significantly, a second fitting routine is performed by imposing the same value of E_d for Ga and As. The resulting E_d value for both Ga and As atoms is interpreted as an equivalent threshold energy for the defect, as already done in Chapter 6. It should be remarked here, as already done in Section 6.4.2, that the defect E_d resulting from the NIEL fitting procedure has a physical meaning associated to the defect configuration only if no significant reordering effect occurs at the irradiating temperature (300 K).
In contrast to the analysis in $\mathrm{In_{0.01}Ga_{0.99}As}$ reported in Section 6.5, the NIEL fitting for the defect E_d is performed both before (BA) and after (AA) annealing stage. Two resulting values, $E_\mathrm{d,BA}$ and $E_\mathrm{d,AA}$ are extracted. If no reordering effect is observed for the defect at the annealing temperature of 333.15 K, $E_\mathrm{d,BA} = E_\mathrm{d,AA}$ is expected. If $E_\mathrm{d,BA} \neq E_\mathrm{d,AA}$, this is representative of a significant annealing effect on

the defect concentration, as it will be discussed in Section 7.4.3; in this case, $E_{d,AA}$ cannot be related to the defect configuration anymore. As $E_{d,AA}$ may be affected by the annealing stage, $E_{d,BA}$ is the value which more closely relates to the physical threshold energy for the defect formation.
The effect of the annealing stage on the defect concentration is quantified for each defect by the relative variation of the defect concentration γ calculated as:

$$\gamma = \frac{\Delta N_t}{N_{t,BA}} = \frac{N_{t,BA} - N_{t,AA}}{N_{t,BA}}. \tag{7.2}$$

A positive value of γ indicates a beneficial effect in terms of defect recovery. All defects are healed if γ approaches 1. On the other hand, a negative value of γ denotes a detrimental effect of the annealing process on the defect concentration.

7.4 Electron irradiation

7.4.1 Electron traps in n-GaAs

The DLTS spectrum recorded for electron-irradiated samples is shown in Fig. 7.1 (a) for the 1 MeV case. The measurement conditions are reported in Section 7.2. At BOL conditions, only the EL2 defect is observed with an activation energy of 0.76 eV, as shown with the dotted black line in Fig. 7.1 (a). The activation energy is in line with values found in the literature [96]. Four main traps are detected in the irradiated cases, labeled E1, E2, E3 and E4. The peak associated to E2 has also a small shoulder denoted with E2'. A time window $t_w > 10$ ms, corresponding to a rate

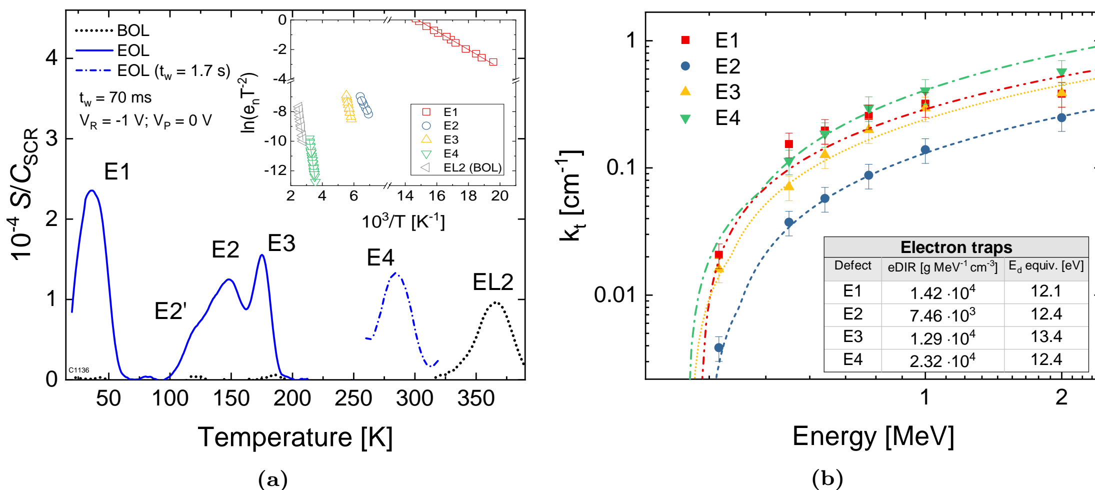

Figure 7.1 – (a) DLTS signal S normalized by the depletion layer capacitance C_{SCR} of BOL (black dotted line) and 1 MeV electron-irradiated (blue lines) n-GaAs mesa-diodes with fluence $\Phi = 1.5{\cdot}10^{15}$ cm^{-2}. The irradiated spectrum at $t_w = 100$ ms is also plotted for the irradiated case, in order to show the peak related to E4, otherwise not visible with $t_w = 70$ ms. The Arrhenius plots of the different traps are reported in the inset. (b) Energy-dependent introduction rate k_t for electron traps in electron-irradiated n-GaAs before annealing. The NIEL curves calculated with the equivalent defect E_d (obtained imposing $E_{d,Ga} = E_{d,As}$ in the fitting process) and scaled by the eDIR factors are superimposed.

below $100\,\mathrm{s}^{-1}$, has to be chosen in order to distinguish clearly the E2 and E3 peaks. The energy levels varies slightly from sample to sample. The defect associated to the E1 level is a very shallow electron trap and has an activation energy of 30∼50 meV. The E2 trap features a broader peak and has an activation energy which varies from irradiation cases between 0.15 eV and 0.21 eV. The E2' activation energy cannot be determined from the measured spectra. The defect level E3 is a deep level featuring a very sharp peak and a nearly pure exponential transient, with an activation energy of 0.37∼0.41 eV. The defect E4 is located at 0.60∼0.65 eV below E_C. We did not sample the EL2 defect in the irradiated samples as its peak position for rate below $100\,\mathrm{s}^{-1}$ is found at $T > 360\,\mathrm{K}$, thus out of our temperature range to preserve stable defect conditions. However, the EL2 defect is expected to be produced in irradiated samples [96]. The defect levels E1 and E2 have been already reported in the literature ([89] and [88], respectively). The defect level E3 is also reported in the literature [48], although the value measured in this experiment is slightly higher. According to DFT simulation, such an energy level could correspond to either Arsenic vacancy (V_Ga) or intestitial (I_As) [0/+], or a divacancy [41]. It is important to point out that different energy levels may correspond to different charge state transition of the same type of defect, e.g., a Frenkel pair (FP) with different interatomic spacing [88]. The NIEL analysis is performed on the defect introduction rate as explained in Section 6.4.2. The defect introduction rates are reported in Fig. 7.1 (b). The data points are the measured introduction rates with error bars given by μ_k. The customized NIEL curves calculated for each defects are superimposed. The optimum E_d values as well as the eDIR factor are tabulated in the inset of Fig. 7.1 (b). All defect introduction rates are found to scale with the NIEL $E_\mathrm{d} = 12{\sim}13\,\mathrm{eV}$ and different eDIR factors in both BA and AA cases. The E_d values found matches well the 13 eV value obtained by molecular dynamics simulations [19] as the most likely threshold displacement energy for recoils in GaAs lattice. Therefore, E1-E4 can be ascribed to single-displacement defects. Regarding the nature of E3, the divacancy can be ruled out as double displacement defect would result in a higher threshold energy.

7.4.2 Hole traps in p-GaAs

The DLTS spectrum recorded for electron-irradiated p-type samples is shown in Fig. 7.2 (a) for the 1 MeV case. The BOL measurement is shown with a dotted line in Fig. 7.2 (a). At BOL conditions, only the defect H7 is detected, with an activation energy of 0.55 eV. The energy level position is in very good agreement with the double donor [++/+] charge state of the EL2 defect in p-GaAs [97,98] due to an antisite $\mathrm{As_{Ga}}$-related defect. This is in line with the fact that $\mathrm{As_{Ga}}$ is expected to be the most abundant point defect produced within the GaAs layer during the epitaxial growth by MOCVD.
Six additional defects are detected after irradiation, labeled from H1 to H6 in ascending order for peak temperature detection. The activation energies are extracted by fitting of the Arrhenius plots of e_p/T^2 reported in the inset of Fig. 7.2 (a). The defect associated to the H1 level is a very shallow hole trap 35 meV above E_V. The defect level H2 is located 0.13 eV above E_V and its concentration is lower compared to all other levels. The H3 energy level is located 0.27-0.30 eV above E_V. This trap

level has already been found in the literature [48]. As this level was also detected in samples irradiated at 4 K by Pons *et al.*, the authors in [89] concluded that this trap is associated to a primary defect. The activation energy found in this work is very close to the energy levels of V_{Ga}, V_{As} and $\mathrm{Ga}_{\mathrm{As}}$ according to DFT simulations [41,42]. The trap H4 and H5 are located at 0.33 eV and 0.37 eV above E_{V}, respectively, and they exhibit a strong variation in peak height from sample to sample. This effect is not completely understood, and more work is necessary to understand the nature of these traps. The defect H6 is located 0.48 eV above E_{V}; this values is not commonly found in the trap list of irradiated p-GaAs in the literature. As H6 is not introduced by 0.5 MeV electron irradiation, it is likely that it is produced by recoils with higher energy. In this regard, DFT simulations show that a similar level could correspond to a particular charge state of the $\mathrm{Ga}_{\mathrm{As}}$ antisite [41].
The NIEL analysis for the H1-H7 defects is reported in Fig. 7.2 (b). The data points are the measured introduction rates with error bars given by μ_{k}. The NIEL calculated with similar E_{d} for Ga and As atoms are superimposed, as well as the eDIR value for the data fitting. The fitting values are tabulated in the inset of the figure. The defects H1 and H3 scale with NIEL $E_{\mathrm{d}} = 13$ eV, whereas H4-H7 are found to scale with NIEL $E_{\mathrm{d}} = 19{\sim}23$ eV. As this value is approximately twice as big as the physical threshold energy, they may be related to a defect caused by a double displacement. A value of 22 eV is found for H7, which confirms its nature of $\mathrm{As}_{\mathrm{Ga}}$-related defect.

7.4.3 Annealing dynamics

The annealing of the mesa-diodes were performed as described in Section 7.2. For each defect, the effect of the annealing is quantified by the γ parameter defined in

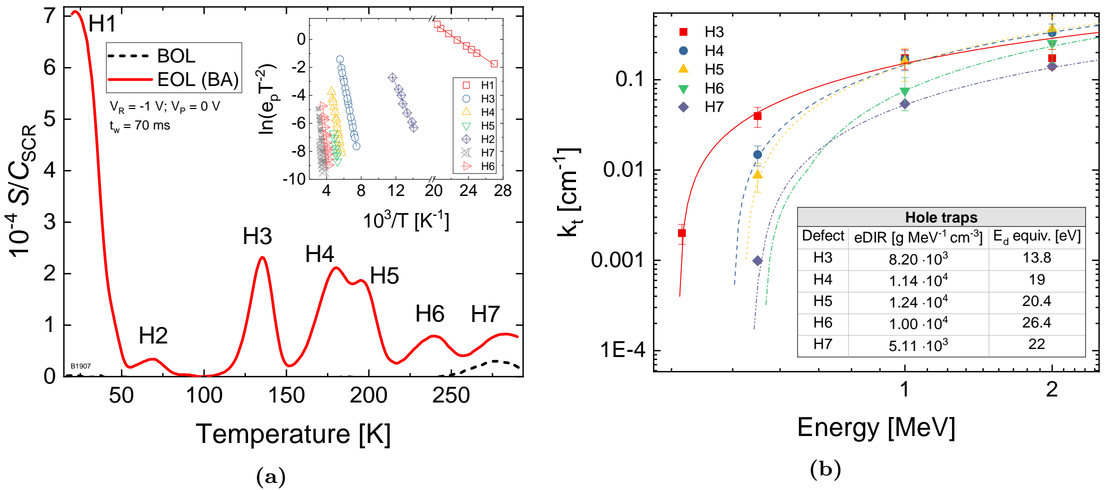

Figure 7.2 – (a) DLTS signal S normalized by the depletion layer capacitance C_{SCR} of BOL (black dotted line) and 1 MeV electron-irradiated (red lines) p-GaAs mesa-diodes with fluence $\Phi = 1.5{\cdot}10^{15}\,\mathrm{cm}^{-2}$. The Arrhenius plots of the different traps are reported in the inset. (b) Energy-dependent introduction rate k_{t} for electron traps in electron-irradiated p-GaAs before annealing. The NIEL curves calculated with the equivalent defect E_{d} (obtained imposing $E_{\mathrm{d,Ga}} = E_{\mathrm{d,As}}$ in the fitting process) and scaled by the eDIR factors are superimposed.

Eq. 7.2. In this section, we first discuss the annealing observed via DLTS measurements in n-GaAs and p-GaAs separately. Then, general conclusions on the defect annealing dynamics are drawn.

Annealing of defects in n-GaAs

All defects are found to be stable with respect to the thermal annealing stage with the only exception of E3, whose concentration is found to decrease as visible in Fig. 7.3. The fraction of healed E3 defects are quantified by $\gamma = \sim 0.22$, a value which is fairly independent of the irradiation energy. DFT simulations shows that the the E3 level can be associated to an As single displacement defect. Since E3 has the sharpest peak feature and is the first and only level to exhibit beneficial reordering effects, it could be ascribed to an As FP with short interatomic distance. In this case, the decrease in the concentration following annealing stage is understood as a direct recombination of the closely-spaced FP. Alternatively, it could be ascribed to an As interstitial or vacancy that diffuses away from the sampled portion of the SCR during the thermal annealing. An isochronal annealing study could clarify the nature of this trap, although this analysis is not performed within the scope of this dissertation.

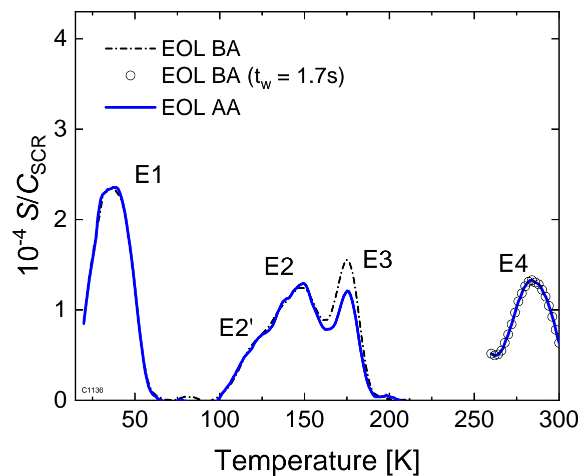

Figure 7.3 – DLTS signal S normalized by the depletion layer capacitance C_{SCR} of 1 MeV electron irradiated n-GaAs mesa-diodes with fluence $\Phi = 1.5 \cdot 10^{15}\,\mathrm{cm}^{-2}$ measured before (BA) and after (AA) annealing stage at 333.15 K for 48 h in dark. The irradiated spectrum at $t_{\mathrm{w}} = 100\,\mathrm{ms}$ is also plotted for the irradiated case, in order to show the peak related to E4, otherwise not visible with $t_{\mathrm{w}} = 70\,\mathrm{ms}$.

Annealing of defects in p-GaAs

The DLTS spectrum measured in p-GaAs irradiated with 1 MeV electrons and measured following the annealing stage for 48 h at 333.15 K is shown in Fig. 7.4. The traps H1-H3 and H6 show no variation in the peak height and shape after the annealing stage. The traps H4 and H5 exhibit a partial recovery. The trap H7, on the other hand, shows a detrimental behavior after the annealing stage. The variation in defect concentration for the defect H4, H5 and H7 is observed at different

extent for the experiments at different electron energies. This is the reason why, the NIEL analysis performed after the annealing stage leads to different values of the equivalent defect E_d as compared to the values before annealing.

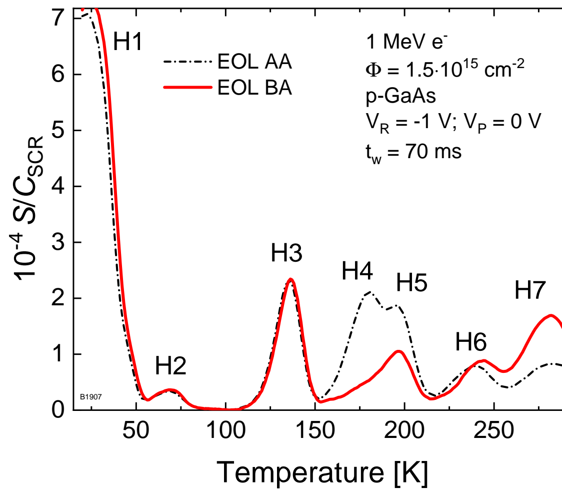

Figure 7.4 – DLTS signal S normalized by the depletion layer capacitance C_{SCR} of 1 MeV electron irradiated p-GaAs mesa-diodes with fluence $\Phi = 1.5{\cdot}10^{15}\,\mathrm{cm}^{-2}$ measured before (BA) and after (AA) annealing stage at 333.15 K for 48 h in dark.

Overview on defect annealing dynamics

The DLTS spectra comparing before and after annealing measurements in n- and p-GaAs are plotted in Fig. 7.3 and 7.4, respectively.
The γ values for the defects which exhibit a variation of their concentration after the annealing stage, namely H4, H5, H7 in p-GaAs and E3 in n-GaAs, are plotted as a function of the electron energy in Fig. 7.5.
A $\gamma \approx 1$ is found for H4 and H5 in the 0.5 MeV electron case, whereas it decreases at higher energies. For these defects, the short-cascade recoils of low-energy electrons

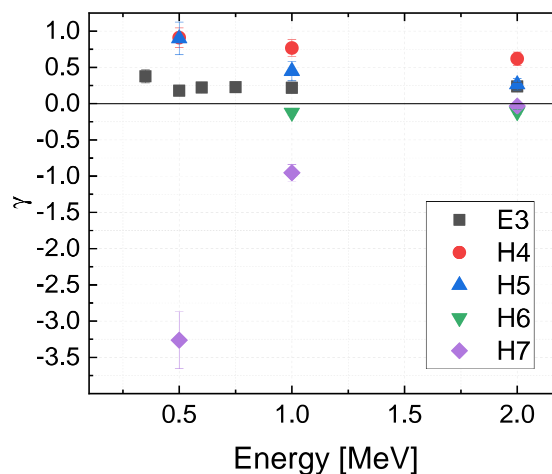

Figure 7.5 – Relative fraction of healed defects γ, calculated with Eq. 7.2,after thermal annealing regime (48 h in dark at 333.15 K) as a function of the electron irradiation energy for the defects H4, H5, H6 and H7 in p-GaAs and E3 in n-type GaAs.

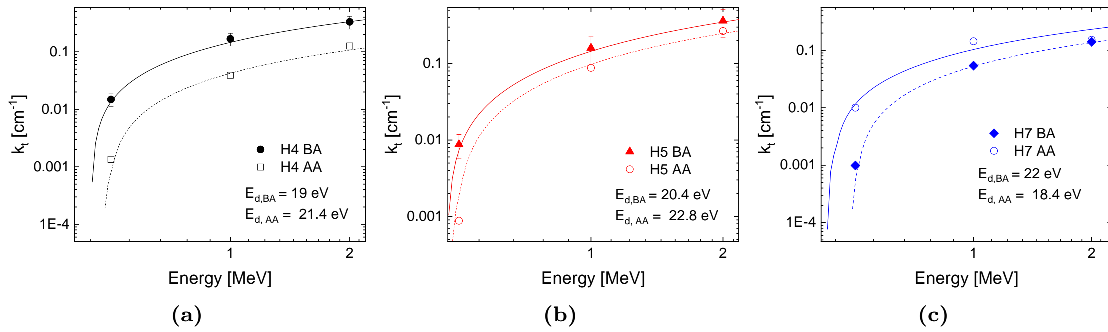

Figure 7.6 – Energy-dependent introduction rate k_t for the trap (a) H4, (b) H5 and (c) H7 in electron-irradiated p-GaAs mesa-diodes before (BA) and after (AA) annealing stage for 48 h at 333.15 K.

facilitate defect annihilation during the temperature annealing, i.e., the defects are more closely spaced for low electron energy irradiation, thus defect recombination is facilitated. The energy-dependent annealing factor γ influences the defect E_d parameter found with the NIEL fitting routine on the annealed introduction rates. For the E3 defect, a constant γ value is observed, as discussed already in Section 7.4.1. The defect annihilation rate is thus independent of the electron energy, and no effect is observed in the fitting of the defect E_d. The most striking feature comes from the H7 defect. An energy-dependent detrimental effect due to the annealing stage is observed. For the 0.5 MeV case, this is quantified by $\gamma = -3.25$; at 1 MeV the factor decreases to -1 whereas for the 2 MeV case it is almost 0. As no consistent match is found between the decrease of the H4 and H5 and the increase of the H7 concentration, the annealing dynamics are considered to be unrelated. A speculation on the origin of the H7 detrimental annealing effect can be related to the diffusion of I_{As} within the portion of SCR sampled via DLTS, in combination with the thermally-aided process leading to an I_{As} to fall into a V_{Ga}. This, however, does not explain the inverse energy-dependence of the γ factor. More investigation is required to understand the physical basis behind the H7 production following thermal annealing.

The influences of the annealing stage on the introduction rate plots and the defect E_d obtained in the NIEL fitting is shown in Fig. 7.6 for the defects H4, H5 and H7 in p-GaAs. The NIEL curves are calculated with the E_d values reported in Table 7.2. It should be remarked that the defect $E_{d,BA}$ obtained with introduction rate data before annealing are more closely related to the real physical threshold energy for defect creation.

A summary on the trap levels and threshold energies E_d before and after the annealing stage is reported in Table 7.2.

7.4.4 Correlation with the trap levels in $In_{0.01}Ga_{0.99}As$

It is interesting to compare the defects detected in GaAs mesa-diodes via DLTS with the ones in $In_{0.01}Ga_{0.99}As$ component cell via AS. The comparison in terms of energy levels should be done with care, however, for the reasons explained in Section 7.1. In particular, the sensitivity of the emission rate to the electric field for defects in

Mesa-diode	Trap	E'_t [eV]	$E_{d,BA}$ [eV]	$E_{d,AA}$ [eV]
p^+-n	E1	0.051	12.1	12.1
	E2	0.19	12.4	12.4
	E3	0.42	13.4	13.4
	E4	0.61	12.4	12.4
n^+-p	H1	0.035	11.2	11.2
	H3	0.28	13.8	13.8
	H4	0.33	19	21.4
	H5	0.37	20.4	22.8
	H6	0.48	(26.4)	(26.4)
	H7	0.55	22	18.4

Table 7.2 – Trap energy level E'_t (referred to the respective band edges) and threshold energy E_d obtained from the NIEL fitting of the introduction rates before (BA) and after (AA) annealing stage (48 h at 333.15 K) in electron-irradiated GaAs mesa-diodes. The values within brackets may suffer of high uncertainty.

III-V materials [60] is expected to be an important factor for the scattering of the energy level data. The electric field-dependent emission rate in GaAs was already observed and described in detail via DLTS by Fleming *et al.* [95]. For instance, a study on the double donor level of the EL2 in GaAs, labeled H7 in our DLTS study, revealed that its apparent energy level can vary from 0.3 eV up to 0.61 eV when the emission rate is observed under different electric field conditions [97].

A similar effect is also observed in our samples. For instance, the plot in Fig. 7.7 shows several DLTS spectra acquired for 1 MeV electron-irradiated p-GaAs diodes, measured with V_R = -3 V fixed and varying the filling pulse V_P from -2.5 V to 0 V. As V_P is increased, the probed slice of the SCR where the trap emission is observed

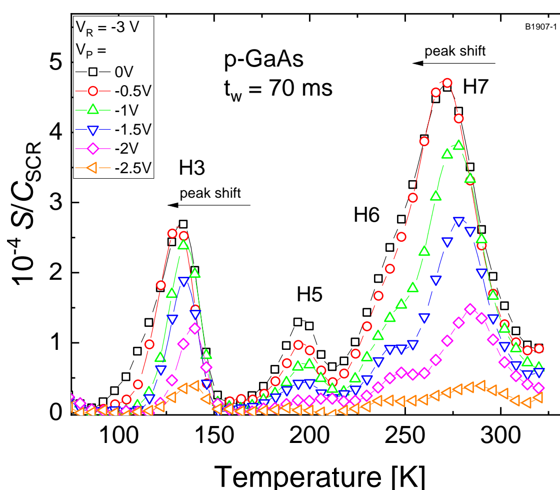

Figure 7.7 – DLTS signal S normalized by the depletion layer capacitance C_{SCR} in 1 MeV electron-irradiated p-GaAs with $\Phi = 1.5{\cdot}10^{15}$ cm^{-2} following annealing stage for 48 h at 333.15 K. The measurements were performed with a constant reverse bias V_R = -3 V and with varying filling pulse V_P.

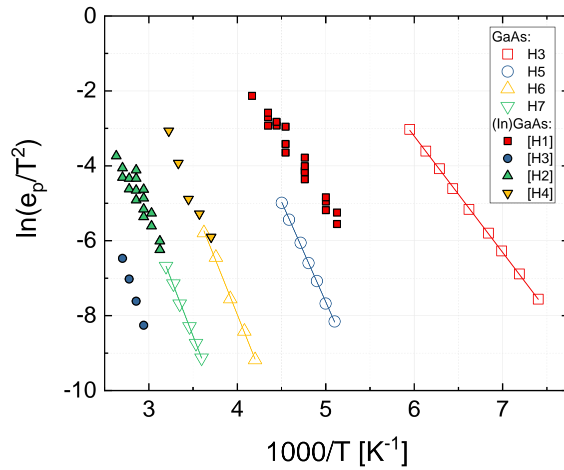

Figure 7.8 – Trap signatures in irradiated p-GaAs and p-$In_{0.01}Ga_{0.99}As$ after annealing stage (48 h at 333.15 K) detected via DLTS and admittance spectroscopy, respectively. The traps in p-$In_{0.01}Ga_{0.99}As$ are labeled within square brackets. The value of e_p is calculated from t_w in the DLTS case, whereas from f_t in the AS case.

during DLTS is increased as well (this can be understood from Fig. 3.5). As the probed region increases toward the inner of the junction, i.e., the zone with maximum electric field, the traps are subjected to a higher electric field profile during carrier emission. If the trap is sensitive to the electric field, a variation of the DLTS spectra is observed.

The peak position of the single traps shifts toward lower temperatures with a different rate. The effect is clearly observed in Fig. 7.7 for the trap H3 and H7. This is interpreted as an enhancement of the trap emission rate due to electric field. Moreover, as V_P is increased, the peaks feature a broader symmetrical shape, which can be a sign of tunneling-assisted emission rate always related to the electric field.

Despite the limitations introduced by electric field-dependent emission rates, a com-

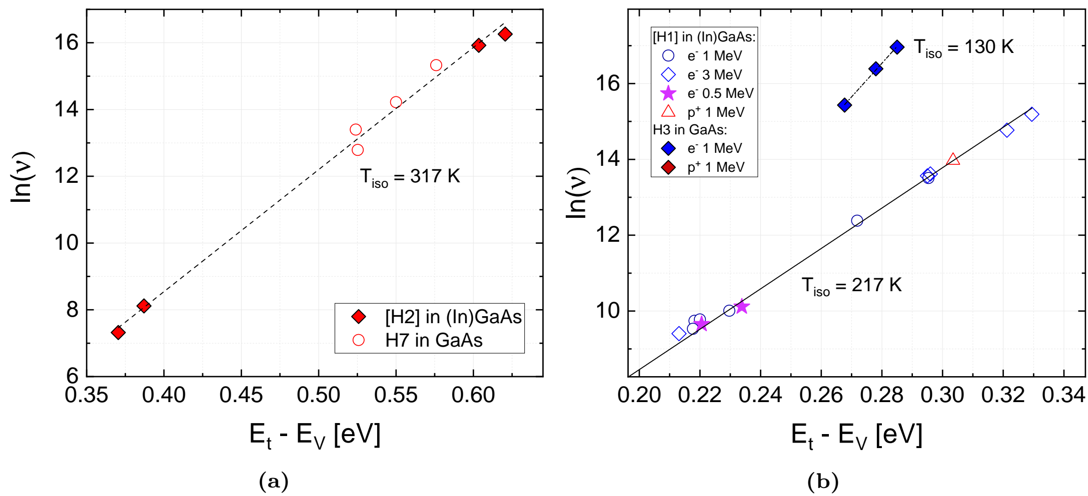

Figure 7.9 – Meyer-Neldel plot, as described in Section 3.2.3, for the defects (a) [H2] and H7 and (b) [H1] and H3 in p-$In_{0.01}Ga_{0.99}As$ and p-GaAs, respectively. The defects in p-$In_{0.01}Ga_{0.99}As$ are labeled within square brackets. The linear fits are performed with Eq. 3.22.

parison of the trap signatures (e_p/T^2) is a first way to assess whether similar energy levels correspond to the same structural defect in the two cases. In Fig. 7.8, the trap signatures for the defects observed in p-GaAs and p-$In_{0.01}Ga_{0.99}As$ after the respective annealing stages are shown.
The traps H3, H5, H6 and H7 are the most relevant after the annealing stage in p-GaAs. They are compared to the traps H1, H2, H3 and H4 in p-$In_{0.01}Ga_{0.99}As$. To avoid ambiguity in the discussion, from now on we will refer to the traps in $In_{0.01}Ga_{0.99}As$ with the trap label in square brackets.
The traps H6 and [H4] exhibit a quite similar Arrhenius plot, although the uncertainties in the determination of the $-f{\cdot}\mathrm{d}C/\mathrm{d}f$ peak for [H4], as discussed in Section 6, prevents to draw strong conclusion for this trap.
Another similarity is found between the signatures of H7 and [H2]. As H7 is an As_{Ga}-related defect, its presence is expected in both materials.
Similar energy levels, however, do not imply that the type of defects introduced is the same. In order to check whether the trap sampled in the two cases are coming from the same type of defect, an MNR analysis is performed by using the data for the activation energy E'_t and pre-exponential factor ν (as defined in Eq. 3.17) obtained in the two cases. The analysis with the empirical method of the MNR plots is explained in Section 3.2.3. In this case, we try to observe whether the scattering of the E'_t and ν data can be described by the MNR, i.e., the plot of E'_t-$\ln(\nu)$ data falls on a straight line described by Eq. 3.22 with $\Delta H = E'_t$. The MNR plot for H7 and [H2] is shown in Fig. 7.9 (a). The scattering of the $\ln(\nu)$ and E'_t data from both defects falls on a straight line characterized by $T_{iso} = 317\,\mathrm{K}$. Therefore, H7 and [H2] may be attributed to the same defect. In terms of defect E_d, however, H7 has a post-annealing value of 18.4 eV, whereas [H2] has a much higher value of 38 eV. It should be pointed out that the latter value has higher uncertainty due to the few data points available in the NIEL fitting. Moreover, the photon annealing in $In_{0.01}Ga_{0.99}As$ might also play a role in defining the final annealing configuration and thus the defect E_d. Ultimately, it should be mentioned that the two experiments were conducted at two different irradiation facilities. The different dosimetry may affect significantly the E_d results.
The defect [H1] and [H3] are not observed in p-GaAs. Although the [H1] signature is very different from the one of H3, a similarity between the energy levels is observed. An obvious question is whether the levels are related to the same type of defect. The MNR plot for these defects is shown in Fig. 7.9 (b). No linear relationship between the admittance spectroscopy and DLTS data is found. This can be interpreted as a sign that the two energy levels have different properties and thus may be attributed to different type of defects.

Final considerations

As a conclusive summary of this section, the comparison between the traps detected in p-$In_{0.01}Ga_{0.99}As$ and p-GaAs is somewhat inconsistent. The inconsistencies found for the trap signatures requires further investigation. Possible source of differences are the slightly different material composition of the two samples and the influence of the electric field on the emission rate of the traps. Moreover, the influence of

the different spectroscopy techniques on the defect parameter extraction should be properly addressed in order to validate the comparison.

Only the trap associated to the double donor state of the EL2 ([H2] in p-$In_{0.01}Ga_{0.99}As$, and H7 in p-GaAs) is consistently found in both material and the scattering of the E'_t and $\ln(\nu)$ values satisfies the Meyer-Neldel rule. Even for this trap, however, a different threshold energy for defect formation E_d in the two cases is found. The value of E_d should be characteristic of the type of defect, thus independent of the measurement technique. As the two set of samples were irradiated with electrons at two different irradiation facilities (Sirius and TU Delft), the different dosimetry and irradiation conditions might play a role in this discrepancy. This poses a warning and an incentive to understand whether, in a more general overview, irradiation experiments at the two facilities can be directly compared.

7.4.5 Effective defect NIEL*

The NIEL* is the total NIEL introduced in the material following an irradiation experiment, calculated directly from the defect introduction rates as explained in Section 6.6.1. An obvious question is whether the effective NIEL* calculated with Eq. 6.4 in GaAs mesa-diodes can be compared to the one calculated in $In_{0.01}Ga_{0.99}As$ reported in Fig. 6.5.

The calculated NIEL* with introduction rate data from DLTS in n- and p-GaAs is plotted in Fig. 7.10. The blue symbols are the NIEL* values computed in $In_{0.01}Ga_{0.99}As$, and the attenuated $NIEL_{21eV}$ curve is superimposed as in Fig. 6.5. The NIEL* in p-GaAs is plotted with open squares. The values are much higher than the one calculated for p-$In_{0.01}Ga_{0.99}As$. Moreover, NIEL* in p-GaAs follows a typical $NIEL_{13eV}$ instead of a $NIEL_{21eV}$ trend, as found for p-$In_{0.01}Ga_{0.99}As$ in Chapter 6. The NIEL* in n-GaAs is plotted with black diamonds. This is slightly lower than the one calculated for p-GaAs, and it also follows a $NIEL_{13eV}$ trend. In theory, the NIEL* in n- and p-GaAs should be the same. It should be remarked here, however, that our estimation of the NIEL* with Eq. 6.4 accounts for the defects in the material which are measurable with our spectroscopy techniques. The missing contributions in the NIEL* could come from defects not observable in the materials due to the limited temperature range for DLTS measurements, or from annealed defects.

Assuming that all the energy levels in n- and p-GaAs correspond to different defects, the total NIEL* in GaAs, plotted with red spheres, is calculated as the sum of the n- and p-type contributions. The so-calculated total NIEL* in GaAs follows an attenuated $0.4 \cdot NIEL_{13\,eV}$ curve.

The most striking feature observed when comparing the defect NIEL* data from p-$In_{0.01}Ga_{0.99}As$ component cells and p-GaAs mesa-diodes is the different value of E_d found in the NIEL trend. It is unlikely that this difference comes from the different material composition, as this is limited only to 1% In concentration in the component cells. Therefore, since p-$In_{0.01}Ga_{0.99}As$ and p-GaAs were irradiated at two different facilities (TU Delft and Sirius, respectively), it is likely that the inconsistency arises from the different dosimetry techniques. More work is necessary to clarify the mismatch observed in the NIEL* data of the two experiments.

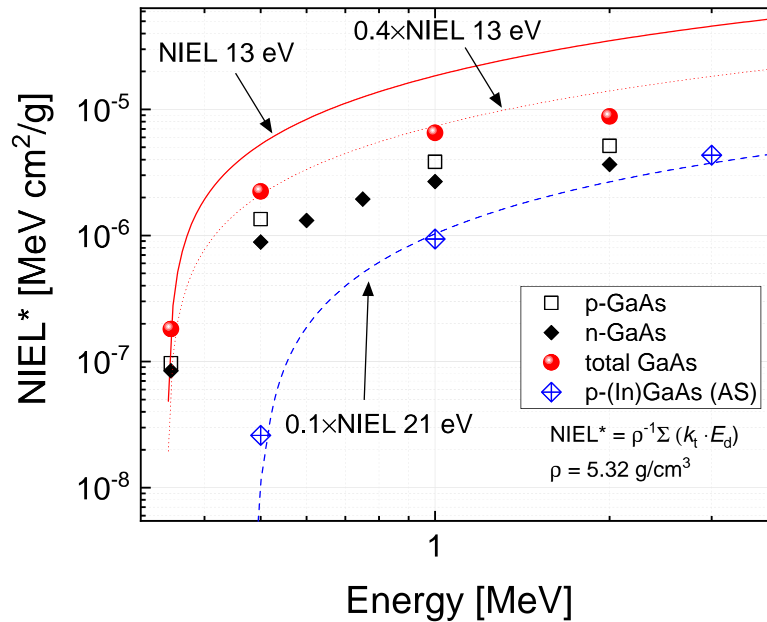

Figure 7.10 – Effective NIEL* calculated from defect introduction rates in electron-irradiated p-GaAs and p-$In_{0.01}Ga_{0.99}As$ according to Eq. 6.4. The total defect NIEL* in GaAs is obtained by summing the n- and p-type contributions. The NIEL* obtained in p-$In_{0.01}Ga_{0.99}As$ component cells is plotted with blue diamonds. The NIEL curves calculated analytically are superimposed.

7.5 Proton irradiation

The DLTS spectra for the 1 MeV proton irradiation case in n- and p-GaAs are reported in Fig. 7.11 (a) and (b), respectively. The dashed curves and the red solid curves are the measurements before and after the annealing stage, respectively. The 1 MeV electron irradiation spectra are superimposed with a blue dash-dotted line for comparison. For the measurements performed after the annealing stage, the maximum temperature for the DLTS scan is set to 320 K, so that the trap E4 is visible with $t_w = 100$ ms in the n-GaAs case. All defects detected for the electron irradiation are also produced with proton irradiation. In addition, the electron trap E4' is produced in n-GaAs which is not observed in electron-irradiated samples. E4' is identified in the spectrum as a side peak of E4. The activation energy of E4', estimated to be ~0.61 eV, is similar to E4. The effect of the annealing stage is similar to what has been observed in the electron case and reported in Fig. 7.5, namely a beneficial effect on E3, H4 and H5 whereas a detrimental effect for H7.

A proper evaluation of the defect concentration in proton-irradiated samples is made difficult by the broad feature of the DLTS spectra. In fact, the direct evaluation from the peak height with Eq. 3.18 is only valid when the transient associated to each defect is exponential, i.e., the DLTS signal produces a sharp peak. This is the case for electron spectra but not for the proton spectra. Evaluation of the defect concentration from broad-featured DLTS spectra should be accomplished in a more rigorous way by using the formalism proposed by Omling *et al.* [61]. Even in this case, the analysis is made difficult by the large number of defects and by the asymmetry found in the peak shapes. Therefore, a quantitative analysis on the proton defect introduction rate cannot be performed for this experiment.

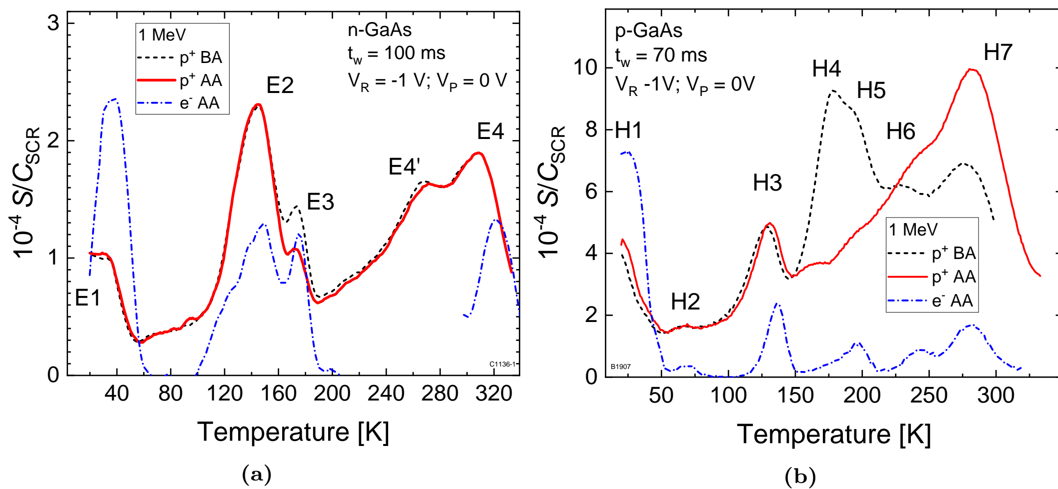

Figure 7.11 – DLTS signal S normalized by the depletion layer capacitance C_{SCR} of 1 MeV proton irradiated (a) n- and (b) p-GaAs mesa-diodes with $\Phi = 1{\cdot}10^{12}\,\mathrm{cm}^{-2}$ before (black dotted curve) and after (red solid curve) annealing stage for 48 h at 333.15 K. The respective spectra for the annealed 1 MeV electron irradiation cases with $\Phi = 1.5{\cdot}10^{15}\,\mathrm{cm}^{-2}$ are superimposed with blue dash-dotted curves.

7.5.1 Difference between proton and electron damage

Despite of the limitation in data evaluation as explained in Section 7.5, the most striking feature in the proton spectra, in analogy with the admittance results in Chapter 6, is the absence of a clear pattern with sharp and localized peaks. The proton DLTS signal can be viewed as the sum of the contributions due to localized peaks attributed to individual traps (as observed in the electron spectrum) with the addition of multiple broader contributions with no clear peak feature. The latter contribution is not observed in any electron irradiation experiment. A complete Gaussian de-convolution of the proton-spectra is hard to achieve and it is not subject of this analysis. As remarked in Chapter 6, this feature can be attributed to continuous distribution of energy levels in the band gap as a result of a more complex crystallographic defect configuration, clustered defects, strain broadened defect levels or to electric field-enhanced emission due to carrier tunneling.
The broad DLTS spectra has been already observed in GaAs devices irradiated with heavy particles [99]. In Fig. 7.12, the proton and electron DLTS spectra measured in this work are compared with the data obtained by Fleming *et al.* on MBE-grown GaAs devices irradiated with fast neutrons at $\Phi = 3{\times}10^{14}\,\mathrm{cm}^{-2}$ [93]. The single broad-featured peak in the DLTS spectrum of neutron-irradiated p-GaAs was termed L-band, in analogy with the U-band found in n-GaAs by the same author and in references listed in [93]. The neutron-atom collision is better described by a hard sphere rather than Coulombic collision. Despite the low cross-section for neutron collision with Ga and As atoms, the generated recoils can have very high energies [100, 101], thus producing long collision cascades [102]. The broad band found in [93] was attributed to the extended clustered damage formed by these collision cascades, which accounts for most of the displacements introduced by neutrons. The DLTS spectra of proton- and electron-irradiated p-GaAs measured in this work are superimposed to the neutron spectra in Fig. 7.12. The amplitude of the

DLTS signal are conveniently scaled to facilitate the comparison of the spectra shape, as quantitative comparison are not possible. The differences observed between the electron, proton and neutron DLTS spectra can be taken as an evidence of the influence of the particle recoil energies on the introduced damage. The plot in Fig. 7.12 gives an overview on the type of defects introduced in the solar cell when the displacements are produced by different recoil energies: low-energy recoils prevail in electron-irradiated samples, and the spectrum comprises of sharp localized peaks due to discrete energy levels (point-like defects); clustered damage due to major contribution of long collision cascades characterizes the broad and almost featureless peaks of the neutron spectrum; in proton-induced damage both low- and high-energy recoils are significantly contributing in the total displacement damage and therefore the broadening of the spectrum is less pronounced as compared to the neutron case, though it does not contain only sharp peaks as in the electron case.
Despite the obvious limitation for quantitative comparison, it is evident how 1 MeV protons introduce a different type of damage than electrons, which resembles a more clustered nature. The importance of the clustered damage and its enhanced damaging effect on solar cell parameters has been already pointed out in the literature [99, 103]. This has been verified experimentally in $In_{0.01}Ga_{0.99}As$ component cells and confirmed by DLTS analysis in both n- and p-GaAs material in this work.

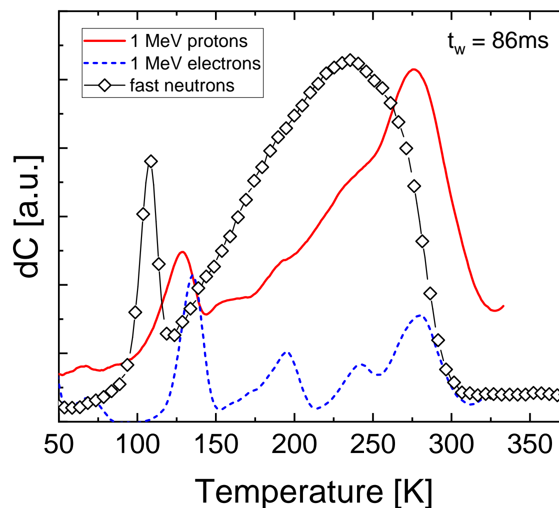

Figure 7.12 – DLTS spectra of p-GaAs irradiated with 1 MeV electrons at $1.5{\cdot}10^{15}$ cm^{-2} (dashed blue curve), 1 MeV protons at $1{\cdot}10^{12}$ cm^{-2} (solid red curve) from this work (Fig. 7.11) and p-GaAs irradiated with fast neutrons at $3{\cdot}10^{14}$ cm^{-2} (open diamonds). Neutron data are taken from Ref. [93]. The three irradiation cases do not introduce the same DDD in the cells. The DLTS signals are conveniently scaled, in order to highlight the different peak shape.

7.6 Conclusion

DLTS is used on electron- and proton-irradiated n- and p-type GaAs mesa diodes to sample the majority carrier traps in GaAs materials of both polarity. The traps, associated to irradiation-induced defects, are characterized in terms of concentration and apparent energy levels within the band gap. The NIEL analysis, as performed

on p-$In_{0.01}Ga_{0.99}As$ component cells in Chapter 6, yields the threshold energy E_d for defect production. Moreover, the dynamic of the defect parameters following thermal annealing for 48 h at 333.15 K is studied.
The data obtained in this work, supported by previous literature data on irradiation-induced defects in GaAs, gives partial information on the nature of the defects created in the material. The remarked different found between electron- and proton-induced defects in GaAs is in agreement with what has been observed via admittance spectroscopy in p-$In_{0.01}Ga_{0.99}As$ component cells described in Chapter 6. This gives additional support to the theoretical explanation on the different damage introduced by the two particles.
Nonetheless, several open questions are left from the DLTS analysis, such as the precise assessment of the crystallographic structures of few defects, the influence of the different irradiation conditions at the two different facilities on the extracted threshold energies for defect formation, and the different reordering dynamics observed during temperature annealing. More investigation is necessary to clarify these points, as discussed in the conclusion chapter of this thesis.

Chapter 8

Summary, Conclusion and Outlook

Summary

Solar cells operated in the space environment experience electrical performance degradation over time due to the interaction with energetic electrons and protons. In III-V solar cells, the main cause of degradation is ultimately ascribed to the displacement damage, namely the formation of stable defects in the semiconductor crystal lattice as a result of the elastic collisions between the particles and the target atoms. A detailed characterization of the displacement damage effects on solar cells is required to enable reliable end-of-life (EOL) performance prediction in complex multi-energetic particle environments. This dissertation addresses the electrical characterization of the displacement damage in space-grade triple-junction (3J) $Ga_{0.5}In_{0.5}P/In_{0.01}Ga_{0.99}As/Ge$ solar cells. This is accomplished by characterizing the solar cell following irradiation with electrons and protons in the MeV range and subsequent standard annealing regime representative of space-like conditions. First, the macroscopic photovoltaic parameters of the solar cell are analyzed, namely the short-circuit current density J_{SC} and the open-circuit voltage V_{OC} measured under AM0 spectrum. These quantities are of paramount importance in space solar generator design. The influence of the type and energy of particle radiation is studied with the NRL method [17] (also called Displacement Damage Dose (DDD) method), which makes use of the Non-Ionizing Energy Loss (NIEL) to quantify the amount of displacements introduced into the crystal lattice of the irradiated material. To analyze the degradation one step closer to the physical level of damage, the degradation of the cell dark current in the space-charge region is studied by making use of a Shockley-Read-Hall model including energy levels within the band gap associated to radiation-induced defects. By fitting of the junction ideality factor, a first picture of the electrical effectiveness of irradiation-induced defects is drawn. Subsequently, the displacement damage is characterized in terms of physical defects generated in the material and their effectiveness on the macroscopic cell performance. Capacitance spectroscopy techniques such as admittance spectroscopy (AS) and deep-level transient spectroscopy (DLTS) are used to sample the defect concentration, activation energy and capture cross-sections. The fitting of the defect introduction rate with the electron NIEL provides the threshold energy for defect formation E_d, which is a characteristic of each defect and it contains information on its crystallographic nature.

Conclusion

The displacement damage characterization sheds light on the semi-empirical nature of the NRL method [17], widely adopted by the solar array radiation community to deal with the multi-energetic nature of the space environment. As the state-of-the-art, a NIEL calculated with $E_\mathrm{d} = 21\,\mathrm{eV}$ is found to scale properly the degradation of the solar cell J_SC due to protons and electrons in the MeV range. J_SC is thus a pure function of the DDD only. When the same NIEL is applied to scale the V_OC degradation, protons are found to be more effective than electrons for a similar level of DDD. The discrepancy is accounted for with the introduction of an electron-to-proton correction factor $\mathrm{R_{ep}}$, which is usually in the range 2.5-3.5 for GaAs-based solar cell. The physical nature of these values was not yet clearly defined. The in-depth displacement damage analysis carried out in this work provides a physical explanation to these values, thus improving the physical model of the NRL method. The NIEL in GaAs with $E_\mathrm{d} = 21\,\mathrm{eV}$ is found to accurately describe the scaling of the relative abundance of different defects produced in the solar cell layers. The correlation of the defect concentration with J_SC degradation shows that all defects may contribute to the J_SC damage. As a similar energy scaling is found for J_SC, the minority carrier capture cross-sections of these defects are in a similar range and cannot differ by orders of magnitude. A similar argument is valid for other parameters sensitive to minority-carrier lifetime such as the diffusion saturation current J_{01} and the minority carrier diffusion length L_n.
A different situation is found for the solar cell at V_OC. At high particle doses, V_OC becomes more and more sensitive to the recombination current in the SCR. A pronounced difference of about one order of magnitude in the SCR lifetime is observed, extracted from the dark characteristics of proton- and electron-irradiated component cells with similar DDD. Assuming a comparable capture cross-section for proton and electron-induced mid-gap defects responsible for the SCR lifetime, protons produce more defects close to the intrinsic Fermi level than electrons. Since the same amount of non-ionizing energy is deposited in both cases, a significant amount of electron defects must therefore be distributed in a wider energy range. Alternatively, assuming that protons and electrons introduce similar energy levels, the effect can be explained assuming a higher capture cross-section for the proton-induced mid-gap defects with respect to the equivalent electron-induced defects.
A defect spectroscopy analysis proved that the defects introduced by a similar DDD of protons and electrons have different characteristics. The distribution of defect states around mid-gap has a much broader feature in the proton case, whereas localized sharp peaks are observed in the electron case. This is representative of the fact that electron irradiation produces mainly isolated point defects in the lattice due to the low energetic content of their recoil spectrum (few tens of eV), whereas in the proton case a higher fraction of displacements triggered by high-energy recoils (~keV) produce clustered defects along the collision cascades. Such clusters are found to be stable to the different annealing regimes representative of space-like conditions. A strong correlation is found between the broad spectra and the increased capture cross-sections of mid-gap defects in proton-irradiated solar cells. The higher damaging effectiveness of the proton-induced clustered damage is the ultimate cause the NIEL scaling deviation for the solar cell V_OC, and consequently for the output

power P_{MP}. The $\mathrm{R_{ep}}$ factors can be thus interpreted as cluster-enhancement factors. The analysis rises awareness on the proper irradiation experiments to be considered when energetic electrons and protons account for a big contribution of the radiation environment. At the present state, the degradation of space solar generators relies heavily on the 1 MeV electron degradation data. Since the physical damage introduced by protons and electrons is found to be significantly different, all $\mathrm{R_{ep}}$ factors are only a semi-empirical way to reconcile data. A preferred approach would be to choose the testing particle type and energy range according to the most predominant contribution in a given space mission. The ground testing of the displacement damage degradation with the standard 1 MeV electrons is suitable for the NIEL scaling if no significant contribution comes from electrons with higher energies, i.e., characterized by a recoil spectrum much similar to the proton one. In this case, 1 MeV electrons reproduce accurately the damage state that consists of solely isolated defects. If high-energy electrons or protons ($>$ 1 MeV) contribute significantly in the DDD, both clustered and isolated damage is introduced, thus the NIEL scaling obtained on the basis of data from electrons in the 0.5 - 3 MeV range will underestimate the damage of the radiation environment. With regards to the proton environment, 1 MeV proton irradiation experiment is usually performed to test solar cell against introduced damage consisting of both isolated and clustered defects. The cluster-enhancement effect due to high-energy protons ($>$ 10 MeV) in GaAs-based solar cell [99] suggests that irradiation with protons above 10 MeV, or alternatively fast neutrons, should be preferred in case of space environment with strong contribution of protons above 10 MeV.

Outlook

Admittance spectroscopy is validated on standard $2 \times 2\,\mathrm{cm}^2$ solar cells, typically manufactured for radiation testing purposes. The method provides an alternative to DLTS in defect spectroscopy analysis when no ad-hoc structure is available. Moreover, the direct analysis yields straightforward correlations between irradiation-induced defects and solar cell photovoltaic parameter degradation. A similar analysis can be applied on new-generation component cells where different materials other than GaAs are adopted, in order to investigate their radiation-hardness and the regeneration behavior at a defect level. Moreover, defect spectroscopy combined with NIEL analysis can prove to be beneficial in other fields where radiation effects in semiconductor are of prime relevance, such as radiation detector applications.
Many open questions are left from this work in the field of radiation effects on space solar cells. More investigation would be required to clarify the following points:

- The difference in defect threshold energies E_{d} values found for similar defects introduced in p-(In)GaAs and p-GaAs sheds light on the different damage produced in solar cells when electron irradiation experiments are conducted at TU Delft and Sirius facilities with the same nominal fluence. The energy dependency of the defect introduction rate, studied either via admittance spectroscopy or DLTS, is a valid tool to compare the damage introduced by the different facilities. A similar study as performed in Chapter 7 on samples irradiated at the TU Delft facility may facilitate the understanding of the root

cause of the different degradation behavior.

- The numerical simulations of irradiated GaAs cells can be improved by tracing the equivalent material lifetimes back to defect electrical parameters extracted via DLTS. A more in-depth analysis on the irradiated device can provide accurate values for each defect capture cross-section. In this way, the simulation of irradiated solar cells will be much closely related to the actual process of defect production in the solar cell. Moreover, degradation mechanisms encountered by space solar cells when operating in low-intensity low-temperature conditions [104], relevant for deep-space missions, can also be explained.

- The different annealing dynamics observed for GaAs defects needs a better annealing study in order to confirm their crystallographic nature. A DLTS study combined with isochronal annealing is advised to gain more knowledge in this field. Moreover, further analysis on the apparent detrimental effect of the H7 defect (Section 7.4.3) is essential to properly understand annealing effects on GaAs photovoltaic parameters.

- The annealing of GaInP component cells shows interestingly a different behavior between proton- and electron- irradiation. As this is not observed in GaAs, the difference may arise from defects in the InP lattice. A defect analysis and annealing study on InP-based solar cells irradiated with both particles could yield interesting insights.

- With regards to the NIEL calculation methods, replacing the fully-analytical approach with a semi-analytical formalism aided by molecular dynamic simulations [27] may be a step forward to increase the physical basis of the NRL method.

Acknowledgement

I would like to thank many people who supported me and made this work possible. First, I am deeply grateful to my mentor Claus Zimmermann for his supervision during the whole doctoral program. I consider myself lucky for the chance I had to learn a lot from him at a professional and scientific level. The numerous discussions as well as his valuable inputs on several manuscripts were of paramount importance for the successful completeness of my Ph.D. program. I would like to thank very much my academic supervisor Alessio Gagliardi, who allowed me to be part of his research team at TUM and who constantly followed me throughout the entire doctoral program. Moreover, special thanks go to David Lackner, for his supervision, advice and the inspiring conversations had during my time at ISE. Special thanks also go to my M.Sc. supervisor Heinrich Christoph Neitzert for his help at the very beginning of this experience.
I would like to thank the Solar Array team at Airbus Defence and Space who supported me over the past years, in particular Martin Rutzinger, Manuel Wildfeur, Helmut Nesswetter, Helmut Jenker, Matthias Nikusch, Hans Hofer and Andreas Gerhard for the help and advice provided in all the laboratory activities.
Additionally, I would like to thank Frank Dimroth, who made my visiting research period at ISE possible, and all the III-V team who included me in their activities framed in a nice work atmosphere, making such experience extremely valuable for my doctoral program. Special mentions go to Jonas Schön, Robin Lang and Patrick Schygulla, with whom I had the change to work more closely with.
As every amazing journey, this experience has been flavored with lots of positive and negative moments. In both cases, I was lucky to always found a good friendship behind the corner. Reached the finish line, I have to deeply thank all my friends for their ever-present support. The tight bonds between us have been an extra kick toward the end of this experience. A special mention goes to Davide Silvagni for his patience, numerous advice and all the support that a flatmate and a very good friend could provide.
I want to thank Nora Penzel for being my reference point in these past years, without whom this whole experience would have been half as beautiful as it has been.
Last but not least, I would like to thank all other members of my family for their daily love and support, and in particular my parents, for understanding the amount of time my education has taken away from me spending time with them.

Bibliography

[1] W. Shockley and H. J. Queisser, "Detailed Balance Limit of Efficiency of p-n Junction Solar Cells," *Journal of Applied Physics*, vol. 32, pp. 510–519, mar 1961.

[2] J. F. Geisz, R. M. France, K. L. Schulte, M. A. Steiner, A. G. Norman, H. L. Guthrey, M. R. Young, T. Song, and T. Moriarty, "Six-junction III-V solar cells with 47.1% conversion efficiency under 143 Suns concentration," *Nature Energy*, vol. 5, pp. 326–335, apr 2020.

[3] M. R. Patel, *Spacecraft Power Systems.* CRC Press, nov 2004.

[4] O. D. Miller, E. Yablonovitch, and S. R. Kurtz, "Strong Internal and External Luminescence as Solar Cells Approach the Shockley-Queisser Limit," *IEEE Journal of Photovoltaics*, vol. 2, pp. 303–311, jul 2012.

[5] I. Schnitzer, E. Yablonovitch, C. Caneau, and T. J. Gmitter, "Ultrahigh spontaneous emission quantum efficiency, 99.7% internally and 72% externally, from AlGaAs/GaAs/AlGaAs double heterostructures," *Applied Physics Letters*, vol. 62, pp. 131–133, jan 1993.

[6] M. Feifel, D. Lackner, J. Schön, J. Ohlmann, J. Benick, G. Siefer, F. Predan, M. Hermle, and F. Dimroth, "Epitaxial GaInP/GaAs/Si Triple-Junction Solar Cell with 25.9% AM1.5g Efficiency Enabled by Transparent Metamorphic AlGaAsP Step-Graded Buffer Structures," *Solar RRL*, 2021.

[7] A. P. Kirk, D. W. Cardwell, J. D. Wood, A. Wibowo, K. Forghani, D. Rowell, N. Pan, and M. Osowski, "Recent Progress in Epitaxial Lift-Off Solar Cells," in *2018 IEEE 7th World Conference on Photovoltaic Energy Conversion (WCPEC) (A Joint Conference of 45th IEEE PVSC, 28th PVSEC & 34th EU PVSEC)*, pp. 0032–0035, IEEE, jun 2018.

[8] R. Lang, J. Schon, F. Dimroth, and D. Lackner, "Optimization of GaAs Solar Cell Performance and Growth Efficiency at MOVPE Growth Rates of 100 μm/h," *IEEE Journal of Photovoltaics*, vol. 8, pp. 1596–1600, nov 2018.

[9] E. N. Parker, "Hydromagnetic Dynamo Models.," *The Astrophysical Journal*, vol. 122, p. 293, sep 1955.

[10] H. Alfvén, "Existence of Electromagnetic-Hydrodynamic Waves," *Nature*, vol. 150, pp. 405–406, oct 1942.

[11] R. Fitzpatrick, *Plasma Physics.* CRC Press, aug 2014.

[12] J. Barth, “Modeling Space Radiation Environments,” *Applying Computer Simulation Tools to Radiation Effects Problems*, p. Section I, 1997.

[13] B. H. Mauk, N. J. Fox, S. G. Kanekal, R. L. Kessel, D. G. Sibeck, and A. Ukhorskiy, “Science objectives and rationale for the radiation belt storm probes mission,” *Space Science Reviews*, vol. 179, no. 1-4, pp. 3–27, 2013.

[14] B. E. Anspaugh, “GaAs Solar Cell Radiation Handbook,” *National Aeronautics and. Space Administration JPL*, pp. 5–5–5–7, 1996.

[15] F. Lei, P. Truscott, C. Dyer, B. Quaghebeur, D. Heynderickx, P. Nieminen, H. Evans, and E. Daly, “MULASSIS: a geant4-based multilayered shielding simulation tool,” *IEEE Transactions on Nuclear Science*, vol. 49, pp. 2788–2793, dec 2002.

[16] S. R. Messenger, E. M. Jackson, J. H. Warner, and R. J. Walters, “SCREAM: A new code for solar cell degradation prediction using the displacement damage dose approach,” *Conference Record of the IEEE Photovoltaic Specialists Conference*, no. June, pp. 1106–1111, 2010.

[17] S. R. Messenger, G. P. Summers, E. A. Burke, R. J. Walters, and M. A. Xapsos, “Modeling solar cell degradation in space: A comparison of the NRL displacement damage dose and the JPL equivalent fluence approaches,” *Progress in Photovoltaics: Research and Applications*, vol. 9, pp. 103–121, mar 2001.

[18] A. Pillukat, K. Karsten, and P. Ehrhart, “Point defects and their reactions in e -irradiated GaAs investigated by x-ray-diffraction methods,” *Physical Review B*, vol. 53, pp. 7823–7835, mar 1996.

[19] N. Chen, S. Gray, E. Hernandez-Rivera, D. Huang, P. D. LeVan, and F. Gao, “Computational simulation of threshold displacement energies of GaAs,” *Journal of Materials Research*, vol. 32, pp. 1555–1562, apr 2017.

[20] J. Lindhard, V. Nielsen, M. Scharff, and P. V. Thomsen, “Integral equations governing radiation effects,” *Mat. Fys. Medd. Dan. Vid. Selsk*, 1963.

[21] G. M. Martin, A. Mitonneau, and A. Mircea, “Electron traps in bulk and epitaxial gaas crystals,” *Electronics Letters*, 1977.

[22] ESA-ESTEC, “ECSS-E-ST-20-08C Rev.1,” *European cooperation for space standardization*, no. July, pp. 1–197, 2012.

[23] J. Bourgoin and M. Lannoo, *Point Defects in Semiconductors II*, vol. 35 of *Springer Series in Solid-State Sciences.* Berlin, Heidelberg: Springer Berlin Heidelberg, 1983.

[24] L. Shao, “An algorithm for fast calculation of ion range and damage distributions based on the boltzmann transport equation,” *Nuclear Instruments and Methods in Physics Research Section B: Beam Interactions with Materials and Atoms*, vol. 268, pp. 3564–3567, dec 2010.

[25] J. F. Ziegler, M. D. Ziegler, and J. P. Biersack, “SRIM - The stopping and range of ions in matter (2010),” *Nuclear Instruments and Methods in Physics Research, Section B: Beam Interactions with Materials and Atoms*, vol. 268, no. 11-12, pp. 1818–1823, 2010.

[26] A. Akkerman, J. Barak, and M. Murat, “A Survey of the Analytical Methods of Proton-NIEL Calculations in Silicon and Germanium,” *IEEE Transactions on Nuclear Science*, vol. 67, pp. 1813–1825, aug 2020.

[27] F. Gao, N. Chen, E. Hernandez-Rivera, D. Huang, and P. D. LeVan, “Displacement damage and predicted non-ionizing energy loss in GaAs,” *Journal of Applied Physics*, vol. 121, p. 095104, mar 2017.

[28] J. Srour, C. Marshall, and P. Marshall, “Review of displacement damage effects in silicon devices,” *IEEE Transactions on Nuclear Science*, vol. 50, pp. 653–670, jun 2003.

[29] G. H. Kinchin and R. S. Pease, “The Displacement of Atoms in Solids by Radiation,” *Reports on Progress in Physics*, vol. 18, p. 301, jan 1955.

[30] M. J. Norgett, M. T. Robinson, and I. M. Torrens, “A proposed method of calculating displacement dose rates,” *Nuclear Engineering and Design*, vol. 33, pp. 50–54, aug 1975.

[31] C. Leroy and P.-G. Rancoita, *Principles of Radiation Interaction in Matter and Detection.* World Scientific Publishing Co. Pte. Ltd., 2011.

[32] Insoo Jun, “Effects of secondary particles on the total dose and the displacement damage in space proton environments,” *IEEE Transactions on Nuclear Science*, vol. 48, no. 1, pp. 162–175, 2001.

[33] A. Akkerman and J. Barak, “New Partition Factor Calculations for Evaluating the Damage of Low Energy Ions in Silicon,” *IEEE Transactions on Nuclear Science*, vol. 53, pp. 3667–3674, dec 2006.

[34] A. R. Sattler, “Ionization Produced by Energetic Silicon Atoms within a Silicon Lattice,” *Physical Review*, vol. 138, pp. A1815–A1821, jun 1965.

[35] N. Mott, “The scattering of fast electrons by atomic nuclei,” *Proceedings of the Royal Society of London. Series A, Containing Papers of a Mathematical and Physical Character*, vol. 124, pp. 425–442, jun 1929.

[36] M. J. Boschini, C. Consolandi, M. Gervasi, S. Giani, D. Grandi, V. Ivanchenko, P. Nieminem, S. Penbotti, P. G. Rancoita, M. Tacconi, S. Pensotti, P. G. Rancoita, and M. Tacconi, “Nuclear and non-ionizing energy-loss of electrons with low and relativistic energies in materials and space environment,” *Astroparticle, Particle, Space Physics and Detectors for Physics Applications - Proceedings of the 13th ICATPP Conference*, pp. 961–982, sep 2012.

[37] M. Boschini, P. Rancoita, and M. Tacconi, "SR-NIEL Calculator: Screened Relativistic (SR) Treatment for Calculating the Displacement Damage and Nuclear Stopping Powers for Electrons, Protons, Light- and Heavy- Ions in Materials," *[Online] available at INFN sez. Milano-Bicocca, Italy [2020,07]: http://www.sr-niel.org/.*, 2020.

[38] S. Messenger, E. Burke, M. Xapsos, G. Summers, and R. Walters, "The Simulation of damage tracks in silicon," *IEEE Transactions on Nuclear Science*, vol. 51, pp. 2846–2850, oct 2004.

[39] S. Messenger, E. Burke, G. Summers, M. Xapsos, R. Walters, E. Jackson, and B. Weaver, "Nonionizing energy loss (NIEL) for heavy ions," *IEEE Transactions on Nuclear Science*, vol. 46, no. 6, pp. 1595–1602, 1999.

[40] C. Baur, M. Gervasi, P. Nieminen, P. G. Rancoita, and M. Tacconi, "Solar Cell Degradation Analysis Applying the Displacement Damage Dose Approach Using Appropriate Niel Values," *European Space Power Conference 2014*, no. April, 2014.

[41] P. A. Schultz and O. A. von Lilienfeld, "Simple intrinsic defects in gallium arsenide," *Modelling and Simulation in Materials Science and Engineering*, vol. 17, p. 084007, dec 2009.

[42] R. W. Jansen and O. F. Sankey, "Theory of relative native- and impurity-defect abundances in compound semiconductors and the factors that influence them," *Physical Review B*, vol. 39, pp. 3192–3206, feb 1989.

[43] W. Shockley and W. T. Read, "Statistics of the Recombination of Holes and Electrons," *Physical Review*, vol. 87, no. 46, pp. 835–842, 1952.

[44] W. Shockley, "The Theory of p-n Junctions in Semiconductors and p-n Junction Transistors," *Bell System Technical Journal*, vol. 28, no. 3, pp. 435–489, 1949.

[45] N. Gruginskie, F. Cappelluti, G. J. Bauhuis, P. Mulder, E. J. Haverkamp, E. Vlieg, and J. J. Schermer, "Electron radiation-induced degradation of GaAs solar cells with different architectures," *Progress in Photovoltaics: Research and Applications*, vol. 28, no. 4, pp. 266–278, 2020.

[46] C.-t. Sah, R. N. Noyce, and W. Shockley, "Carrier Generation and Recombination in P-N junctions," *Proceedings of the IRE*, vol. 1, pp. 1228–1243, 1956.

[47] S. M. Sze and K. K. Ng, "Physics of Semiconductor Devices, 3rd Edition - Simon M. Sze, Kwok K. Ng," *Physics of Semiconductor Devices, 3rd Edition.; John Wiley & Sons, Inc.; NJ*, pp. 164, 682, 2007.

[48] J. C. Bourgoin and M. Zazoui, "Irradiation-induced degradation in solar cell: Characterization of recombination centres," *Semiconductor Science and Technology*, vol. 17, pp. 453–460, may 2002.

[49] H. Y. Tada, J. Carter, J. R., B. E. Anspaugh, R. G. Downing, and D. R. Tada HY, Carter JR, Anspaugh BE, “The Solar Cell Radiation Handbook,” *JPL Publication*, 1982.

[50] N. Gruginskie, F. Cappelluti, M. van Eerden, G. Bauhuis, P. Mulder, E. Vlieg, and J. Schermer, “Proton irradiation induced GaAs solar cell performance degradation simulations using a physics-based model,” *Solar Energy Materials and Solar Cells*, vol. 223, p. 110971, may 2021.

[51] G. Siefer, C. Baur, and A. W. Bett, “External quantum efficiency measurements of Germanium bottom subcells: Measurement artifacts and correction procedures,” in *2010 35th IEEE Photovoltaic Specialists Conference*, pp. 000704–000707, IEEE, jun 2010.

[52] J. Lefèvre, O. Cavani, and B. Boizot, “The sirius facility: A powerful tool for studying irradiation effects in materials,” *13th International Topical Meeting on Nuclear Applications of Accelerators 2017, AccApp 2017: The Expanding Universe of Accelerator Applications*, no. UMR 7642, pp. 117–126, 2018.

[53] S. Park, “Irradiation effects in GaInP/GaAs/Ge triple junction solar cells for deep space applications,” *Ph.D. Dissertation*, 2018.

[54] D. V. Lang, “Deep-level transient spectroscopy: A new method to characterize traps in semiconductors,” *Journal of Applied Physics*, vol. 45, pp. 3023–3032, jul 1974.

[55] T. Walter, R. Herberholz, C. Müller, and H. W. Schock, “Determination of defect distributions from admittance measurements and application to Cu(In,Ga)Se 2 based heterojunctions,” *Journal of Applied Physics*, vol. 80, pp. 4411–4420, oct 1996.

[56] M. Burgelman, P. Nollet, and S. Degrave, “Modelling polycrystalline semiconductor solar cells,” *Thin Solid Films*, vol. 361-362, pp. 527–532, feb 2000.

[57] S. Khelifi, *Characterization and modelling with SCAPS of the performance of solar cells.* PhD thesis, Ghent University, 2010.

[58] K. Decock, S. Khelifi, S. Buecheler, F. Pianezzi, A. N. Tiwari, and M. Burgelman, “Defect distributions in thin film solar cells deduced from admittance measurements under different bias voltages,” *Journal of Applied Physics*, vol. 110, no. 6, 2011.

[59] S. Khelifi, M. Burgelman, J. Verschraegen, and A. Belghachi, “Impurity photovoltaic effect in GaAs solar cell with two deep impurity levels,” *Solar Energy Materials and Solar Cells*, vol. 92, no. 12, pp. 1559–1565, 2008.

[60] P. Blood and J. W. Orton, *The electrical characterization of semiconductors: majority carriers and electron states.* New York: Academic Press, 1992, 1 ed., 1990.

[61] P. Omling, L. Samuelson, and H. G. Grimmeiss, "Deep level transient spectroscopy evaluation of nonexponential transients in semiconductor alloys," *Journal of Applied Physics*, vol. 54, pp. 5117–5122, sep 1983.

[62] A. Das, V. A. Singh, and D. V. Lang, "Deep-level transient spectroscopy (DLTS) analysis of defect levels in semiconductor alloys," *Semiconductor Science and Technology*, vol. 3, pp. 1177–1183, dec 1988.

[63] A. Yelon, B. Movaghar, and R. S. Crandall, "Multi-excitation entropy: Its role in thermodynamics and kinetics," *Reports on Progress in Physics*, 2006.

[64] P. Stallinga and H. L. Gomes, "Trap states as an explanation for the Meyer-Neldel rule in semiconductors," *Organic Electronics*, vol. 6, no. 3, pp. 137–141, 2005.

[65] S. W. Johnston, R. S. Crandall, and A. Yelon, "Evidence of the Meyer-Neldel rule in InGaAsN alloys and the problem of determining trap capture cross sections," *Applied Physics Letters*, vol. 83, pp. 908–910, aug 2003.

[66] O. Engstrom, "Compensation effects at electron traps in semiconductors," *Monatshefte fur Chemie*, vol. 144, no. 1, pp. 73–82, 2013.

[67] F. R. Shapiro and J. R. Tuttle, "The Meyer-Neldel rule in emission rates from defects in copper indium diselenide," *Solid State Communications*, vol. 87, pp. 199–202, jul 1993.

[68] R. J. Walters, M. A. Xapsos, H. L. Cotal, S. R. Messenger, G. P. Summers, P. R. Sharps, and M. L. Timmons, "Radiation response and injection annealing of P+N InGaP solar cells," *Solid-State Electronics*, vol. 42, no. 9, pp. 1747–1756, 1998.

[69] M. Yamaguchi, "Radiation resistance of compound semiconductor solar cells," *Journal of Applied Physics*, vol. 78, pp. 1476–1480, aug 1995.

[70] M. Salzberger, M. Rutzinger, C. Nömayr, P. Lugli, and C. G. Zimmermann, "Voltage-dependent photocurrent in irradiated GaAs solar cells," *Progress in Photovoltaics: Research and Applications*, pp. 1–9, 2018.

[71] C. Pellegrino, A. Gagliardi, and C. G. Zimmermann, "Difference in space-charge recombination of proton and electron irradiated GaAs solar cells," *Progress in Photovoltaics: Research and Applications*, vol. 27, pp. 379–390, may 2019.

[72] C. Pellegrino, A. Gagliardi, and C. G. Zimmermann, "Impact of Proton and Electron Irradiation-Induced Defects on the Dark Current of GaAs Solar Cells," *IEEE Journal of Photovoltaics*, vol. 9, pp. 1661–1667, nov 2019.

[73] F. Stöckmann, "On the classification of traps and recombination centres," *Physica Status Solidi (a)*, vol. 20, no. 1, pp. 217–220, 1973.

[74] R. Corkish and M. A. Green, "Junction recombination current in abrupt junction diodes under forward bias," *Journal of Applied Physics*, vol. 80, pp. 3083–3090, sep 1996.

[75] J. Pallarès, L. F. Marsal, X. Correig, J. Calderer, and R. Alcubilla, "Space charge recombination in P-N junctions with a discrete and continuous trap distribution," *Solid-State Electronics*, vol. 41, no. 1, pp. 17–23, 1997.

[76] G. A. Hurkx, D. B. Klaassen, and M. P. Knuvers, "A New Recombination Model for Device Simulation Including Tunneling," *IEEE Transactions on Electron Devices*, vol. 39, no. 2, pp. 331–338, 1992.

[77] M. Auf der Maur, M. Povolotskyi, F. Sacconi, and A. Di Carlo, "TiberCAD: A new multiscale simulator for electronic and optoelectronic devices," *Superlattices and Microstructures*, 2007.

[78] J. C. Bourgoin and N. De Angelis, "Radiation-induced defects in solar cell materials," *Solar Energy Materials and Solar Cells*, vol. 66, no. 1-4, pp. 467–477, 2001.

[79] D. Stievenard, X. Boddaert, and J. C. Bourgoin, "Irradiation-induced defects in p -type GaAs," *Physical Review B*, vol. 34, pp. 4048–4058, sep 1986.

[80] R. Campesato, C. Baur, M. Casale, M. Gervasi, E. Gombia, E. Greco, A. Kingma, P. G. Rancoita, D. Rozza, and M. Tacconi, "NIEL DOSE and DLTS Analyses on Triple and Single Junction solar cells irradiated with electrons and protons," in *2018 IEEE 7th World Conference on Photovoltaic Energy Conversion (WCPEC) (A Joint Conference of 45th IEEE PVSC, 28th PVSEC & 34th EU PVSEC)*, no. January 2019, pp. 3768–3772, IEEE, jun 2018.

[81] T. P. Weiss, A. Redinger, D. Regesch, M. Mousel, and S. Siebentritt, "Direct Evaluation of Defect Distributions From Admittance Spectroscopy," *IEEE Journal of Photovoltaics*, vol. 4, pp. 1665–1670, nov 2014.

[82] D. Walker, Yao Yue, C. J. Mann, J. Nocerino, and S. H. Liu, "Dark current characterization of irradiated solar cells," in *2015 IEEE 42nd Photovoltaic Specialist Conference (PVSC)*, vol. 10, pp. 1–3, IEEE, jun 2015.

[83] C. Pellegrino, A. Gagliardi, and C. G. Zimmermann, "Defect spectroscopy and non-ionizing energy loss analysis of proton and electron irradiated p-type GaAs solar cells," *Journal of Applied Physics*, vol. 128, p. 195701, nov 2020.

[84] M. Levinshtein, S. Rumyantsev, and M. Shur, *Handbook Series on Semiconductor Parameters*, vol. 2. WORLD SCIENTIFIC, nov 1996.

[85] R. Hoheisel and A. W. Bett, "Experimental Analysis of Majority Carrier Transport Processes at Heterointerfaces in Photovoltaic Devices," *IEEE Journal of Photovoltaics*, vol. 2, pp. 398–402, jul 2012.

[86] W. Hu, J. Xie, H. W. Chau, and B. C. Si, "Evaluation of parameter uncertainties in nonlinear regression using Microsoft Excel Spreadsheet," *Environmental Systems Research*, vol. 4, p. 4, jan 2015.

[87] T. Mattila and R. M. Nieminen, "Direct Antisite Formation in Electron Irradiation of GaAs," *Physical Review Letters*, vol. 74, pp. 2721–2724, apr 1995.

[88] J. C. Bourgoin, H. J. von Bardeleben, and D. Stiévenard, "Native defects in gallium arsenide," *Journal of Applied Physics*, vol. 64, pp. R65–R92, nov 1988.

[89] D. Pons and J. C. Bourgoin, "Irradiation-induced defects in GaAs," *Journal of Physics C: Solid State Physics*, vol. 18, pp. 3839–3871, jul 1985.

[90] A. F. Wright and N. A. Modine, "Migration processes of the As interstitial in GaAs," *Journal of Applied Physics*, vol. 120, p. 215705, dec 2016.

[91] P. Blood and J. J. Harris, "Deep states in GaAs grown by molecular beam epitaxy," *Journal of Applied Physics*, vol. 56, no. 4, pp. 993–1007, 1984.

[92] R. M. Fleming, C. H. Seager, E. Bielejec, G. Vizkelethy, D. V. Lang, and J. M. Campbell, "Defect annealing in neutron and ion damaged silicon: Influence of defect clusters and doping," *Journal of Applied Physics*, vol. 107, p. 053712, mar 2010.

[93] R. M. Fleming, D. V. Lang, C. H. Seager, E. Bielejec, G. A. Patrizi, and J. M. Campbell, "Continuous distribution of defect states and band gap narrowing in neutron irradiated GaAs," *Journal of Applied Physics*, vol. 107, p. 123710, jun 2010.

[94] J. H. Warner, S. R. Messenger, R. J. Walters, S. A. Ringel, and M. R. Brenner, "A deep level transient spectroscopy study of electron and proton irradiated p+n GaAs diodes," in *2009 European Conference on Radiation and Its Effects on Components and Systems*, vol. 57, pp. 282–285, IEEE, sep 2009.

[95] R. M. Fleming, S. M. Myers, W. R. Wampler, D. V. Lang, C. H. Seager, and J. M. Campbell, "Field dependent emission rates in radiation damaged GaAs," *Journal of Applied Physics*, vol. 116, p. 013710, jul 2014.

[96] M. A. Zaidi, H. Maaref, and J. C. Bourgoin, "Minority carrier capture cross section of the EL2 defect in GaAs," *Applied Physics Letters*, vol. 61, no. 20, pp. 2452–2454, 1992.

[97] N. A. Naz, U. S. Qurashi, and M. Z. Iqbal, "Arsenic antisite defects in p-GaAs grown by metal-organic chemical-vapor deposition and the EL2 defect," *Journal of Applied Physics*, vol. 106, p. 103704, nov 2009.

[98] A. Mąkosa, T. Wosiński, and W. Szkiełko, "Electric Field Enhanced Emission of Holes from the Double Donor Level of the EL2 Defect in GaAs," *Acta Physica Polonica A*, vol. 82, no. 5, pp. 813–816, 1992.

[99] J. H. Warner, *Displacement damage-induced electrical and structural effects in gallium arsenide solar cells following ion irradiation.* PhD thesis, University of Maryland, Baltimore County, 2008.

[100] S. M. Myers, P. J. Cooper, and W. R. Wampler, "Model of defect reactions and the influence of clustering in pulse-neutron-irradiated Si," *Journal of Applied Physics*, vol. 104, p. 044507, aug 2008.

[101] E. Bielejec, G. Vizkelethy, R. M. Fleming, D. K. Serkland, J. K. McDonald, G. A. Patrizi, and D. B. King, "Experimental Study of Defect Formations in GaAs Devices Using Gain, Photoluminescence and Deep Level Transient Spectroscopy," *IEEE Transactions on Nuclear Science*, vol. 60, pp. 219–223, feb 2013.

[102] K. Nordlund, J. Peltola, J. Nord, J. Keinonen, and R. S. Averback, "Defect clustering during ion irradiation of GaAs: Insight from molecular dynamics simulations," *Journal of Applied Physics*, vol. 90, no. 4, pp. 1710–1717, 2001.

[103] J. R. Srour and J. W. Palko, "Displacement Damage Effects in Irradiated Semiconductor Devices," *IEEE Transactions on Nuclear Science*, vol. 60, pp. 1740–1766, jun 2013.

[104] R. Hoheisel, A. Bett, J. Warner, R. Walters, and P. Jenkins, "Low Temperature Low Intensity Effects in III-V Photovoltaic Devices for Deep Space Missions," in *2018 IEEE 7th World Conference on Photovoltaic Energy Conversion (WCPEC) (A Joint Conference of 45th IEEE PVSC, 28th PVSEC & 34th EU PVSEC)*, pp. 3763–3767, IEEE, jun 2018.